DEVELOPMENT AND TESTING OF A 3 DOF TANDEM FLAPPING WING MECHANISM

A THESIS SUBMITTED TO
THE GRADUATE SCHOOL OF NATURAL AND APPLIED SCIENCES
OF
MIDDLE EAST TECHNICAL UNIVERSITY

BY

TALHA MUTLU

IN PARTIAL FULFILLMENT OF THE REQUIREMENTS
FOR
THE DEGREE OF MASTER OF SCIENCE
IN
AEROSPACE ENGINEERING

FEBRUARY 2014

Approval of the thesis:

DEVELOPMENT AND TESTING OF A 3 DOF TANDEM FLAPPING WING MECHANISM

Submitted by **TALHA MUTLU** in partial fulfillment of the requirements for the degree of **Master of Science in Aerospace Engineering Department, Middle East Technical University** by,

Prof. Dr. Canan ÖZGEN _____
Dean, Graduate School of **Natural and Applied Sciences**

Prof. Dr. Ozan TEKİNALP _____
Head of Department, **Aerospace Engineering**

Assoc. Prof. Dr. Dilek Funda KURTULUŞ _____
Supervisor, **Aerospace Engineering Dept., METU**

Examining Committee Members:

Prof. Dr. Ozan TEKİNALP _____
Aerospace Engineering Dept., METU

Assoc. Prof. Dr. Dilek Funda KURTULUŞ _____
Aerospace Engineering Dept., METU

Assoc. Prof. Dr. Oğuz UZOL _____
Aerospace Engineering Dept., METU

Asst. Prof. Dr. Ali Türker KUTAY _____
Aerospace Engineering Dept., METU

Asst. Prof. Dr. Mustafa KAYA _____
Dept. of Aeronautical Science, UTAA

Date: 05.02.2014

I hereby declare that all information in this document has been obtained and presented in accordance with academic rules and ethical conduct. I also declare that, as required by these rules and conduct, I have fully cited and referenced all material and results that are not original to this work.

Name, Last Name : Talha MUTLU

Signature :

ABSTRACT

DEVELOPMENT AND TESTING OF A 3 DOF TANDEM FLAPPING WING MECHANISM

Mutlu, Talha

M.Sc., Department of Aerospace Engineering

Supervisor: Assoc. Prof. Dr. Dilek Funda Kurtuluş

February 2014, 131 pages

Scope of the thesis is to develop a tandem flapping wing mechanism, capable of mimicking the insect flight, in order to investigate the 3-D complex nature of the flow around the flapping wings. Thus, valuable data about the unsteady aerodynamics of such flow can be obtained in order to provide necessary knowledge for development of future Micro Air Vehicles (MAVs). The mechanism is equipped with a state of art multi axial force and torque sensor. By placing the sensor to the root chord of the wing, any force and moment that are exerted to wing can be measured in real-time. In order to design the mechanism, wing trajectories of various insect and birds are investigated. Moreover; different flapping MAVs and flapping wing test setups are examined to provide a better understanding of existing flapping wing technology. By doing so, requirements for a new mechanism are decided. The mechanism has a robotic wrist, enabling the rotation in three axis, which are driven by three motor for each wing. A custom made micro controller with embedded software 'Wing-Sim' governs the motor drivers, sensors and data transfer between the main computer and wings. Furthermore; different wing trajectories can be performed and logged by Wing-Sim. During the

experiments a bio-inspired wing measuring 24 cm span and 8 cm chord, with 3 mm thickness flat plate airfoils are used. Calibration and validation test of the system are completed and presented in the results.

Keywords: Flapping Wing Mechanism, Unsteady Aerodynamics, Force Measurement, Micro Air Vehicles

ÖZ

ÜÇ EKSENDE SERBESTLİK DERECESİNE SAHİP İKİLİ KANAT ÇIRPMA MEKANİZMASI GELİŞTİRİLMESİ VE TEST EDİLMESİ

Mutlu, Talha

Yüksek Lisans, Havacılık ve Uzay Mühendisliği Bölümü

Tez Yöneticisi: Doç. Dr. Dilek Funda Kurtuluş

Şubat 2014, 131 sayfa

Bu tezin amacı; çırpan kanatlar etrafındaki karmaşık 3-B akışları incelemek amacı ile böcek uçuşunu taklit etme yeteneği olan çift kanatlı bir çırpan kanat test düzeneği geliştirmektir. Böylece, bu tip kararsız akışların incelenmesinden elde edilen değerli veriler gelecekte mikro hava araçlarının tasarımı için gereken bilgiyi sağlayacaktır. Mekanizma son teknoloji ürünü çok eksenli kuvvet ve dönme momenti algılayıcısı ile donatılmıştır. Kanat üzerine yerleştirilen bu algılayıcılar sayesinde kanada uygulanan kuvvet ve momentler eş zamanlı olarak ölçülebilmektedir. Mekanizmayı tasarlarken farklı kuş ve böcek türlerinin kanat çırpma şekilleri incelenmiştir. Ayrıca, çırpan kanat teknolojisi hakkında daha iyi bir fikir sahibi olma amacı ile kanat çırpan mikro hava araçları ve çırpan kanat test düzenekleri incelenmiştir. Böylece, tasarlanacak yeni sistemin gereksinimleri belirlenmiştir. Mekanizma 3 farklı motor ile sürülen mekanik bir dirsek aracılığı ile 3 eksende dönme hareketini sağlar. Motor sürücüler, algılayıcılar ve ana bilgisayar ile kanatlar arasındaki veri alışverişi özgün yazılıma ‘Wing-Sim’ sahip mikro kontrolcü ile sağlanmaktadır. Wing-Sim aracılığı ile farklı kanat çırpma şekilleri gerçekleştirilir ve eş zamanlı olarak kaydedilir. Deneyler sırasında 3mm kalınlığında levha kanat kesitli 24 cm kanat uzunluğu 8 cm veter

uzunluğu ölçülerinde kanat kullanılmıştır. Mekanizmanın ince ayar ve ölçüm doğrulama verileri sonuç kısmında sunulmuştur.

Anahtar Kelimeler: Çırpan Kanat Mekanizması, Zamana Bağlı Aerodinamik, Kuvvet Ölçümü, Mikro Hava Aracı

to my parents...

ACKNOWLEDGMENTS

I would like to express my deepest gratitude to my supervisor Assoc. Prof. Dr. Dilek Funda Kurtuluş for all the opportunities she provided to me during all stages of this study. I am grateful to her for her sincere and valuable guidance.

I also thank my jury members Prof. Dr. Ozan Tekinalp, Assoc. Prof. Dr. Oğuz Uzol, Asst. Prof. Dr. Ali Türker Kutay, and Asst. Prof. Dr. Mustafa Kaya for reviewing my thesis.

I am indebted to the technical assistance of Emre Akgül, Serkan Tarçın and Alper Güngör during the development and manufacturing process of the flapping wing mechanism. Also, Cavid Xelilov for helping me to prepare the measurement instruments.

I would like to specially thank to METU Center for Wind Energy - MetuWind for providing special multi axial load cell.

This work is a part of the project supported by TÜBA GEBİP Award given to Dr. Kurtuluş.

I would like the thank Sinem Cihan most sincerely for her support and encouragement.

Above all, I owe my sincere and earnest thankfulness to my family for their unceasing encouragement and support. If they did not support me in all stages of my life, I would not be here. Thank God that I have them.

TABLE OF CONTENTS

APPENDICES

LIST OF TABLES

TABLES

LIST OF FIGURES

FIGURES

NOMENCLATURE

Latin Symbol	Description	Units
A	Motion function amplitude	deg
AR	Aspect ratio	-
c	Chord length	m
C	Conversion matrix	-
D	Motion function offset	deg
f	Frequency of the motion	Hz
F_D	Drag Force	N
F_L	Lift Force	N
F_T	Total ‘thrust’ force	N
h	Wing-beat amplitude	rad
L_{ref}	Reference length	m
K_p	P-Constant	-
k	Reduced frequency	-
R	Wing span	m
Re	Reynolds number	-
St	Strouhal number	-
t	Time variable	s
T	Period of the motion	s
t/T	Non-dimensional time variable	-
U_{ref}	Reference velocity	m/s
x	Pitch axis	-
y	Heave axis	-
z	Plunge axis	-

Greek Symbol	Description	Units
σ	Standard deviation (in force, velocity)	N, m/s
α	Pitch angle	deg
β	Heave angle	deg
δ	Total force angle	deg
θ	Plunge angle	deg
$\dot{\alpha}$	Pitch rate	deg/s
$\dot{\beta}$	Heaving rate	deg/s
$\dot{\theta}$	Plunge rate	deg/s
ε	Position error	deg
φ	Motion function phase angle	rad
ζ	User defined motion function	-
ψ	PWM signal	-
μ	Dynamic viscosity of the fluid	kg/m·s
υ	Kinematic viscosity of the fluid	m^2/s
ω	Angular velocity	rad/s

Subscript	Description
m	Motor parameter
w	Wing parameter

Abbreviations

2-D	Two-Dimensional
3-D	Three-Dimensional
FFT	Fast Fourier Transformation
LEV	Leading Edge Vortex
MAV	Micro Air Vehicle
PIV	Particle Image Velocimetry
PIC	Peripheral Interface Controller
PWM	Pulse Width Modulation
TEV	Trailing Edge Vortex

This page intentionally left blank

CHAPTER 1

INTRODUCTION

1.1 Background Information

Insect flight fascinates the scientists and engineers for centuries with its better aerodynamic performance and increased maneuverability for low flight velocities. Flapping wing is a favorable design for low Reynolds number regime. Figure 1.1 illustrates the trend line for changing flight velocity and weight ([1]- [2]). Also, lift generating mechanism changes from fixed wing to flapping wing with decreasing flight velocity (or Reynolds number).

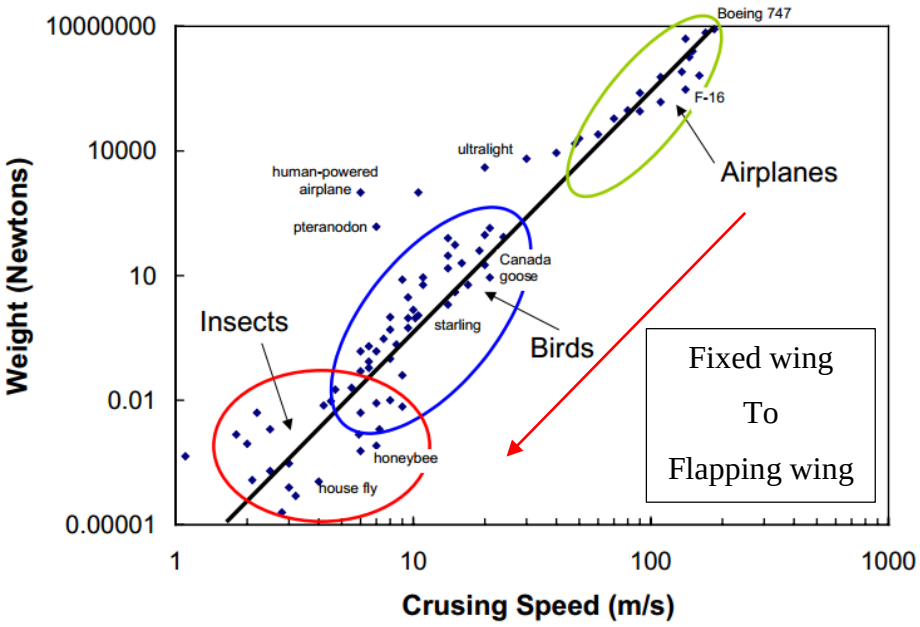

Figure 1.1 Great diagram of flight (from Ref. [1])

Flapping wing is an advanced design, being evolved by natural selection [3]. It shows superior flight characteristics comparing to most of the advanced aircrafts. For instance, SR-71A Blackbird, which is an advanced, long-range, Mach 3+ strategic reconnaissance aircraft, sets the speed and altitude record (Altitude in horizontal flight: 85,069 ft (25,929 m) and speed over a straight course: 2,193 miles per hour (3,529 km/h)) in July 1976 [4]. Even the Blackbird can cover roughly 30 body length per second whereas a European starling can cover 120 body length per second [5]. Furthermore, a Barn Swallow has a roll rate of $5000°/s$ whereas an aerobatic aircraft typically performs $720°/s$ [6]. At last, typical manned aircrafts fly at Reynolds number of 10^6-10^8. On the other hand, most of the insects fly at Reynolds number of 10^3-10^4 (Figure 1.2). Thus, air must be 10^4 times more viscous for a conventional aircraft to fly at the same Reynolds number with the insects and still generate enough lift in order to stay up.

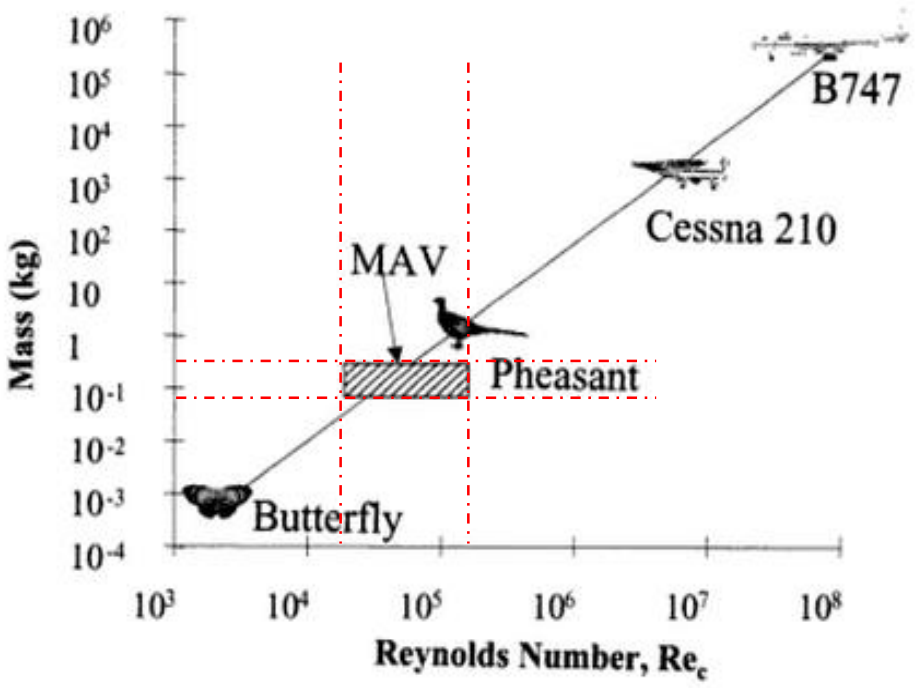

Figure 1.2 Flight regime compared to existing vehicles in Reynolds number scale (from Ref. [7])

Owing to the advances in the micro-technologies and material science, which enable the development of Micro Air Vehicles (MAVs), study of low Reynolds number flight regime becomes very important. According to the definition, given by the Defense Advanced Research Projects Agency (DARPA) in 1997 [8], an aircraft with maximum dimensions of 15 cm and maximum weight of 90 grams is called MAV. MAVs can operate at Reynolds numbers that both birds and insects fly. Birds and insects fly at quite different Reynolds numbers, thus they need different lift generation mechanisms during the flight. There are three different generation of MAVs: fixed wing, rotary wing and flapping wing. Fixed wing aircrafts cannot hover, which makes them less favorable for use in a confined space. On the other hand the rotary wing MAVs encounter stability problems in vicinity of solid wall boundaries. The flapping wing concept happens to be the best approach for MAVs.

1.2 Present Approach

Insects can clap their wings in horizontal direction with great changes in pitch angle. Thus, they can hover by using extra lift generating effect of highly vortical fields that are generated at leading edge and trailing edge of the wings [9]. On the other hand, birds need to have free stream velocity to generate lift by clapping their wings in vertical direction. Thus they cannot hover. In order to design bird like or insect like MAVs, one must understand different lift and thrust generating mechanisms of horizontal, vertical and combined flapping motion.

The current study aims to develop a novel experimental setup in order to investigate insect and bird like flight conditions. Wing trajectories with sinusoidal pure pitch, pure plunge and combined pitch and plunge motions are considered. A novel wing mechanism (Robot-Wing) is developed in order to mimic the bird and insect flight conditions [10]. During the experiments, force and moment quantities are measured at all principle axes of the wing by using a special sensor which is attached to the wing.

1.3 Major Objectives

The major objectives of the present study are:

- To develop a tandem flapping wing mechanism that can be used with water tank/tunnel and wind tunnel. The mechanism should have the capability of measuring aerodynamic forces by using force/torque sensor which is attached to the wing, also it should be suitable for Particle Image Velocimetry (PIV). Moreover, the mechanism should be capable of investigating the nature of bird and insect like flight;

- To find the characteristics of the wing mechanism and generate proportional control calibration data w.r.t. medium and wing weight for the motors.

- To build an experimental setup in order to investigate the effect of flapping trajectory, frequency, and the wing geometry for different test cases such as single wing or tandem wing;

- To establish an experiment methodology for the new setup in order to obtain reliable data;

- To investigate motion trajectories with sinusoidal combined pitch and plunge motions of a bio-inspired 3 mm thick flat plate wing in order to provide a better understanding of flapping aerodynamics by means of experimental studies.

1.4 Outline of the Thesis

Present study consists of six chapters in order to fulfill the objectives that are stated above. In Chapter I, background informations about flapping flight, MAVs and major objectives of the study are given. Chapter II explains the unsteady lift generating mechanisms of the flapping wings, then briefly mentions the important non-dimensional parameters and the dynamic scaling. Moreover, 4 flapping wing MAVs

from literature are presented with their important characteristics. Finally, 5 different flapping mechanisms are compared and important parameters are tabulated. Especially, wing mechanism with adjustable motion trajectory and force measurement capabilities are considered in this chapter. In Chapter III, the design process of the robotic wing mechanism (Robot-Wings) is explained. Chapter IV explains the experimental setup, force measurement, data acquisition, and experimental procedure. In Chapter V, calibration data for the Robot-Wings is given. Also, force and moment results for different wing trajectories are presented. Chapter VI presents the general conclusions and future recommendations for the study.

CHAPTER 2

LITERATURE SURVEY

This chapter is focused on the former studies about flapping wings by means of experimental approaches. The chapter is divided into six sections. In the first part, studies, regarding to understand aerodynamics mechanisms, which are behind the superior characteristics of flapping wigs, are considered. In the second part, some important non-dimensional parameters of flapping wing aerodynamics are presented. In the third part, dynamic scaling is discussed. Fourth part focuses on the flapping trajectories of the certain animal. The fifth part considers four autonomously flying flapping vehicles. Finally, in the last part, adjustable wing trajectory flapping wing mechanisms are presented.

2.1 Lift Generating Unsteady Mechanisms

Recent advances in the microelectronics technology enables the production of smaller UAV systems that are called Micro Air Vehicle (MAV). However, they need different lift generating mechanisms rather than fixed wing and rotary wing. MAVs that are using flapping flight technologies exhibit superior characteristics compared to fixed wing and rotary wing due to better aerodynamic performance and maneuverability at low flight velocities. Wagner effect is the impulsive starting effect on lift generation. In addition, there are four main unsteady mechanisms for extra lift generation during flapping ([11]- [12]). First and the most important one is the dynamic stall or leading edge vortex (LEV) because it generates lift during the transitional phase of the stroke

([13]- [14]). Other three mechanisms, namely clap-and-fling mechanism ([15]- [16]), wake capturing phenomenon ([17]- [18]) and rotational lift (Kramer effect) ([14]- [19]- [20]), are effective during the rotational phases.

Flapping wing lift and drag calculations also differ. For fixed wing aircrafts, lift and drag coefficients (C_L and C_D) are functions of wing profile. Flapping wings behave like fixed wing for steady state flow regime. However, for unsteady flows, they cannot be considered separately [21]. LEV formation requires wing to be exposed to high angles of attack. This condition causes a normal force formation on the wing. Therefore, Dickinson defined a circulatory coefficient that consist of lift and drag [22]. This total force and its direction has to be determined experimentally (Eq. 2.1-2).

$$F_T = \sqrt{{F_L}^2 + {F_D}^2} \tag{2.1}$$

$$\delta_T = tan^{-1}(\frac{L}{D}) \tag{2.2}$$

2.1.1 Wagner Effect

The circulation slowly approach its steady-state value instead of converging immediately as a result of impulsive start of flapping motion. This delay results of viscous behavior of the fluid and vortex shedding at trailing edge [12]. Due to viscosity effect, it takes time to establish Kutta condition. Also vortex shedding phenomenon at trailing edge starts a new vortex. When the starting vortex moves away from the trailing edge, maximum circulation on the wing is observed. This slow development of circulation, which is first proposed by Wagner in 1925, is called as *Wagner effect*.

2.1.2 Leading Edge Vortex

After exceeding a certain angle of attack, it is followed by flow separation and stall for steady flow regime. However; in unsteady flow regime, an attached vortex is created

at leading edge of the wing for a great part of the stroke. This vortex is one of the most important mechanisms of the flapping wings and called as Leading Edge Vortex (LEV). LEVs induce a downward velocity and so increase the lift force. Flow direction changes rapidly at leading edge that generates a leading edge suction vector for blunt wing profiles. On the other hand, Figure 2.1 shows that a leading edge vortex is generated for the flow around thin airfoils so the suction vector becomes normal to the wing, which is added up to lift.

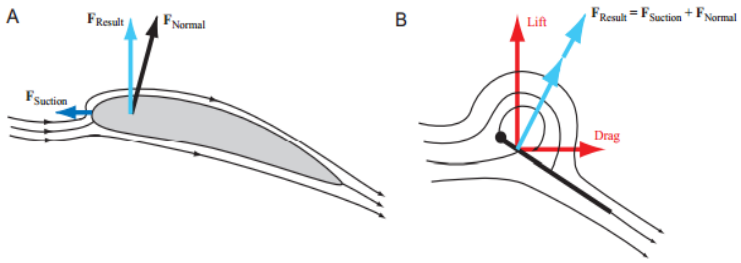

Figure 2.1 Leading edge vortex lift contribution (adopted from Ref. [12])

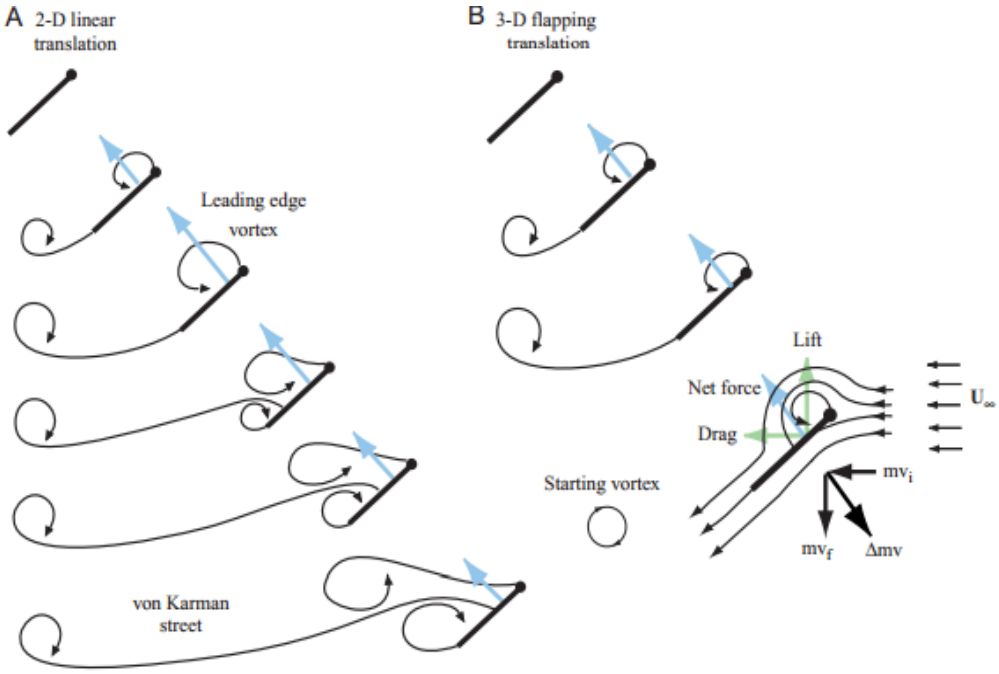

Figure 2.2 Leading edge vortex development in (a) 2-D and (b) 3-D during linear transition starting form rest (from Ref. [12])

If the leading edge vortex has high vorticity values, the flow cannot be reattached before the trailing edge and a trailing edge vortex is formed. This condition is called

dynamic or delayed stall and cause a dramatic drop of lift. According to Figure 2.2 the leading edge vortex is more stable for 3-D case and no trailing edge vortex forms whereas it is not the same for 2-D case. Stability of the leading edge vortex, which is only presented for the 3-D case, is considered in different studies ([23]- [24]).

2.1.3 Clap and Fling

Clap and fling mechanism is explained by Weis-Fogh (1973) [15] and Lighthill (1973) [25] as follows; at the end of each upstroke wings come together. This movement is called 'clap'. After the clap, wings start to separate providing that the trailing edges stay unseparated. This movement is called as 'fling'. Air is sucked between the wings during the down stroke. As a result, a bound vortex, which acts like a starting vortex for the other wing, is formed at each wings leading edge. Due to *Wagner effect* circulations build up more rapidly. Moreover; vortices that are created during upstroke phase vanish when the wings clap to each other due to opposite orientation. Figure 2.3 gives an extensive illustration of clap and fling mechanism.

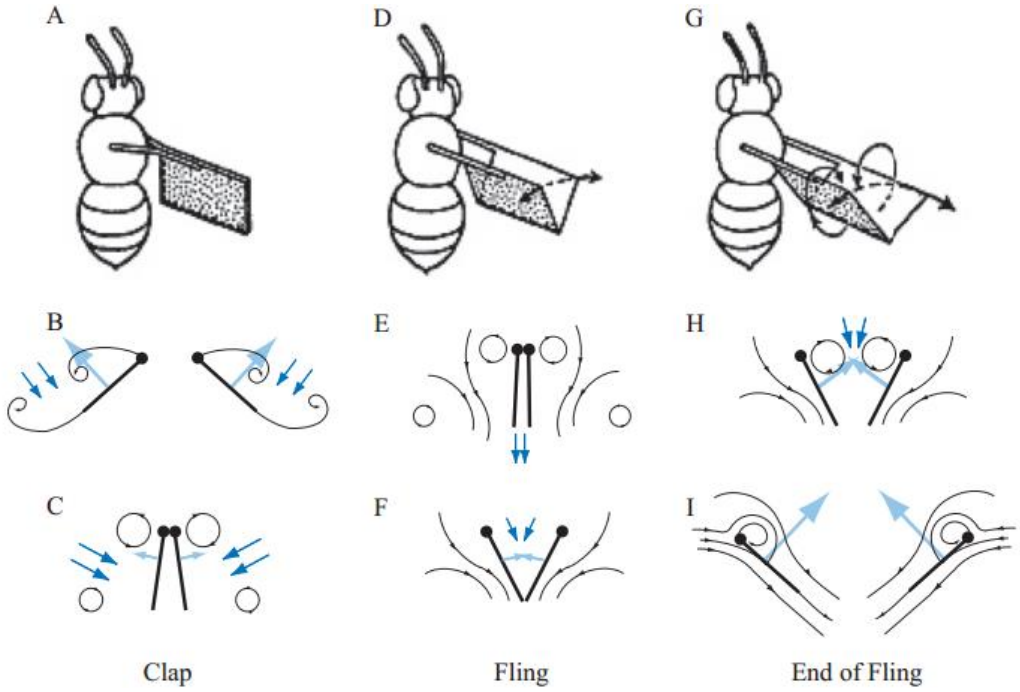

Figure 2.3 Schematic representation of the clap (A-C) and fling (D-F) mechanism (from Ref. [26])

2.1.4 Rotational Lift

Rotational lift, which is also called as *Kramer effect*, is first proven via experimental methods by Kramer (1932) [19]. Insects and some small birds (e.g. hummingbirds) are rotating their wings near the end of each stroke. By doing so, positive angle of attack and lift generation during both forward and reverse strokes is maintained. Dickinson states that lift force generation strongly depends on the rotation axis chord wise location [17]. Moreover; rotation around trailing edge shows better lift characteristics then rotation around leading edge. Also, timing is an important parameter for lift generation.

2.1.5 Wake Capturing

The reciprocating motion of the wings causes wing interaction with shed vorticity of prior strokes, which end up with increased lift generation. This interaction is observed for 2-D motion of flat plate by Dickinson [17]. A similar phenomenon is also observed with 3-D mechanical model of a fruit fly and measured by force transducer and PIV [27].

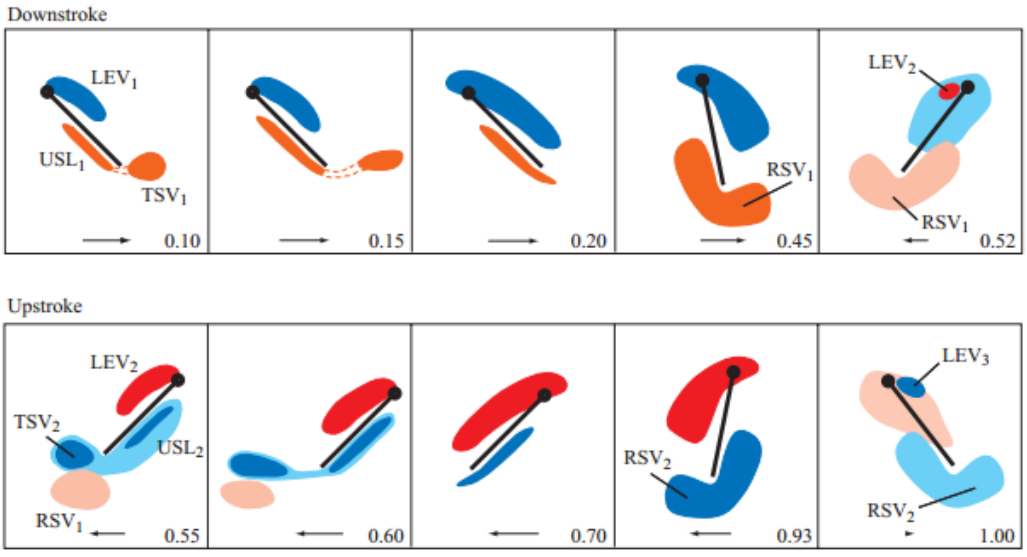

Figure 2.4 Wing-wake interaction at the end stroke (from Ref. [18]) (RSV: rotational Starting vortex, TSV: trailing-edge starting vortex, USL underwing shear layer)

Figure 2.4 shows the wing-wake capture phenomenon step by step. Warm tones (reds) represent CCW vorticity and cool tones (blues) represent CW vorticity. At the end of the downstroke, the wing starts to rotate causing the vortices at the edges to shed of the wing. Strong velocity field is induced and pushed against the wing. Hence, lift is increased at the beginning of the upstroke. A new LEV is formed with the following stroke.

2.2 Significant Non-dimensional Parameters

Three fundamental non-dimensional parameters, that have significant role regarding the flow dynamics, are Reynolds number (*Re*), Strouhal number (*St*) and reduced frequency (*k*) [28]. Reynolds number represents the ratio of the inertial forces to viscous forces for a fluid. Strouhal number is used for characterizing the vortex dynamics and shedding behavior of unsteady flow. Finally, reduced frequency, which is a measure of flow unsteadiness imposed by flapping motion, is the ratio of the flapping velocity to the free stream velocity. Reynolds number can be defined as follows for a given reference length and reference velocity.

$$Re = \frac{\rho U_{ref} L_{ref}}{\mu} = \frac{U_{ref} L_{ref}}{\nu} \tag{2.2}$$

Rho 'ρ' is the fluid density, mu 'μ' is the dynamic viscosity and nu 'ν' is the kinematic viscosity of the fluid. For flapping flight, the mean chord length of wing is used as reference length. However, reference velocity is defined differently for hovering and forward flight. Mean velocity of the wing tip can be used as reference velocity for 3-D hovering case whereas the maximum flapping is used for 2-D hovering flights. It can be written as $U_{ref} = \omega R$, where R is the wing length and omega is the mean angular velocity of the wing ($\omega = 2hf$, where h is the wing-beat amplitude in radians and f is the flapping frequency). Hence, Reynolds number for a 2-D flapping airfoil undergoing hovering motion can be written as follows;

$$Re = \frac{U_{ref}L_{ref}}{\nu} = \frac{U_{ref}c}{\nu} = \frac{2\pi fhc}{\nu} \tag{2.3}$$

Reynolds number for 3-D flapping wing undergoing hovering motion is given by;

$$Re = \frac{U_{ref}L_{ref}}{\nu} = \frac{2hfRc}{\nu} = \frac{hfR^2}{\nu}\left(\frac{4}{AR}\right) \tag{2.4}$$

Note that, for a 3-D flow Reynolds number is proportional with the wing-beat amplitude, flapping frequency and the square of the wing span, but inversely proportional with the wing's aspect ratio. In forward flight, flight velocity is used as the reference velocity. The second significant non-dimensional parameter in flows showing an unsteady aerodynamic behavior is the Strouhal number for flapping flight and is defined as follows;

$$St = \frac{fL_{ref}}{U_{ref}} = \frac{2fh}{U_{ref}} \tag{2.5}$$

Second definition (right) of Strouhal number describes a ratio between the flapping speed (*fh*) and the forward speed (U), which offers a propulsion efficiency criterion for flapping wings. The last non-dimensional parameter that characterizes the unsteady aerodynamics of the flapping airfoils is the reduced frequency. It is defined as follows;

$$k = \frac{\omega fc}{2U_{ref}} = \frac{\pi fc}{U_{ref}} \tag{2.6}$$

For 2-D hovering airfoils the reduced frequency can be written as follows;

$$k = \frac{\pi fc}{U_{ref}} = \frac{c}{2h} \tag{2.7}$$

In hovering 3-D flight reduced the frequency can be defined as follows;

$$k = \frac{\pi fc}{U_{ref}} = \frac{\pi c}{2hR} = \frac{\pi}{gAR} \tag{2.8}$$

2.3 Dynamic Scaling

Experimental studies usually require a scaling by means of Reynolds number and Strouhal number ([29], [30]). Thus, flapping frequency and fluid flow velocity can be determined. For instance, consider a case-zero with a characteristic length of L_0, reference velocity of U_0, and the kinematic viscosity of ν_0 and an experiment case with a scaled characteristic length of L_s, reference velocity of U_s, and kinematic viscosity of ν_s with respect to case-zero. Reynolds numbers for both cases are defined as follows

$$Re_0 = \frac{U_0 L_0}{\nu_0} \;\; \& \;\; Re_s = \frac{U_s L_s}{\nu_s} \tag{2.9}$$

The Strouhal number for case-zero and scaled experiment case is given below;

$$St_0 = \frac{f_0 L_0}{U_0} \;\; \& \;\; St_s = \frac{f_s L_s}{U_s} \tag{2.10}$$

Equating the Reynolds number and Strouhal number of case-zero and the scaled case and solving for the ratio of scaled reference velocities yields;

$$\frac{U_s}{U_0} = \frac{L_0 \nu_s}{L_s \nu_0} \quad \& \quad \frac{U_s}{U_0} = \frac{L_s f_s}{L_0 f_0} \tag{2.11}$$

Equating the velocity ratios and solving for the scaled frequency yields;

$$f_s = \left(\frac{\nu_s}{\nu_0}\right)\left(\frac{L_0}{L_s}\right)^2 f_0 \tag{2.12}$$

Note that, scaled viscosity and the characteristic length depend on the experiment setup. It is easy to change the scaled frequency comparing to the operating medium and the wing model. Thus, flapping frequency is considered as the scaling parameter.

2.4 Bio-Aerodynamics

To design a wing mechanism, it is necessary to investigate the flapping animals. Especially hovering insects and birds are preferred by considering that the hover ability is a key design requirement for the future MAVs. This section mainly focuses on the wing trajectories of Drosophila fruit fly, hummingbird and smaller birds.

Birds usually flap their wings in vertical direction only. Flapping a wing in a free stream flow creates an effective angle of attack with a normal force vector containing both lift and thrust components. This phenomenon, namely *Knoller-Betz effect*, is first studied by Knoller in 1909 and Betz in 1912 ([31], [32]). Figure 2.5 gives the graphical results of the zebra finch wing span and wing tip variation [33]. Insects fly with various wing trajectories. This trajectories are usually named according to wing tip motion such as oval, figure of eight or pear-shaped trajectories [34].

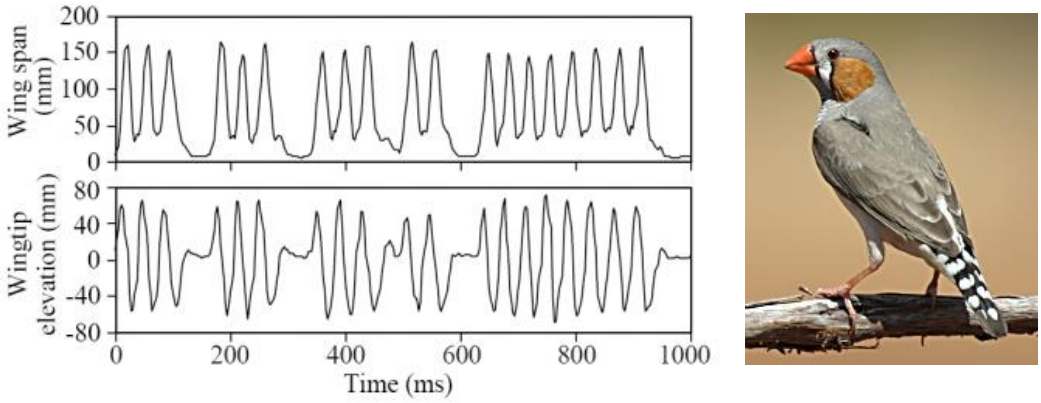

Figure 2.5 Wing kinematics (left) of a zebra finch (right) at 2m/s flight velocity (from Ref. [33])

Figure 2.6 shows the general flapping trajectory of Fruit fly at hover. Most of the insects use nearly horizontal stroke plane and with approximately equal and relatively high angles of attack for downstroke and upstroke.

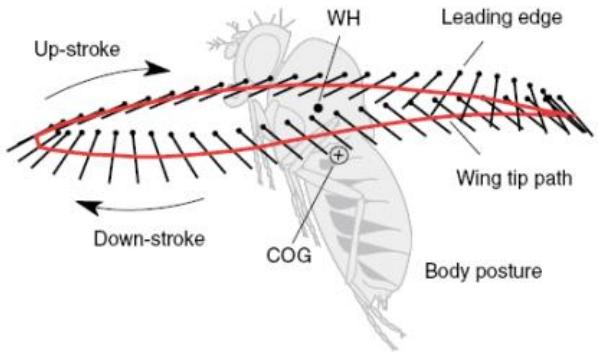

Figure 2.6 General wing trajectory of the Fruit fly (from Ref. [34])

Figure 2.7 illustrates the flapping trajectories of *Rofous* hummingbird, which is preferred for experimental measurement in the wind tunnel, for several different forward flight speeds between 0 – 12 m/s [35].

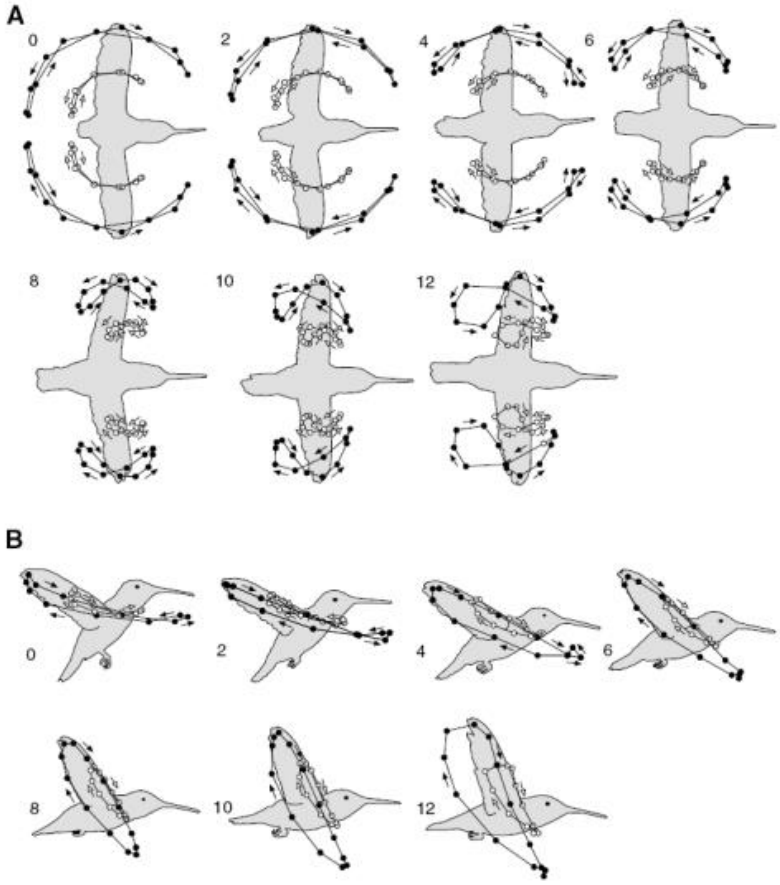

Figure 2.7 Flapping trajectory of hummingbird at velocities varying between 0 – 12 m/s (from Ref. [35])

2.5 Flapping Wing MAVs

Flapping MAVs mainly have three different types, namely MEMS, vibrating and mechanical flapping wings. Four MAVs, which are capable of performing controlled flights, are presented in Figure 2.8 as a base design for different flapping MAVs.

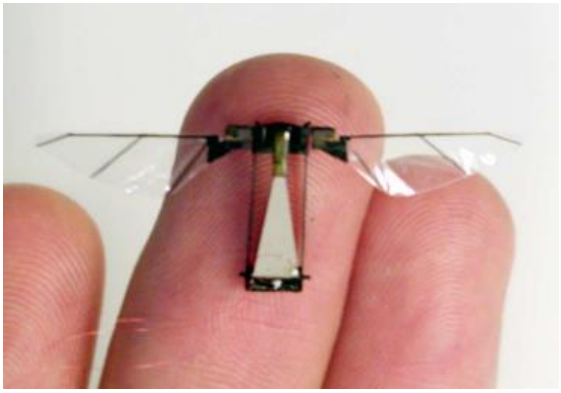

a) Robotic insect, Harvard University [36]

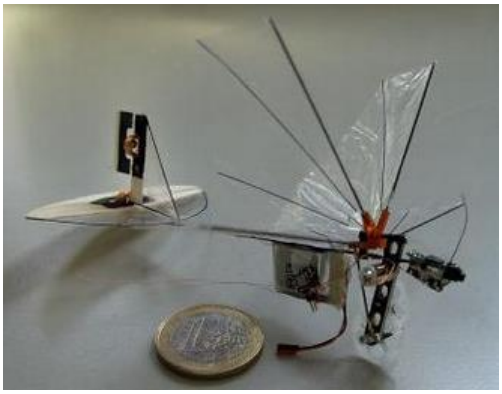

b) DelFly micro, TU Delft [37]

c) Delfly II, TU Delft [38]

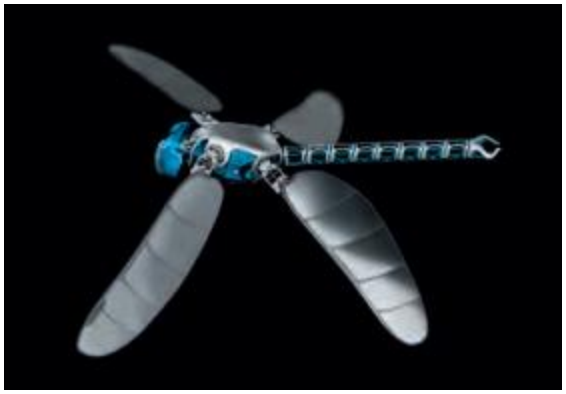

d) Bionicopter, Festo [39]

Figure 2.8 Different flapping MAV concepts

Robot insect (Figure 2.8 a), weighing 60 mg and has a span of 3 cm, is performed autonomous vertical flight successfully [40]. It uses wake vibrating wing mechanism to generate lift. Delfly Micro (Figure 2.8b) and Delfly II (Figure 2.8c) are similar MAVs, weighing 3.07-17 g and having span values of 10 – 28 cm respectively. They are capable of fully autonomous flight [41]. Wing motion of Delfly is based on clap and fling mechanism. Bionicopter (Figure 2.8d) is a tandem wing flapping air vehicle that is capable of flying autonomously including take-off and landing. It has a total

weight of 175 gr and total wing span of 63 cm. Although, Bionicopter cannot be classified as MAV, it is a promising design for future MAVs. Table 2.1 gives the general characteristics of four MAVs

Table 2.1 Flapping MAV specifications

MAV designation	Robot insect	Delfly micro	Delfly II	Bionicopter
Span [mm]	30	100	280	630
Mass [gr]	0.06	3.07	17	175
Flapping Frequency (Hz)	110	30	13-15	15-20
Wing Stroke (^{0})	$\pm 50^0$	$\sim 40^0$	$\sim 44^0$	$\sim 40^0$

2.6 Related Wing Mechanisms

In the previous parts, an insight to unsteady aerodynamics of the flapping wings is given. Also, the particular mechanisms that create additional force and the importance of flapping wing researches are mentioned. Although METU Aerospace Engineering Department already has two wing flapping systems, which can perform 2-D experiments with different airfoils, there is a need for a tandem flapping wing mechanism. Each wing of the new mechanism is expected to have a capability of performing 3 DOF rotational motion in order to simulate the 3-D experimental cases. In other words, an independently controlled tandem flapping wing mechanism that allows to use of any user-defined trajectory, adequate for PIV measurement, and capable of measuring lift and thrust is needed. Several wing mechanisms are investigated in order to design such a system.

Van den Berg's flapping machine, namely 'the flapper', uses differential gears that are embedded within the wrist mechanism [42]. The flapper can only control pitch and plunge angle. The mechanism is used in wind tunnel and only PIV measurement can be done with the system. Figure 2.9 shows a view from the wind tunnel experiment in order to investigate LEVs.

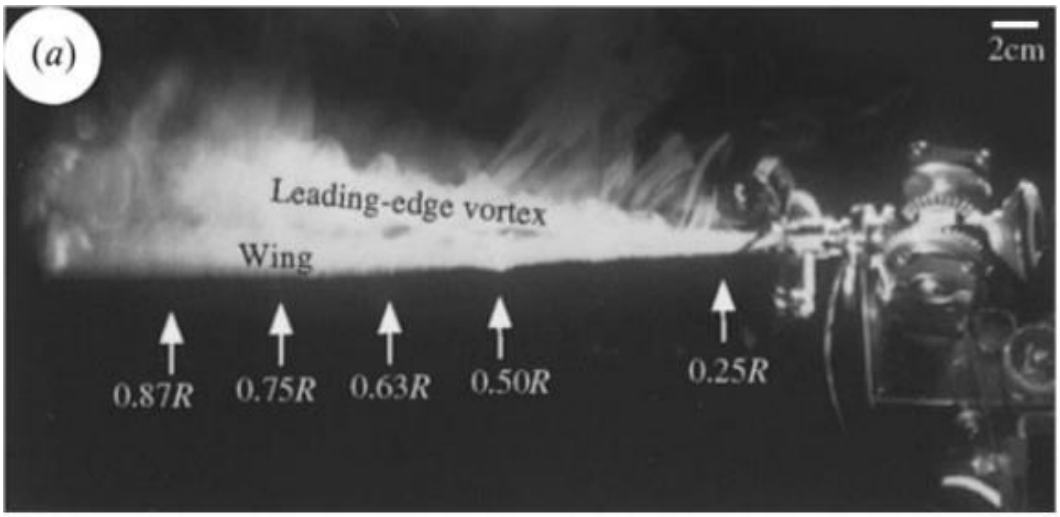

Figure 2.9 Van de Berg's flapper (from Ref. [42])

Smith's Moth Wing uses ball bearing like mechanism to give the rotational freedom in three axes ([43]- [44]). This system can be used in single and tandem wing condition (Figure 2.10) Wind tunnel test and force measurement can be done with the system. Also, flight test is possible.

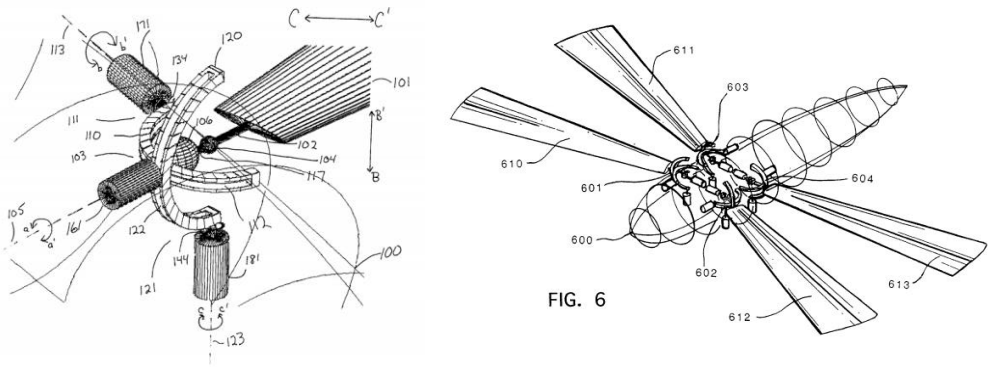

Figure 2.10 Smith's Moth Wing wrist mechanism (left) and tandem configuration (right) (from Ref. [43]- [44])

Winson Lai's flapping wing mechanism uses bevel gears that are mounted in a wrist mechanism to control the pitch axes and timing belt to control the plunge axes (Figure 2.11). Plunge motion (or rotation) is accomplished by mounting the system to another step motor and controlling the plunge axes with it [45]. This mechanism can control all three rotation axes separately and operates in the water. It is used with force

transducers. Figure 2.11 gives detailed information about the design of Lai's mechanism. Bulky design of the gear box and the motion transmission is the only drawback of the system. Timing belt probably causes the disturbance in the flow vicinity of the wing root.

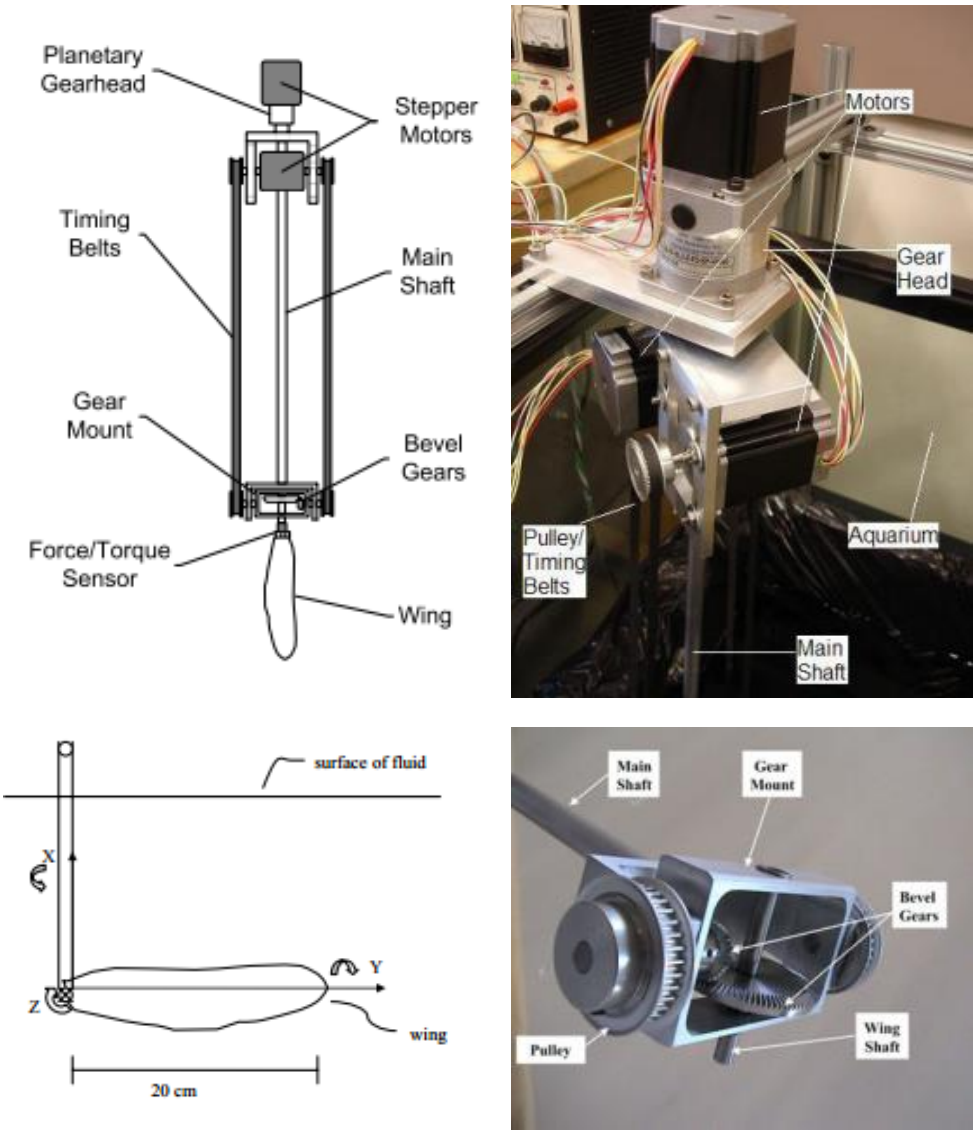

Figure 2.11 Lai's flapping wing mechanism (adopted form Ref. [45])

Morrison et. al [46] develop a flapping wing mechanism that is capable of performing 2 DOF pitch and plunge flapping motion. The system is equipped with multi axial force and torque sensor and used with water channel. Pitch and plunge motion are provided by bevel gears (Figure 2.12).

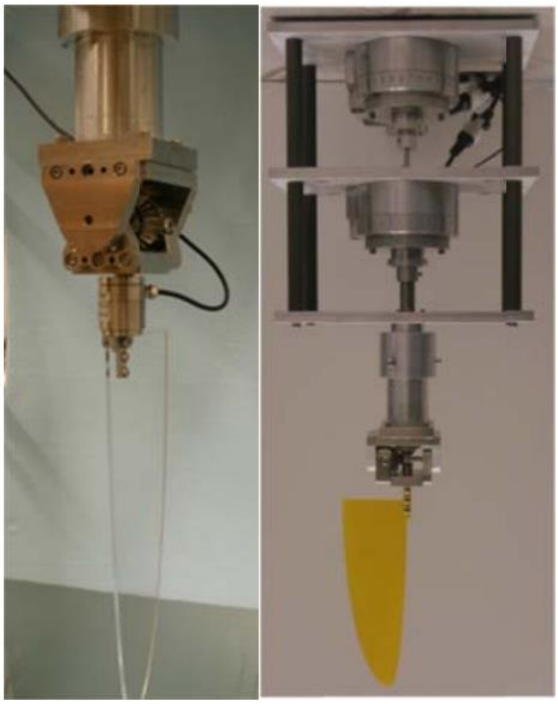

Figure 2.12 Morrison's flapping apparatus (from Ref. [46])

Dileo's experimental flapping wing is developed to mimic the dragonfly wing motions ([47], [48]). It has two rotational degrees of freedom and one degree of freedom in the flight direction. Both bevel gear and timing belt are used for each axes. Force measurement and flow visualization with PIV is available. Bulk wing model design can cause a disturbed flow field in vicinity of the interested measurement region (Figure 2.13).

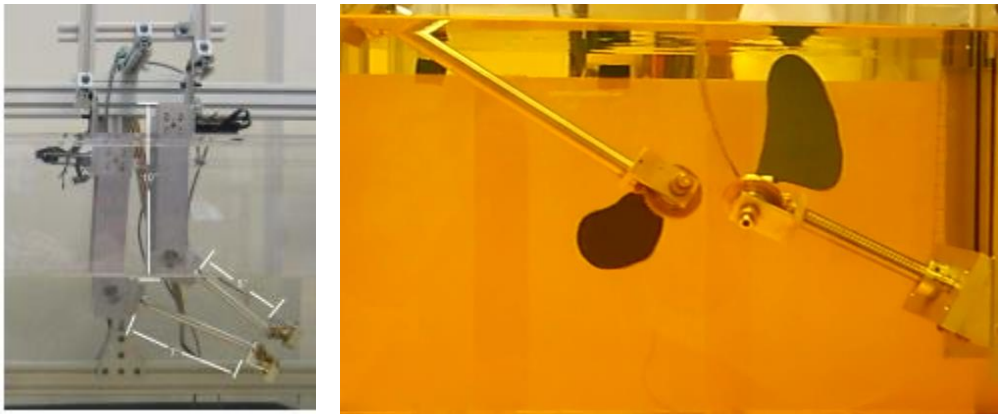

Figure 2.13 Dileo's Robotic model wing (from Ref. [49])

Maybury's flapping wing mechanism is similar to Dickinson's Robot-wings without linear motion ability [50]. It can be used for mimicking hovering flight of dragon fly and is able to perform force measurement during the experiments (Figure 2.14)

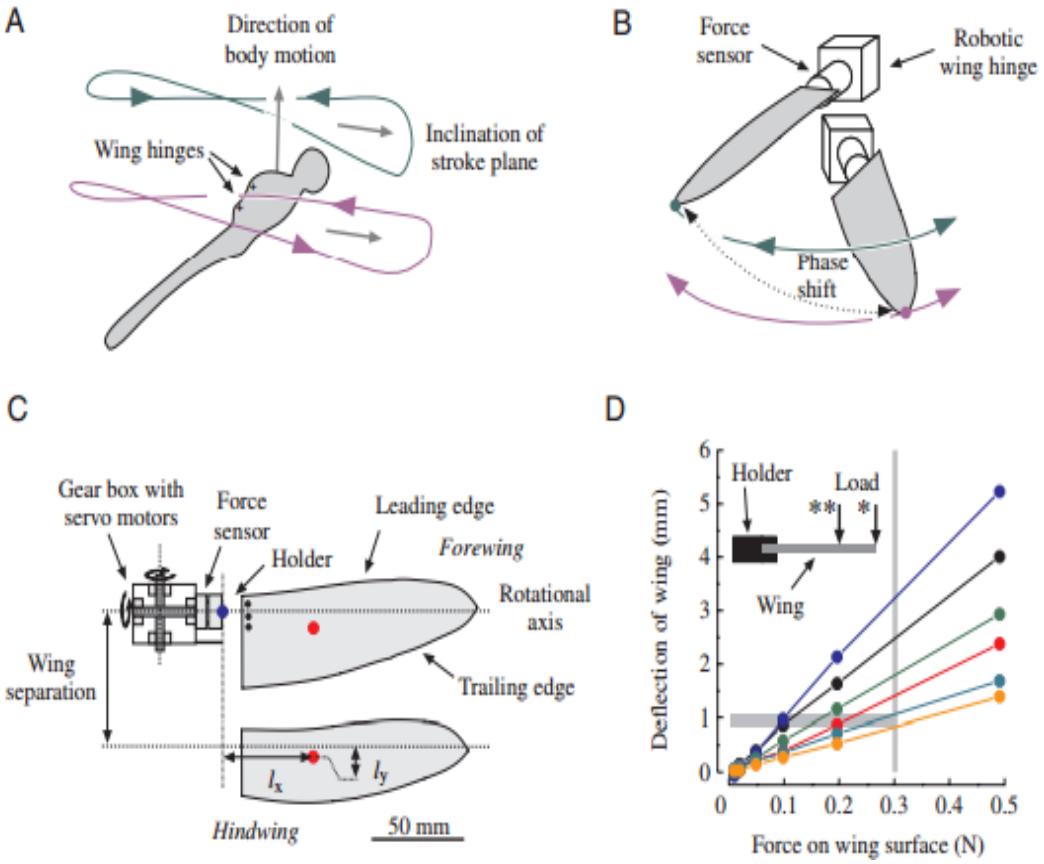

Figure 2.14 Maybury's flapping wing mechanism (from Ref. [50])

Dickinson's Robofly is a dual wing mechanism [27]. It has three rotational degrees of freedom at each wing and one linear degree of freedom in the flow direction. Thus, it does not need a water tunnel to generate free stream flow velocity. Rotational motion is given to pitch, heave and plunge axes by using bevel gears whereas plunge axis only uses timing belt. Both flow and force measurements can be done. Experiments are conducted in oil in order to match the similarity parameters. This mechanism is one of the most outstanding experimental setup. Eccentric transmission shafts, which are placed nested to each other, provide less disturbed flow field (Figure 2.15).

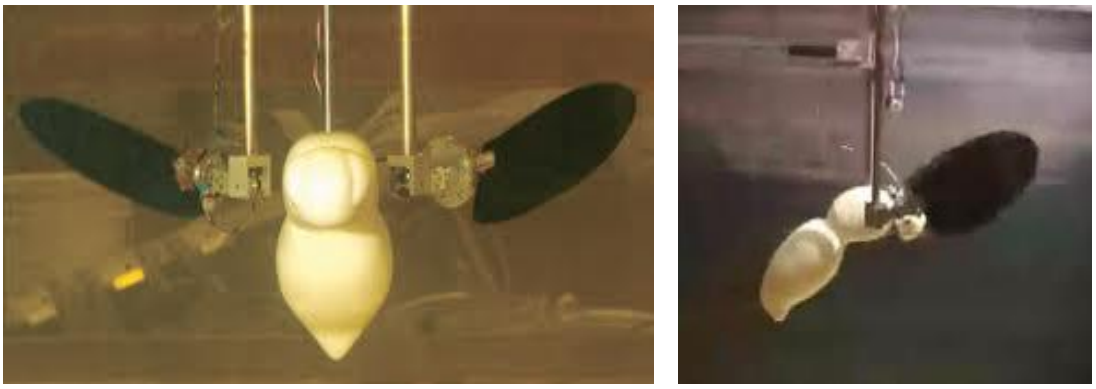

Figure 2.15 Robotfly performing hover flight of fruit fly (from Ref. [51])

Selected studies, which are using flapping wing mechanisms, provide a basis for a new flapping mechanism design. They have certainly influence on the design approach taken in this study. To sum up, general characteristics of the competitor flapping mechanisms are tabulated in Table 2.2

Table 2.2 Flapping test mechanism characteristics

Flapping Mech.	DOF	Flapping Frequency	Re	Operating Medium	Measurement System
Van den Berg's [42]	2	0.3 Hz	-	Air	PIV
Smith's [44]	3	-	-	Air	Force
Lai's [45]	3	0.5 Hz	-	Water	PIV
Morrison's [46]	2	0.2	7100	Water	Force
Dileo's [48]	5	~1 Hz	1160	Oil	Force - PIV
Maybury's [50]	6	0.6 Hz	137	Oil	Force - PIV
Dickinson's [18]	7	~0.7 Hz	160	Oil	Force – PIV

CHAPTER 3

FLAPPING MECHANISM

This chapter presents the design and technical futures of dual robotic flapping wing mechanism (Robot-Wings) [10], which is developed for use in laboratory experiments, such as aerodynamic performance of different wings, optimization of flapping trajectories. The mechanism is scaled by means of Reynolds number and Strouhal number. There exist two wings which can flap with the maximum angular velocity of 290deg/s. Each wing has three rotational degrees of freedom, which allows the adjustment of different flapping trajectories separately. Six computer-controlled brushless motors drive the three rotational axis of each wing, which are equipped with sensors for measuring the instantaneous aerodynamic forces. A special software and graphic user interference (GUI) are developed in order to control the Robot-Wings. The main objective of the software is to solve the coupled kinematic of the three rotation axes in order to obtain the desired motion trajectories. Hardware of each wing is embedded with three motor position readers, three custom made motor control circuits and a microcontroller unit.

3.1 System Design

Robot-Wings is designed to mimic the flapping wing motion (Figure 3.1). Each wing can perform pitch, heave and plunge motion around the x, y and z-axes. Rotation by θ around the z-axis is referred to plunge angle; rotation by β around the y-axis is referred to heave angle; and rotation by α around the x-axis is referred to pitch angle. Wings are capable of performing flapping motion in different mediums such as air, water and

oil. Compact gear-box design minimize the flow distribution in vicinity of the wing. Lift and Drag force can be measured via force and torque transducer that are placed between wing and gear-box. Dynamic scaling of the system is performed by means of Reynolds number and Strouhal frequency. Hence, dimensions of the system are determined.

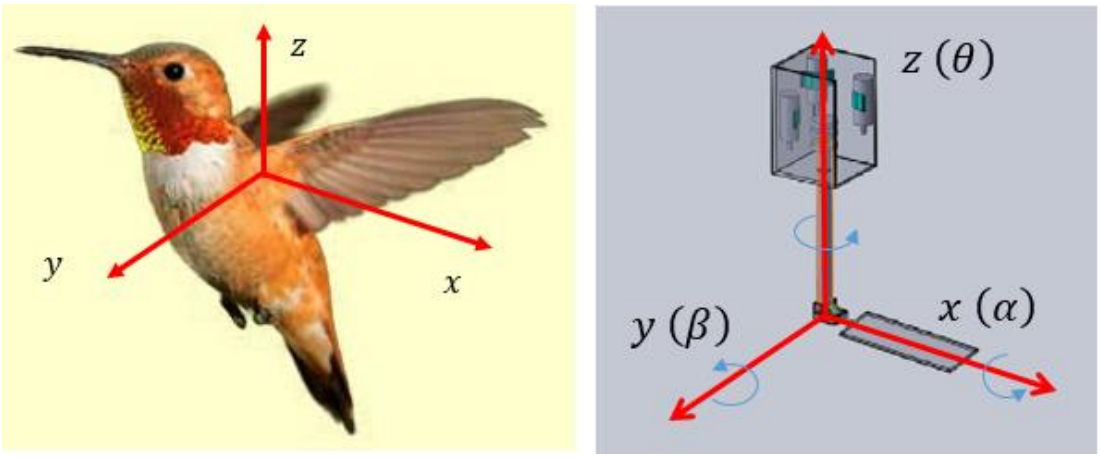

Figure 3.1 Hummingbird and Robot-Wings principle axes placement

Robot-Wings is capable of performing arbitrary flapping trajectories with six-degree-of-freedom. Position and velocity limits at each axis are presented in Table 3.1. Maximum angular rates are calculated by considering the motor specifications. However, using maximum rates can damage the system or the sensors on the wings. That's why, speed limitations are set via software.

Table 3.1 Robot-Wings motion limits

	with Load Cell	***without Load Cell***
$\boldsymbol{\alpha}$	$\pm 90^{0}$	$\pm 180^{0}$
$\boldsymbol{\beta}$	$+45^{0}/-90^{0}$	$+45^{0}/-225^{0}$
$\boldsymbol{\theta}$	$\pm 180^{0}$	$\pm 180^{0}$
$(\dot{\alpha})_{max.}$	$160^{0}/s$	
$(\dot{\beta})_{max.}$	$290^{0}/s$	
$(\dot{\theta})_{max.}$	$290^{0}/s$	

3.2 Mechanical Design

The Robot-Wing is designed to be used with water tank or tunnel, also it is possible to use the mechanism with wind tunnel. Thus, most of the mechanical parts are used partially or fully submerged in the water. Thus, they are manufactured either stainless steel or aluminum. The flapping wing mechanism has two identical wing modules, which are composed of three main sub parts, namely the mechanical wrist, transmission shaft, and the motor box. An integrated force and torque sensor is placed in between the mechanical wrist and the wing. Rotational motion is transferred from the motors to the wing by means of timing belts, pulleys, transmission shaft and bevel gears. Moreover, a control box module is used for the data acquisition, system control and wing modules powering.

3.2.1 Mechanical Wrist and Gearbox Design

Each wing module has a coaxial mechanic arms fully submerged in to water during the experiment. Mechanic arm is connected to the motor box via transmission shaft. It consist of two bevel gear (blue) in order to maintain plunge control and three different (green) for controlling the pitch axis (Figure 3.2).

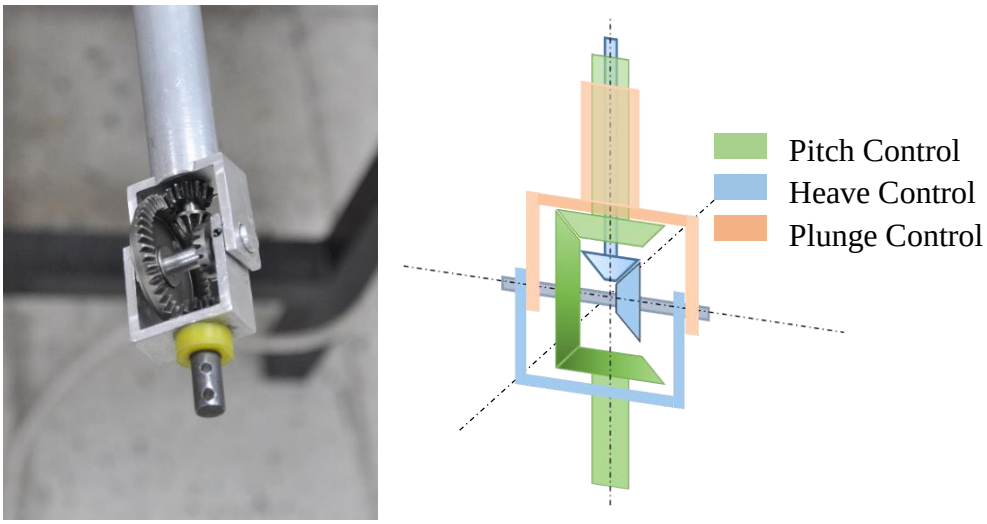

Figure 3.2 Mechanical wrist and gear box assembly (left) with illustrated explanation of gear and rotation axes assignment (right)

3.2.2 Transmission Shaft

The transmission shaft is being assembly of three coaxial shaft. Plunge motion control shaft is the inner shaft, pitch motion is controlled by the middle shaft and the plunge motion is controlled by the outer shaft. A bevel gear is attached to the both inner and middle shaft from the wrist side. On the motor box side, all shafts are attached to the pulleys. Bevel gears are adapted form radio controlled model car differential gears. The outer shaft is directly connected to aluminum 'U' part of the wrist. All shaft are supported by using ball bearings between each other.

3.2.3 Motor Box

This part acts like a support for the transmission shafts, mechanical wrist and the wing. It is connected to heavy profiles via M8 bolts by doing so mechanical vibrations are avoided. Three brushless MAXON DC motor with integrated encoders are used to drive the coaxial arm. Three mechanical couplings are being connected to each motor. Also, the motor motions are transferred to the transmission shafts by using a timing belts (Figure 3.3).

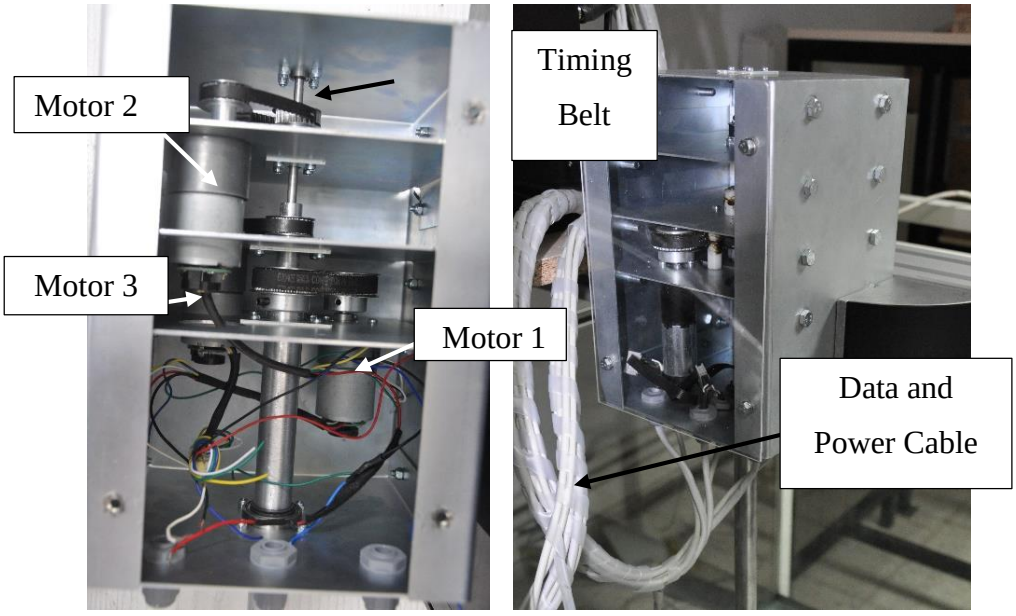

Figure 3.3 Motor box of the robotic flapping wing mechanism

3.2.4 Control Box

Wing modules are connected to the Control-Box. It can be connected to PC via two separated USB cable one for each wing (Figure 3.4). Control-box contains a 12V power supply, six motor driver, two PIC based micro controller circuit for data acquisition, and an embedded 2 GB memory for necessary drivers. Moreover, it has an emergency power cut switch on the front panel.

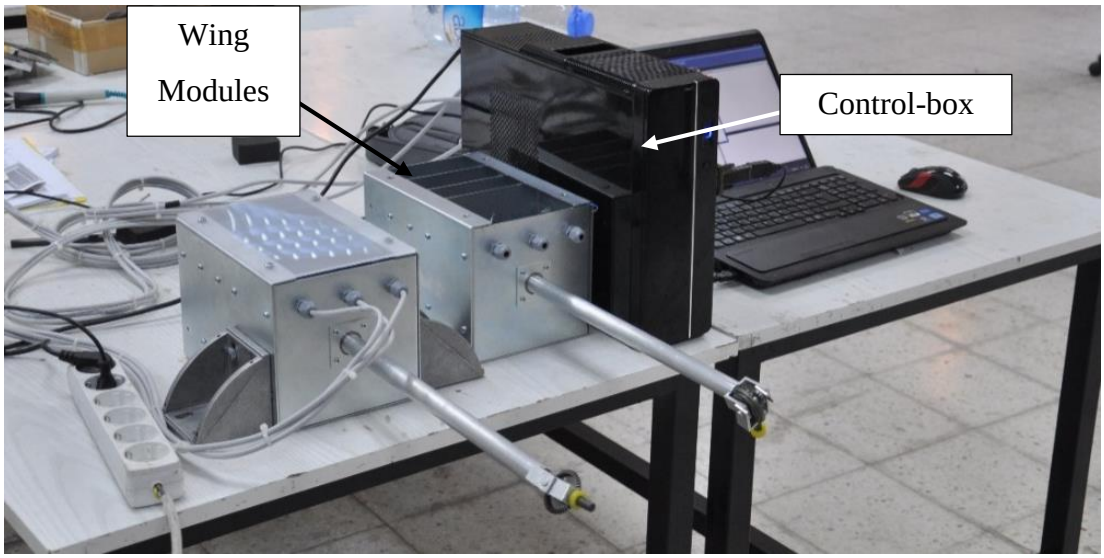

Figure 3.4 Two wing modules and Control-Box

3.3 Motion Kinematics

Wing motion can be defined in three different form – sine, ramp and step functions by means of amplitude 'A', period 'T', offset, phase angle 'φ', delay 'D' and duration. Sinusoidal function that defines the wing motions is given below. Offset is initial angular displacement from the origin and delay is used for starting a motion after a while. They are given as input via software, if necessary.

$$\zeta_{w,sine}(A, D, T, \varphi, t) = A * \sin(2\pi t/T + \varphi) + D \qquad (3.1)$$

Each wing capable of performing three motions, namely pitch, heave and plunge motions by using three electric motors. Motion transmission between wing and motor is provided by timing belt, transmission shaft and gear-box. Thus, a conversion matrix between motor motion and wing motion is necessary in order to solve the complex coupling of the rotation axes.

$$\begin{bmatrix} -1 & -3.308 & 1 \\ 0 & -1.8 & -1 \\ 0 & 0 & 1 \end{bmatrix} \begin{bmatrix} \alpha_w \\ \beta_w \\ \theta_w \end{bmatrix} = \begin{bmatrix} \alpha_m \\ \beta_m \\ \theta_m \end{bmatrix} \tag{3.2}$$

$$[C] \begin{bmatrix} \alpha_w \\ \beta_w \\ \theta_w \end{bmatrix} = \begin{bmatrix} \alpha_m \\ \beta_m \\ \theta_m \end{bmatrix} \tag{3.3}$$

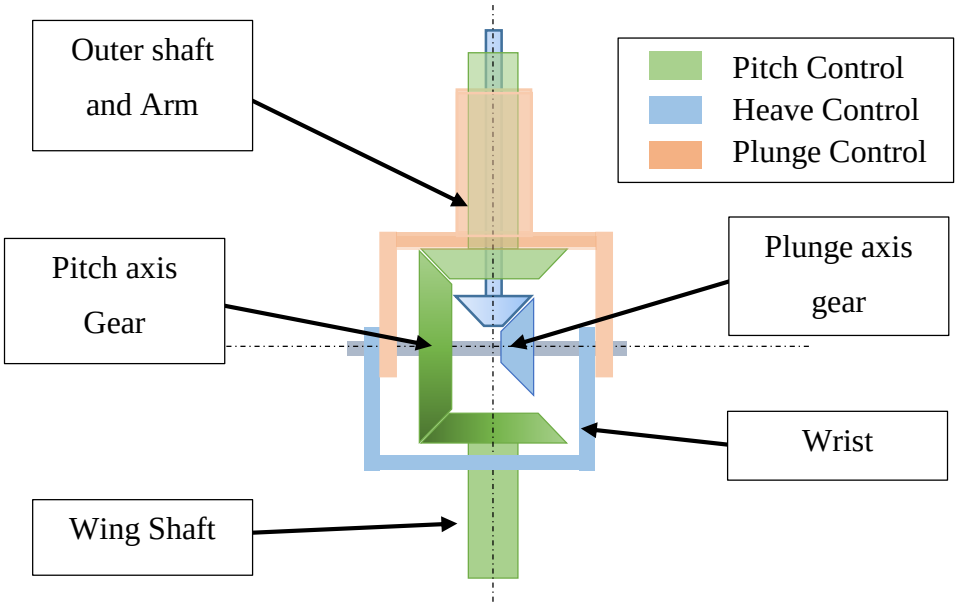

Figure 3.5 Mechanical wrist and gear box parts

Using concentric transmission shafts is causing coupling between the axes. Since the wrist mechanism is attached to the outer transmission shaft, it rotates with the outer shaft whereas the other shafts stays stationary. However; the bevel gears that are driving the pitch and plunge axes are also attached to the mechanic wrist (Figure 3.5). So, in order to prevent the unintentional pitch and plunge motion, inner and mid shafts

must rotate with the outer shaft providing that the relative angular velocity between shafts are zero. Moreover; pitch shaft rotates around plunge axes with the rotating plunge axes, which causes a coupling between plunge and pitch axes. Lastly, pitch axis is not coupled with other axes. In other words, generating a pure pitch motion only requires using pitch motor whereas generating a pure plunge motion requires using all three motor working at the same time (Figure 3.6). Phase difference and delay given as zero in the cases that are presented. Figure 3.7 shows the wing tip trajectory during a pure pitch motion around a rotation axis at c/2.

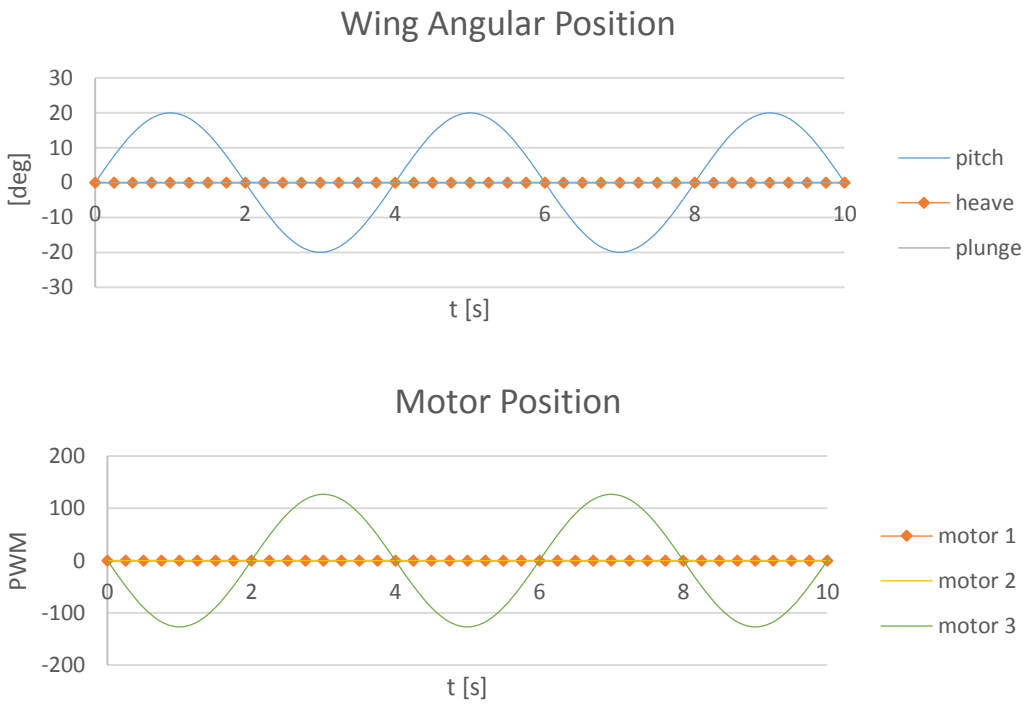

Figure 3.6 Wing and Motor position for a pure pitch motion of A=20º and T=4s

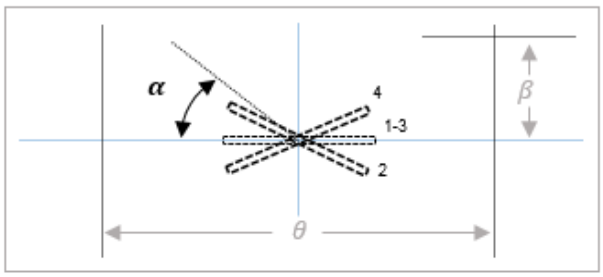

Figure 3.7 Wing tip trajectory for a pure pitch motion of A=20º and T=4s

Figure 3.8 shows the desired wing trajectory for a sinusoidal plunge motion and necessary motor inputs. It is seen that motor 2 rotates in opposite direction compared to motor 1 and motor 3 due to odd gear number on the plunge axis.

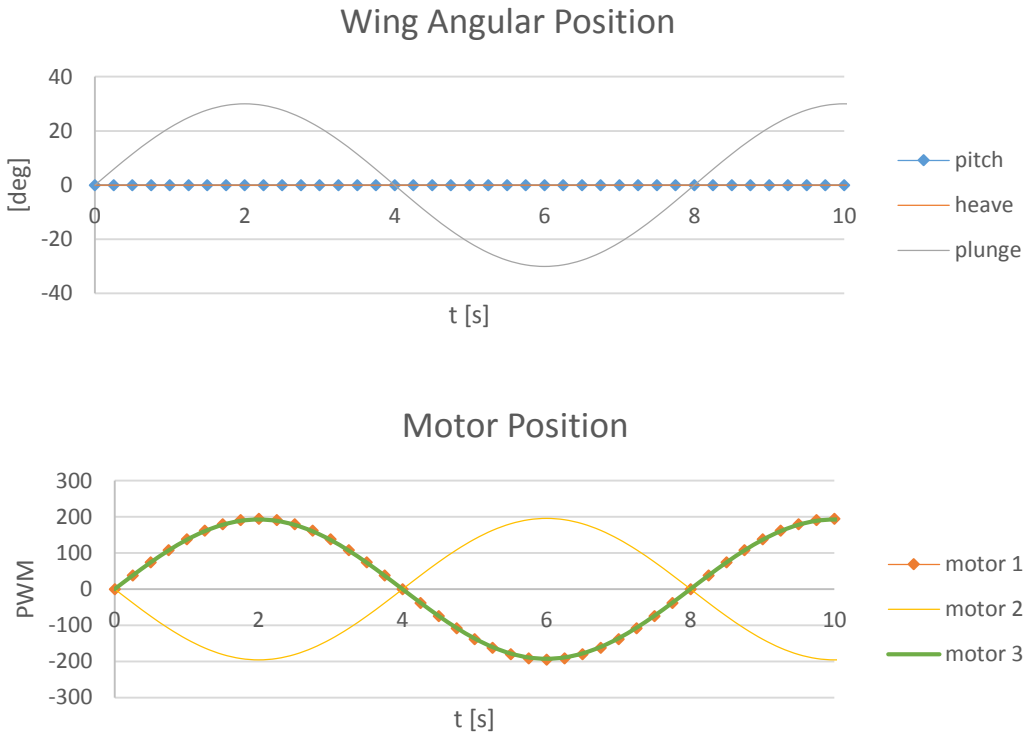

Figure 3.8 Wing and Motor position for a pure plunge motion of A=30º and T=8s

Wing tip trajectory for a pure sweep motion with zero angle of attack is presented in Figure 3.9

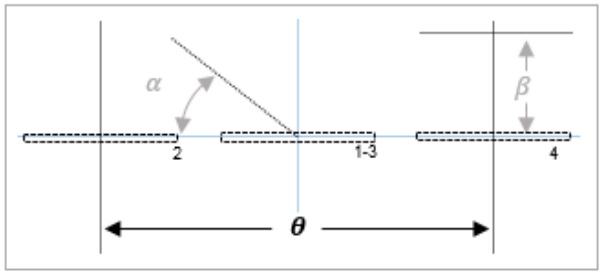

Figure 3.9 Wing tip trajectory for a pure plunge motion of A=30º and T=8s

Simultaneous use of two or three axes require much complicated motor motions. Figure 3.10 shows motor and wing positions for a figure of eight motion with variable

pitch angle. Wing tip trajectory of the motion is illustrated in Figure 3.11. Furthermore; Figure 3.12 shows the wing and motor positions for a constant pitch angle figure of eight motion. Note that, pitch motor still continue to perform complex motion due to coupling of the axes. While wing performs simple sinusoidal motions, three motors perform much complex combined sinusoidal motions.

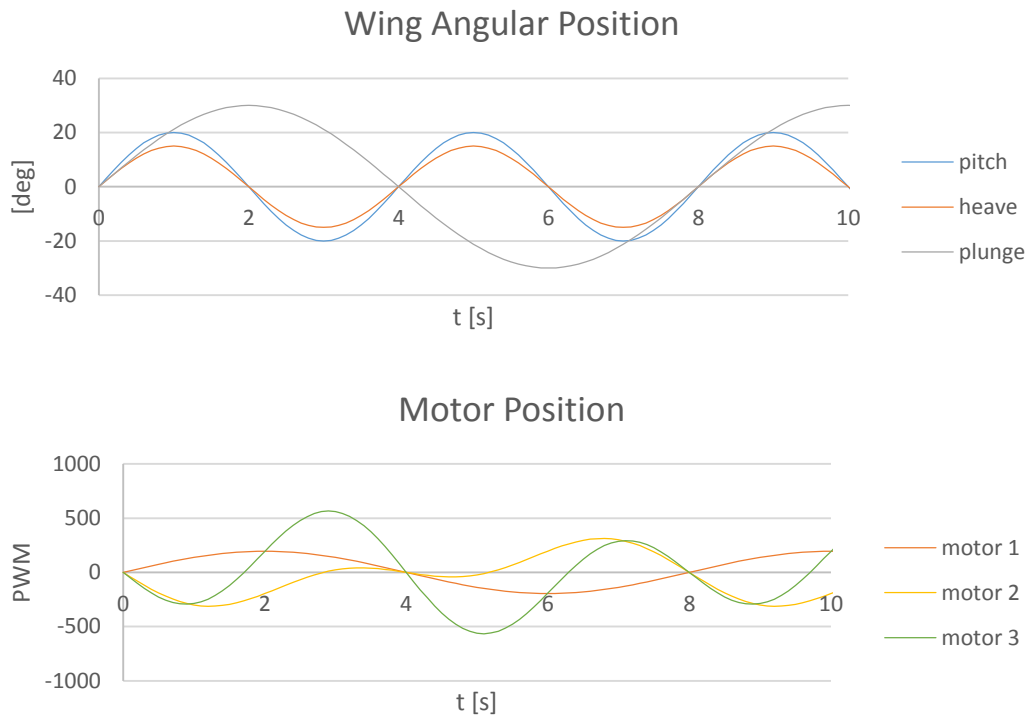

Figure 3.10 Wing and Motor position for a combined pitch, heave and plunge 'figure of eight' motion of A=20º, 15º, 30º and T=4s, 4s, 8s

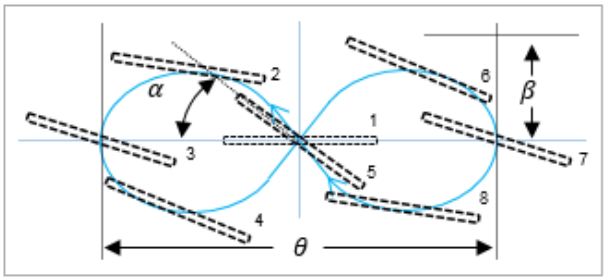

Figure 3.11 Wing tip trajectory for a combined pitch, heave and plunge 'figure of eight' motion of A=20º, 15º, 30º and T=4s, 4s, 8s

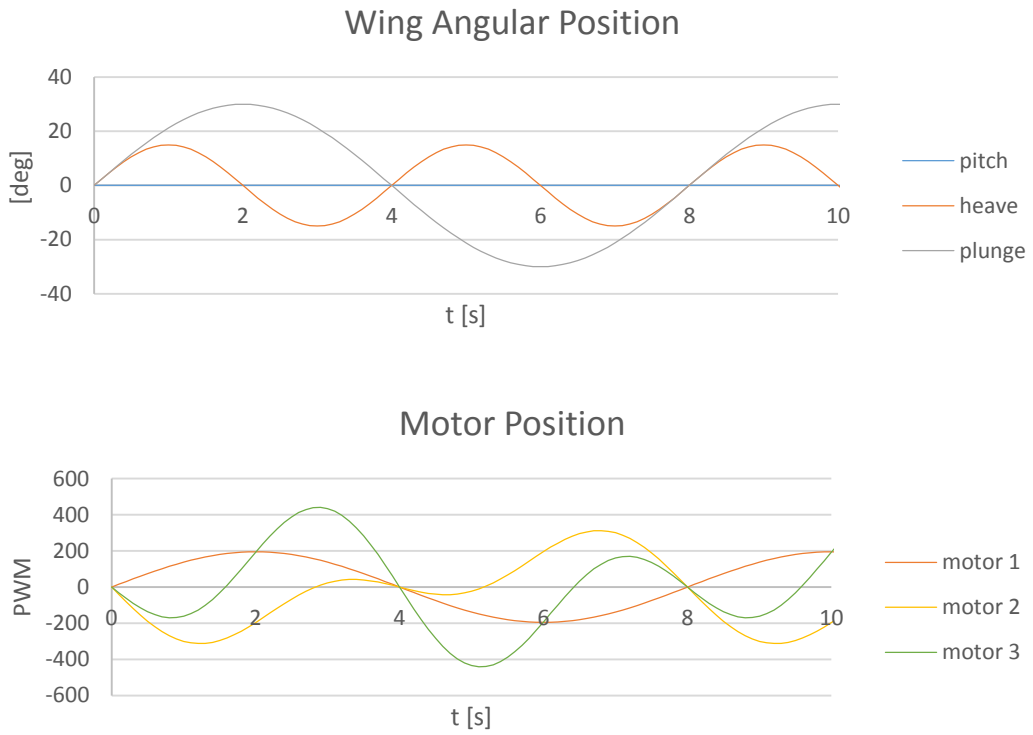

Figure 3.12 Wing and Motor position for a combined heave and plunge 'figure of eight' motion of A= 15º, 30º and T= 4s, 8s

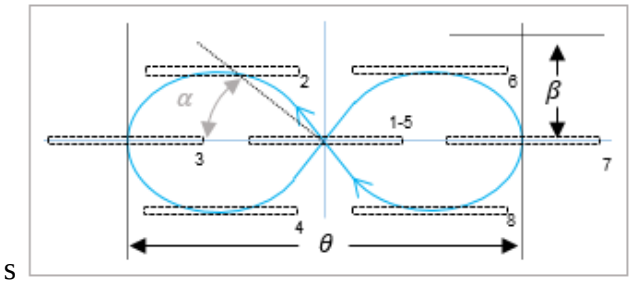

Figure 3.13 Wing tip trajectory for a combined heave and plunge 'figure of eight' motion of A= 15º, 30º and T= 4s, 8s

In order to obtain any user defined trajectory, coupling of axes must be solved simultaneously during the motion. Actually, control-box simultaneously converts the desired wing trajectory data to motor position data by use of coupling matrix. Also, the system can transform the data obtained from the encoders to necessary wing position data to check the error of the system input and output.

3.4 Hardware development

The Mechanism has two wings, and three custom made MAXON motors, position reader and motor drivers for each wing. Two microcontroller circuits, which are placed in to a control box, are used to control the wings (Figure 3.14). Wing-Sim, which is an in-house software created for the Robot-Wings, calculates the necessary motor motions for user defined wing positions. This is done by multiplying a motor position-coupling matrix, given in Eq. 3.2 with the position vector (α, β, θ) of the wing axes. The resulting vector is the position of the three motors. These values are sent to microcontrollers constantly throughout the system runtime since the memory of the microcontroller is limited. The computer also takes the feedback from the microcontroller (motor positions), converts it to axes positions (multiplying by a motor-decoupling matrix). After that, Wing-Sim plots the both input and output position of the each axis on the screen simultaneously. Hence, wing motions can be watched during the experiment. Besides that, after the experiment is done, the Wing-Sim also saves the output in excel format and prints graphics of "experimental positions vs. time" and "desired positions vs. time". Hence, position data can be investigated after the experiment.

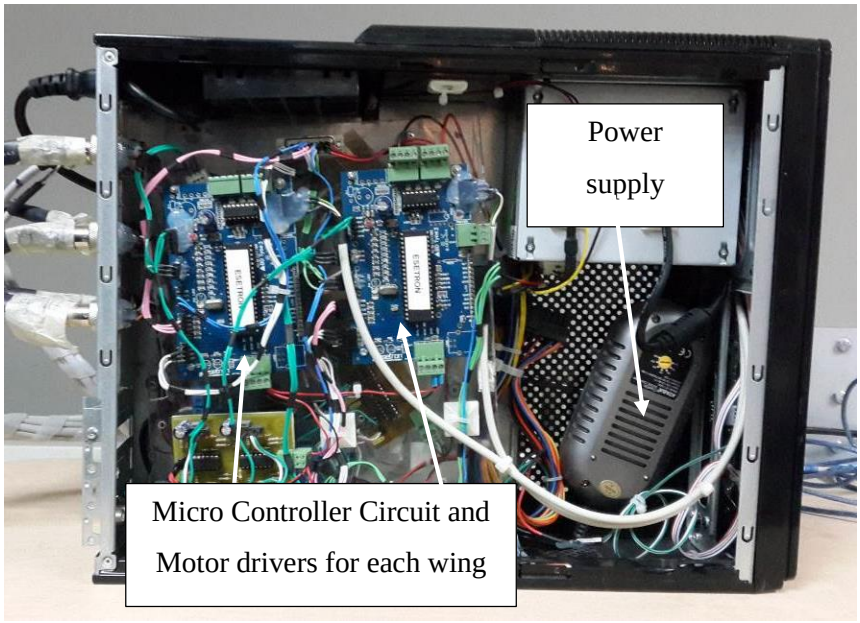

Figure 3.14 Control-box internal view

PIC16F777 microcontroller is chosen since it has 3 PWM outputs to control the 3 motors. Position data ‘encoder count’ of each motor is read by microcontroller via position readers. Wing motions are controlled by using position feed-back and desired position values. P- Controller (Proportional Controller) is used to control the motions. Position errors of the axes are calculated during the motion continuously.

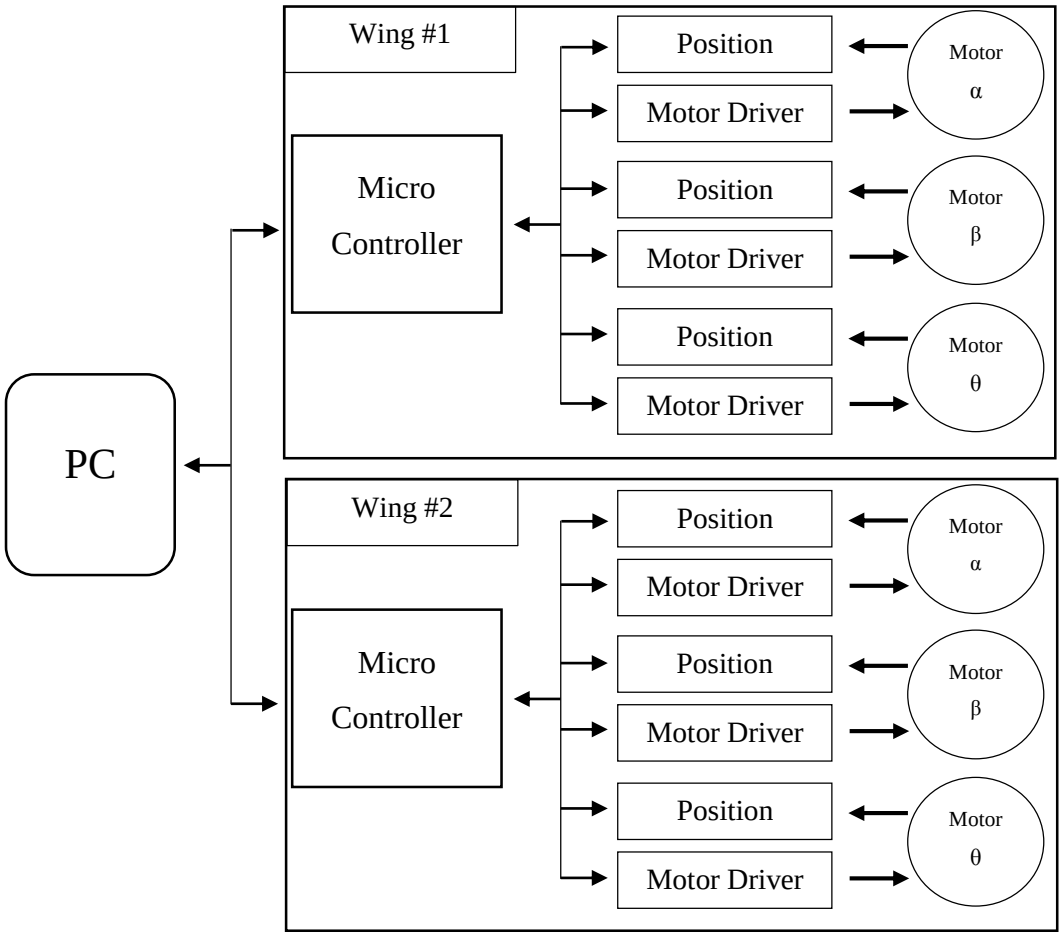

Figure 3.15 Hardware block diagram

A PWM response is created for each motor accordingly to position errors. The position reader consists only of a single PIC16F628A. It just reads encoder data of one motor and sends the value to microcontroller when requested. Motor driver is an integrated circuit that is developed for the mechanism. It can drive one motor in two direction up to 2.5 A and 12 V.

3.5 Software development

Microcontroller uses two data buffers for each motor. In case of absence of position data, data from old buffer can be used for input position calculation. Each time the motor starts using data of one buffer, the computer starts sending the data to a new buffer. Therefore the control is never interrupted and the microcontroller always knows where the motors are expected to be. The communication algorithm is shown in Figure 3.16.

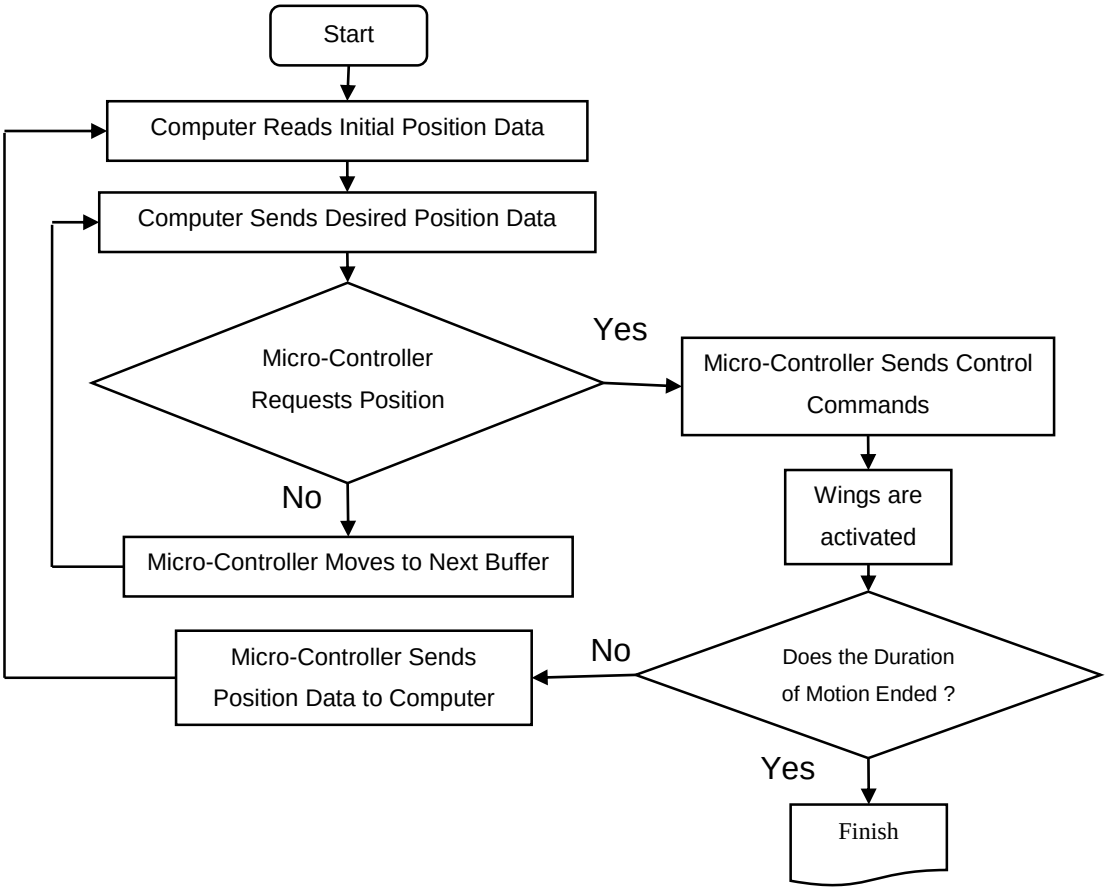

Figure 3.16 Communication flow chart

P – constant for each motor is determined experimentally. Each motor should be able to overcome aerodynamic or hydrodynamic force that is generated by the wing and friction force between the gears and shafts. System requires different P – constant calibration for different operational mediums such as water, oil and air, and also for

different wings. Proportional controller gives nearly good responses above the motors' threshold value. However, it couldn't compensate the small values. Therefore, it is necessary to use a piecewise function for the Pulse-Width Modulation (PWM) outputs. If the error goes below a certain ε_1 value, PWM stays constant at a minimum PWM value. It is also necessary to define a stability condition. If the error goes below another threshold the function becomes zero, PWM signal simply decays to zero. (Figure 3.17)

$$\psi(\varepsilon) = \begin{matrix} 0 \ , \ \varepsilon \leq \varepsilon_0 \\ \psi_1 \ , \ \varepsilon \leq \varepsilon_1 \\ K_p\varepsilon \ , \ \varepsilon > \varepsilon_1 \end{matrix} \tag{3.4}$$

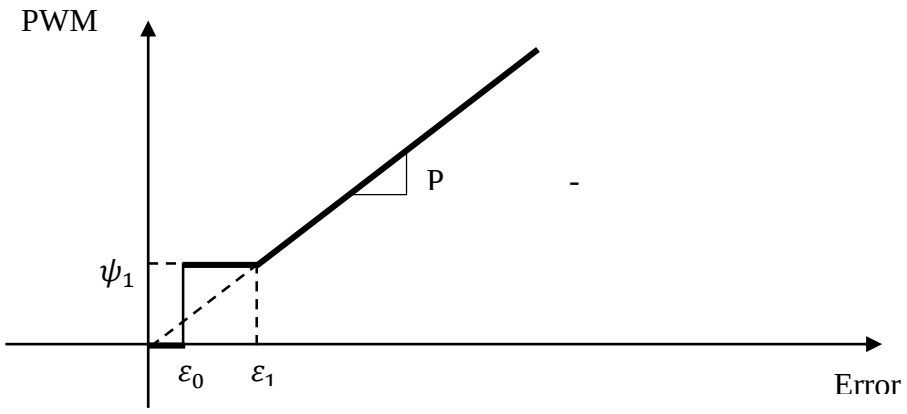

Figure 3.17 PWM signal versus position error

3.6 User Interface Development

A software called Wing Simulator (Wing-Sim) is developed in order to operate Robot-Wings. Experiment cases can be saved to the internal memory within the control-box. Initial position of the wings can be arranged before the experiment and wings automatically return the initial position after the experiment is completed. Type of the functions that defines the flapping frequency can be chosen as sine, ramp or step function. Amplitude, period, offset, phase difference, delay and the motion duration can be specified for each wing independently. Also, Wing trajectories can be

monitored during the motion. Furthermore; all position data can be logged and extracted in Excel format.

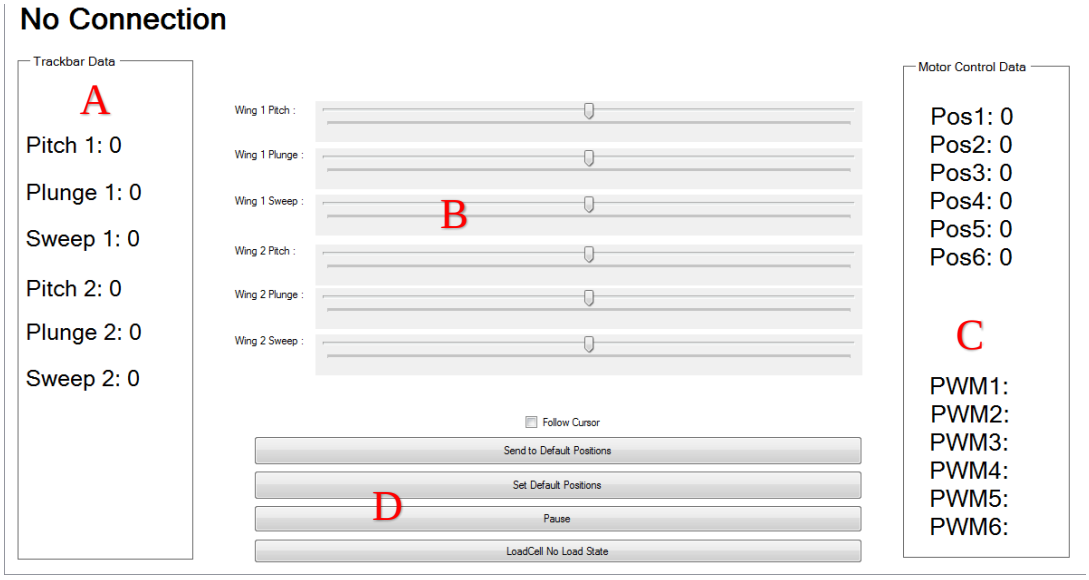

Figure 3.18 Wing-Sim position settings menu

Position settings menu enables setting initial position of both wings (Figure 3.18). Connection status of the wings can be monitored before the experiment. Block-A of Figure 3.18 shows angular position of the wings. Block-B of Figure 3.18 is the cursor block, which provides control over the wing axes simply sliding the cursers. Block-C of Figure 3.18 is the motor position block. It shows the angular position of the motors and the PWM signal for each motor. Finally, Block-D has control commands, such as: setting initial position, returning the initial position, and limiting the rotational motion in case of force transducer usage in order to avoid any damage on the cables that are used for force transducer.

Another important menu is the advance setting menu (Figure 3.19). By using the advance setting menu proportional constants of each axes can be changed independent from each other. Also, sampling time of the system can be set from this menu. Furthermore, a backlash parameter is defined for each axes. Since, the backlash is introduced while the directional changes. If an additional angular movement, equal to backlash uncertainty, can be added to motion kinematics, it can solve the backlash

problem. However, it needs precise initial position arrangements. Also, measuring backlash is not easy. Finally a minimum PWM value can be specified for the axes.

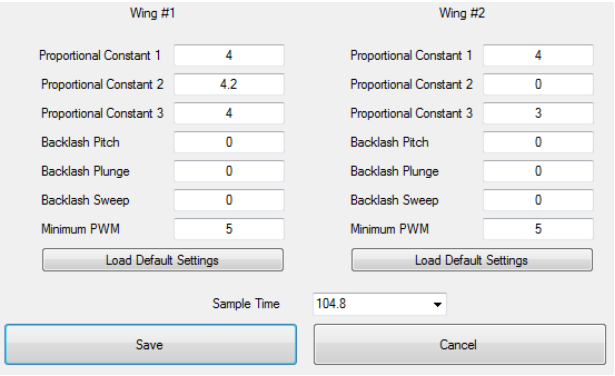

Figure 3.19 Advance setting menu

Trajectory setting menu enables activation or deactivation of any axes. Also, motion function can be defined from the Block-A of Figure 3.20. Moreover; various Amplitude, period, offset, phase difference, delay and the motion duration can be specified for each axis independently (Block B of Figure 3.20). Finally, motion can be started by pushing the execute button.

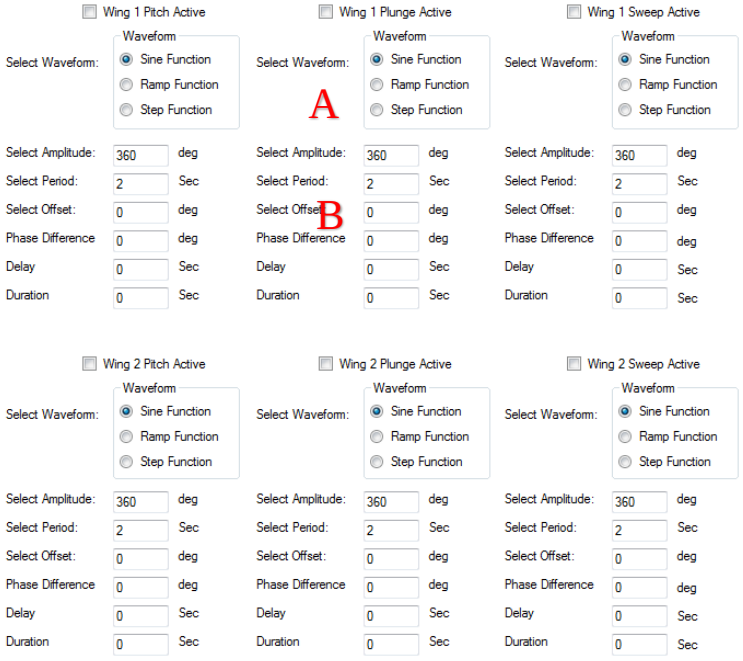

Figure 3.20 Trajectory setting menu

Motion tracking menu provides graphical illustration of each axes angular position with actual and desired trajectory values (Figure 3.21). All graphs are plotted in real-time during the experiment and logged automatically.

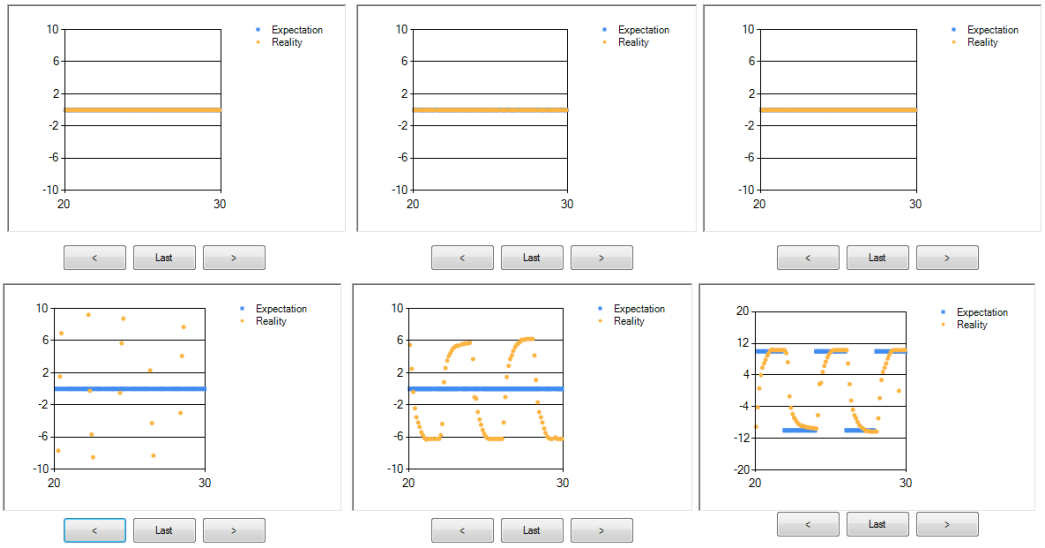

Figure 3.21 Motion tracking menu

Calibration procedure of the Robot-wings are explained in the Chapter IV and the results of the calibrations test are presented in Chapter VI

CHAPTER 4

EXPERIMENTAL METHOD

Experiments are conducted in the Aerodynamics Laboratory at the Department of Aerospace Engineering of METU. A special experiment room, which has purified water source to fill the water tanks and drainage to empty them, is constructed inside the laboratory. Purified water source and water exhaust are vital for water tank experiment setups. Three different size water tanks are placed in to experiment room. 0.8mx0.8mx2m water tank is used in the experiments. A computer controlled positioning system allowing to wings to perform rotational motions in three axes is used. A bio-inspired wing with 3 mm thickness is used. The flapping motion is carried out in zero free-stream velocity. Force measurement during the experiment is done by using ATI NANO17 IP65/IP68 transducer. Since the transducer is attached to the wing, measurements are transformed from wing fixed frame to inertial frame. Weight of the wing is extracted from the total force, in order to get the final results.

4.1 Experimental Setup

In this part, a comprehensive explanation of the experimental setup is given with detailed illustrations. Important elements of the experimental setup, which are the wings, water tank, operating medium, flapping mechanism, end the data collection unit, are explain. Characteristics of these parts are extremely important for analyzing the data and obtaining meaning full results. Thus, each element of the experimental setup carefully design or chosen for the current experiments. Finally schematic of the complete setup is shown and explained briefly.

4.1.1 Wing Models

A carbon fiber replica of the *Zimmerman* wing, which is used by Morrison et. al [46], is manufactured in order to compare the measurements of the system. Original wing has 241 mm wings span, 79 mm wing root chord and 2.7 mm wing thickness. Two quarter ellipse sharing a major axis passing through wing quarter chord are used for creating the Zimmerman wing planform area shape. New wing has thickness of 3 mm and it is fabricated from multi axial carbon fiber fabric (Figure 4.1). ATI NANO17 is attached to wing from leading edge. Wing fixed x-y-z axes are aligned with the sensor x-y-z- axes. Flapping axis of the wing is placed approximately 70 mm away from the wings root chord.

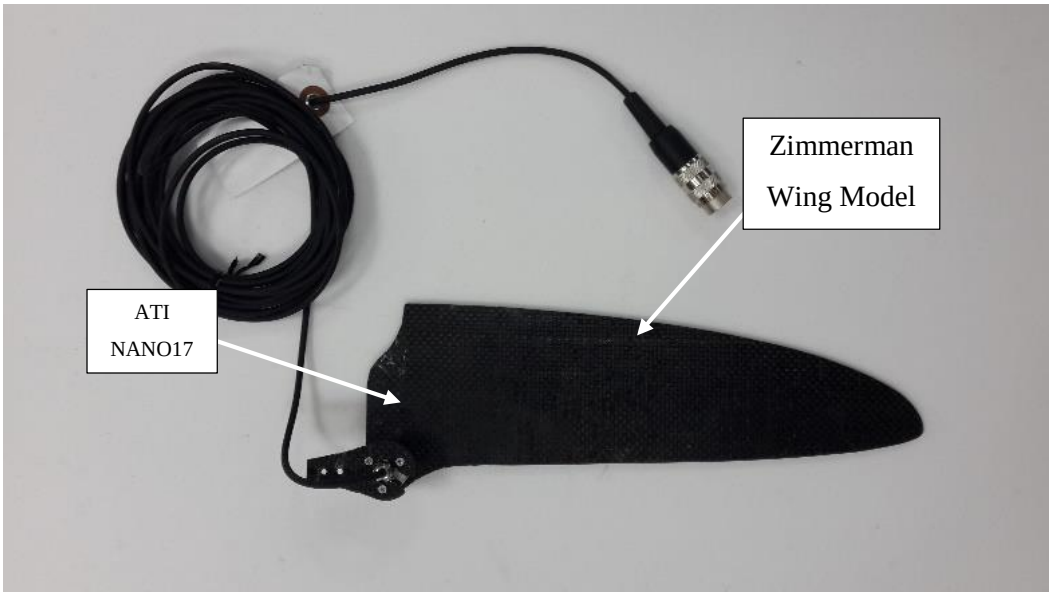

Figure 4.1 Carbon fiber wing model installed with ATI NANO17

Moreover, two different airfoil, namely with NACA0006 and 5% thick flat plate, are manufactured for PIV usage in future studies (Figure 4.2). Both airfoils have 6 cm chord and 18 cm span. Wings are fully submerged in the water during the experiments. Each airfoil has a pair in order to investigate the dual wings cases, such as, tandem wings and Weis-Fogh. Wings can be mounted to mechanism from LE, c/4 chord or c/2 chord locations. Each wing made of acrylic material, which is being transparent. Acrylic material is suitable for PIV experiments.

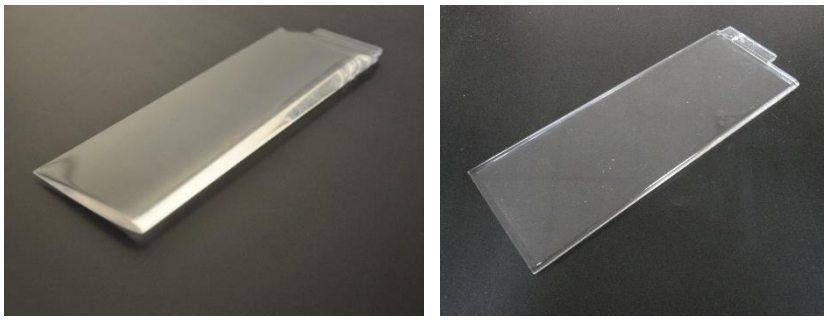

Figure 4.2 Acrylic wings with NACA 0006 (left) and 5% flat plate (right) airfoil

Wing root chord is being 6 cm away from the rotation origin, when the wings are connected with force transducers (Figure 4.3).

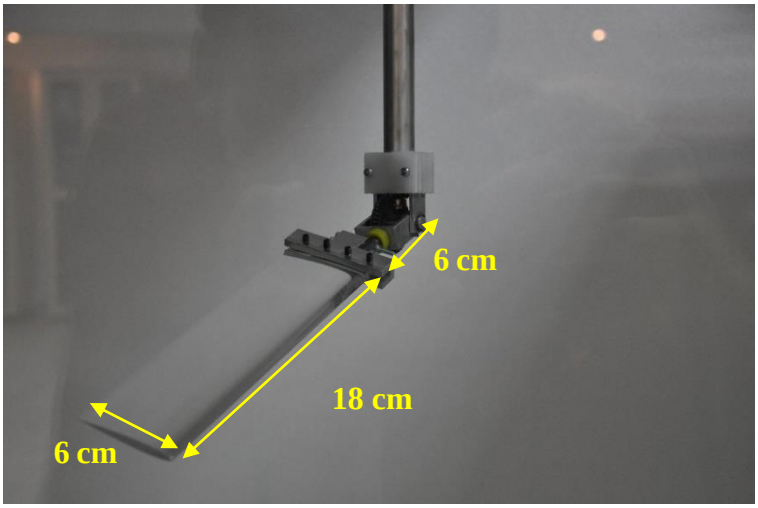

Figure 4.3 NACA0006 wing model connection to the mechanism

4.1.2 Water Tank

The experimental setup is mounted on top of a water tank measuring 0.8mx0.8mx2m made of 1.5cm thick glass walls (Figure 4.4). 2 meter dimension of the tank in the chord wise direction provides at least 15 chord length distance from wings to wall boundaries in both forward and backward directions. Also, 10 chord length distance kept between wing and wall boundary in span wise direction. Since the vibration isolation is important for the quality of the data, the tank is placed on a shock absorber material. Also, it has a metal cage in order to install the flapping mechanism.

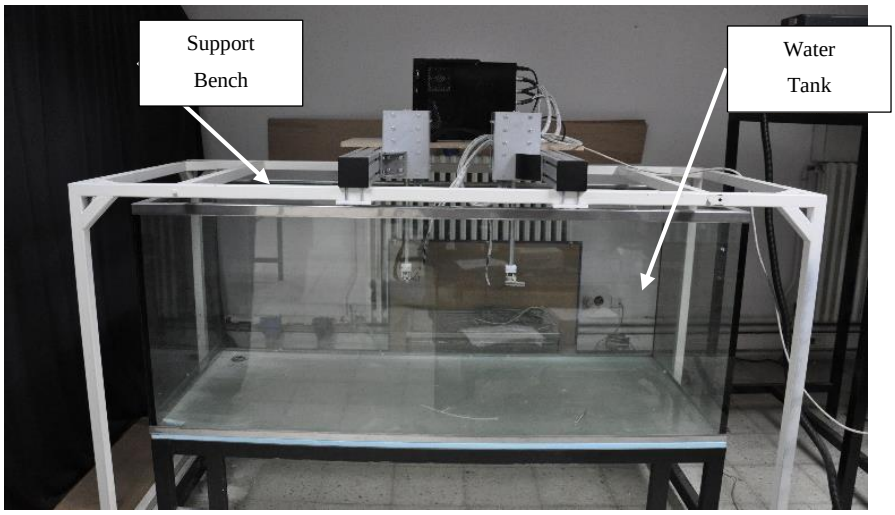

Figure 4.4 Water tank placement with flapping mechanism support bench and flapping wing mechanism

4.1.3 Definition of the Flow

The experiments are carried out in zero free-stream velocity. This means that flow needs to be rested before starting to each experiment in order to obtain a steadiness of the flow in the water tank. Kurtuluş [52] states that 15 minutes is sufficient for the experiments that are conducted in 1.5mx1mx1m water tank in order to guarantee steady surrounding around the wings. Minimum fifteen minutes of pauses should be given between each test case. Physical properties of flow medium are given in Table 4.1. The water tank is filled with purified water during the experiments in order to get rid of unwanted particles. Carbon filters are used for obtaining purified water from the tab water.

Table 4.1 Thermo-physical properties of the working fluid water.

Property	**Unit**	**Value**
Temperature (T)	[^{o}C]	20
Density (ρ)	[kg/m^3]	998.2
Dynamic Viscosity (μ)	[kg/m·s]	1.003×10^{-3}
Kinematic Viscosity (υ)	[m^2/s]	1.004×10^{-6}

4.1.4 Positioning System

The positioning system, namely Robot-Wings, is specially designed to mimic the insect wing motion and simulate the flight conditions of various insects in an experimental environment. It is placed on top of the water tank to give the intended motion to the wing models (Figure 4.6). A special software 'Wing-Sim' is developed for controlling of the wings and the logging of the position data in real-time. Robot-Wings uses PIC based custom made micro-controller boards for data acquisition. Micro controllers can be connected to host computer via USB or RS-232 cable. Two USB port are needed for each wing separately. Position feedback is provided by using the encoders connected to motors. The Wing-Sim uses position data for calculating the motor input signal in order to achieve the desired wing trajectory. Hardware connection of positioning system is shown in Figure 4.5. (Note that, only one wing module is illustrated in the Figure 4.5). A special support bench is used for supporting the positioning system and also separating it from the water tank (Figure 4.4). Thus, water tanks are isolated from any vibration that is originated form the wing modules by separating and flapping wings mechanism and the tank. The flapping mechanism needs 220 V AC separate power supply.

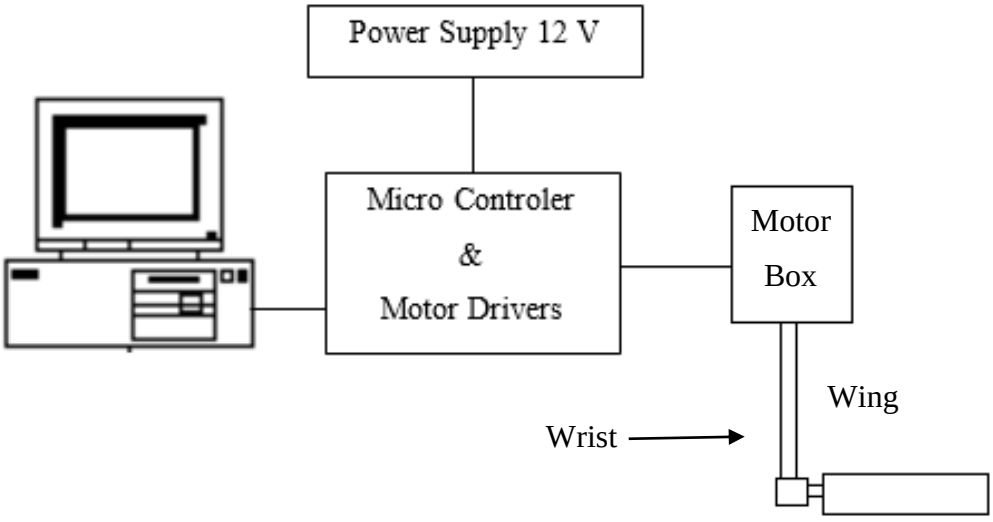

Figure 4.5 Hardware connection schematic of the positioning system (Note that only one wing module is shown in the figure)

4.1.5 Complete Setup

All systems that are used in the experiments are shown in the Figure 4.6. Two computer programs are needed during the experiments, one for measurements and the other for the motion. Measurement unit consist of 4 main part which are ATI NANO17, Net-box, NI-DAQ 6211 BUS, power supply and an in-house Labview block are prepared for ATI Force/Torque transducers. Figure 4.7 is shows the wing, transducer and mechanic arm assembly.

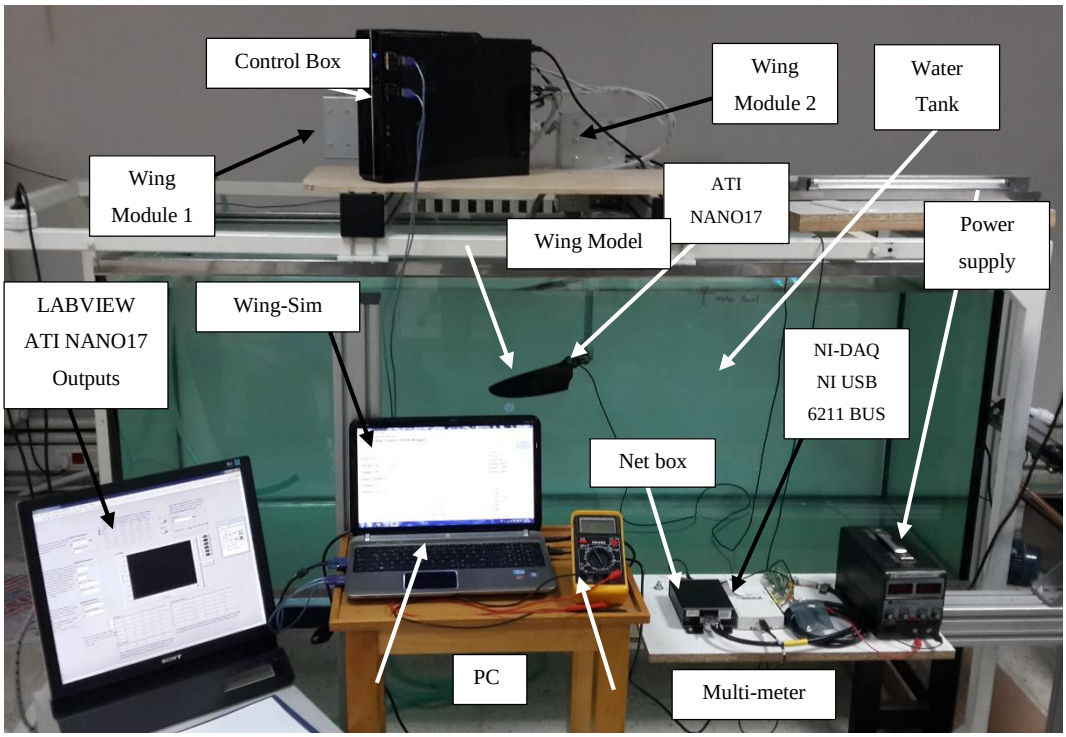

Figure 4.6 Complete experimental setup before the experiment

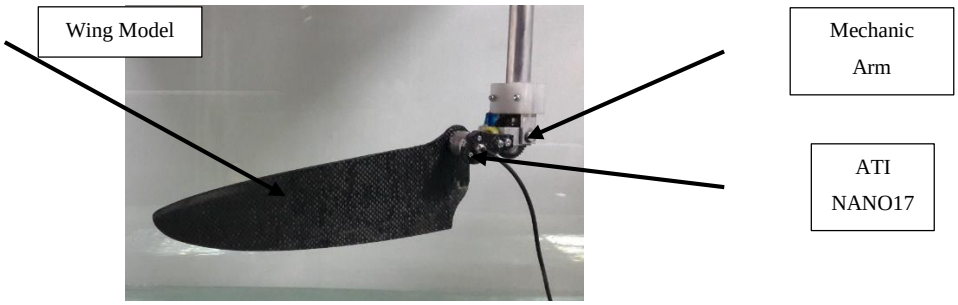

Figure 4.7 Wing model mechanism interference

4.2 Force and Moment Measurement

A special transducer, ATI NANO17, is used for force and moment measurements. The transducer is capable of measuring the force and moment in three axes. It is preferred to have water-proof and small dimensions. All measurements are carried out with a sampling frequency of 100 Hz. Measurements are recorded by using Labview software for data analysis. In order to obtain phase-averaged flow quantities, the measurements are performed for at least 50 flap cycles. The data is averaged per flap phase, to find the statistical mean. Uncertainty of this mean value is determined via calculating the standard deviation of the mean data. Following equation is used to calculate root-mean-square:

$$\sigma = \sqrt{\frac{1}{n-1}\sum_{i=1}^{n}(x_i - \bar{x})^2} \tag{4.1}$$

'n' is the number of the flapping cycles and x bar indicates the mean value of the aerodynamic force and moments over n data points. The standard deviation is a measure for the variety of the data

4.2.1 Force and Moment Transducer

ATI NANO17 is a 6-axis load cell capable of measuring force and moment. It has protection against water spray and submersion possibility up to 4m. ATI NANO17 is made of high strength stainless steel. Maximum allowable overload values are 3.1 to 6.9 times the rated capacities silicon strain gages provide a signal 75 times stronger than conventional foil gages. Thus, signal amplification results near-zero noise distortion. Table 4.2 gives the rated sensing ranges for ATI NANO17. It has cylindrical shape with 20 mm diameter and 22 mm height. Also, it weights roughly 40gr. Small dimensions and low weights provides better, less disturbed measurements. The transducer is connected to an amplifier, which amplifies the signal by approximately a factor of 1000. National Instruments (NI) 'NI-USB-6211 BUS' data acquisition

board is used during the experiments. Figure 4.8 shows the computer connection schematic of the sensor. Measurements are recorded by using Labview software. ATI NANO17 is attached to the wing mechanism and the wing model by using polyamide connection parts. Z-axis, which has the maximum load capacity, of the transducer is arranged to be perpendicular to platform of the wing models, since the aerodynamic forces usually act perpendicularly to chord direction.

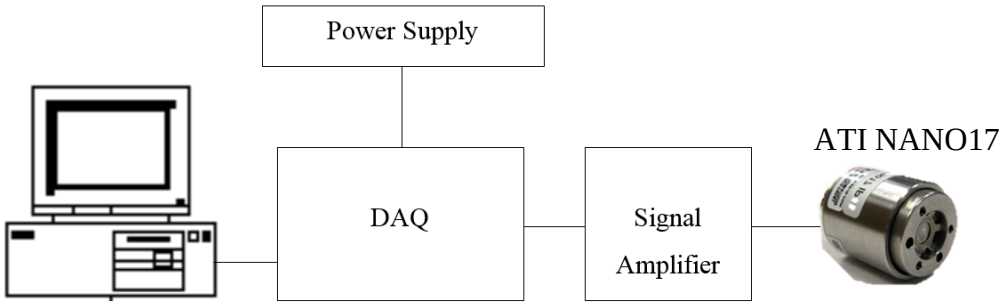

Figure 4.8 ATI NANO17 hardware schematic

ATI NANO17 is calibrated by using SI-12-0.12 calibration standard. Rated sensing range in x and y direction is ±12 N, and ±17 N for z axis. Table 4.2 gives its rated sensing range, signal resolution, counts value and tool transform factor for different calibration standards.

Table 4.2 ATI NANO17 standard calibration values

Calibration	SI-12-0.12	SI-25-0.25	SI-50-0.5
Rated Sensing Ranges			
Fx, Fy	±12.0 N	±25 N	±50 N
Fz	±17 N	±35 N	±70 N
Tx, Ty, Tz	±120 Nmm	±250 Nmm	±500 Nmm
Resolution (16-bit)			
Fx, Fy	1/1280 N	1/640 N	1/320 N
Fz	1/1280 N	1/640 N	1/320 N
Tx, Ty, Tz	1/256 Nmm	1/128 Nmm	1/64 Nmm
Counts Value (16-bit)			
Fx, Fy, Fz	1280 / N	640 / N	320 / N
Tx, Ty, Tz	256 / Nmm	128 / Nmm	64 / Nmm
Tool Transform Factor	0.05 mm/unit	0.05 mm/unit	0.05 mm/unit

4.2.2 Labview Measurement Block

A Labview program block is used for reading data from ATI F/T Transducers and NI DAQ Board during the experiments (Figure 4.9). Sensor parameters, calibration file, should be introduced to the program (Block A), also connection protocol between host computer and the NI DAQ Board should be established (Block B). Sampling rate can also be arranged (Block C). Real-time force and voltage readings are shown during the measurement (Block D-E). Block f plots the all 6 measurement simultaneously. Calibration matrix of the ATI NANO17 is given in the Block G. If it is existed, bias of the readings can be eliminated by using the Block H. Also, reversing this procedure is possible. Finally, Block I is used for specifying the data output file. It has a control switch to start data logging. Measurements are started to logging the data before the wings starting the flapping. Synchronizing can be done by finding the first rise in the force measurements. Since the sensor is undoubtedly precise and sensible, it is safe to use it for matching the data.

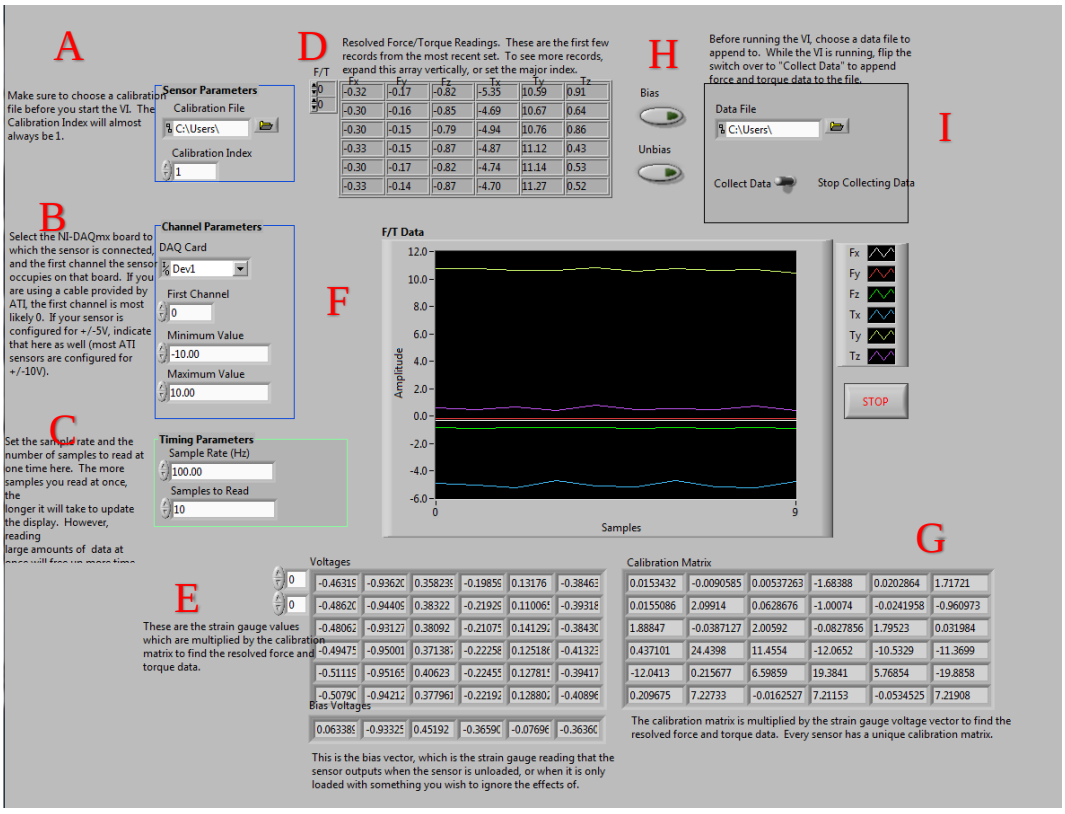

Figure 4.9 Labview Force/Torque measurement block.

4.2.3 Coordinate Transformation

The mechanism is capable of measuring the flapping angles via encoders that are attached to the motors. Actually encoders measures the PWM value of the motors. After that this PWM values are transformed to the wing angular position in real-time and logged. Since the transducer is connected to the wings, the measured quantities are obtained on the wing and expressed in the wing-fixed coordinate frame. It is desired to obtain the force and moment measurements for a stationary earth-fixed inertial frame, for which the vertical axis is the z-axis, the forward direction is the y-axis (Figure 4.10).

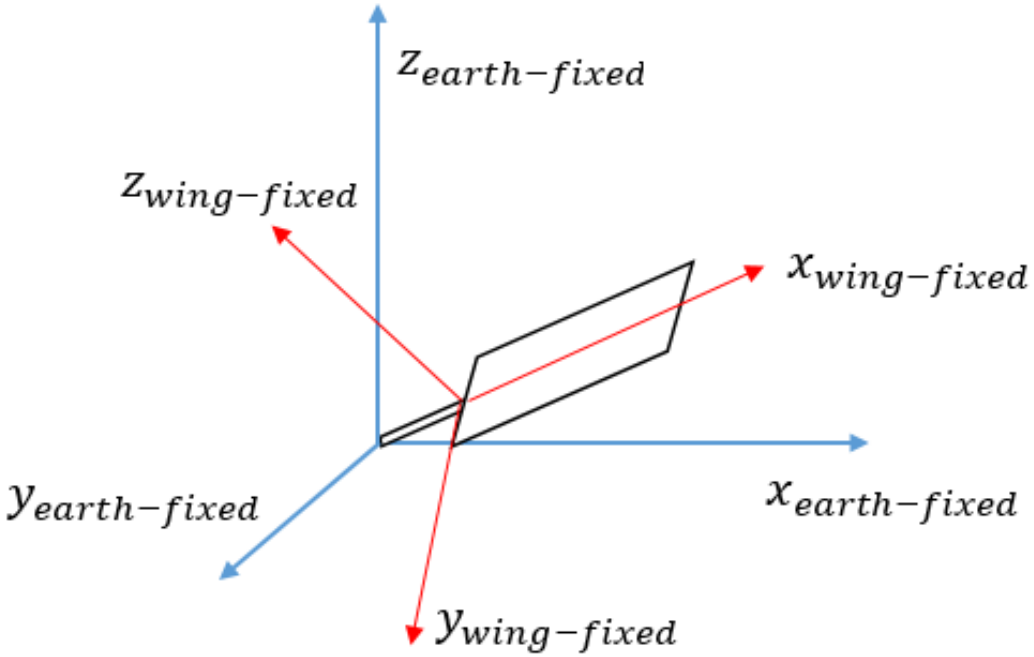

Figure 4.10 Earth-fixed and wing-fixed coordinates systems

Therefore, quantities that are measured in wing-fixed coordinate system needs to be transformed in to earth-fixed coordinates. This is accomplished by a 3-2-1 Euler angle transformation. In order to obtain the resulting rotation matrix, first rotation, θ_1, is given about the vertical axis of earth-fixed frame, the second rotation, θ_2, is around

the x axis of the wing-fixed frame, and the last rotation, θ_3 is about the y-axis of wing-fixed frame. Rotation matrix is given as follows;

$$R(\theta_3,\theta_2,\theta_1)=\begin{bmatrix}1 & 0 & 0\\ 0 & c\theta_3 & -s\theta_3\\ 0 & s\theta_3 & c\theta_3\end{bmatrix}\begin{bmatrix}c\theta_2 & 0 & s\theta_2\\ 0 & 1 & 0\\ -s\theta_2 & 0 & c\theta_2\end{bmatrix}\begin{bmatrix}c\theta_1 & s\theta_1 & 0\\ -s\theta_1 & c\theta_1 & 0\\ 0 & 0 & 1\end{bmatrix} \quad (4.2)$$

A general rotational matrix has the following form,

$$R(\theta_3,\theta_2,\theta_1)=\begin{bmatrix}c\theta_2c\theta_1 & c\theta_2s\theta_1 & -s\theta_2\\ s\theta_3s\theta_2c\theta_1-c\theta_3s\theta_1 & s\theta_1s\theta_2s\theta_3+c\theta_1c\theta_3 & c\theta_3c\theta_2\\ c\theta_3s\theta_2c\theta_1+s\theta_1s\theta_3 & c\theta_3s\theta_2s\theta_1-s\theta_3c\theta_1 & c\theta_3c\theta_2\end{bmatrix} \quad (4.3)$$

Rotation matrix converts is to convert earth fixed to wing fixed coordinate system. Therefore, the force that is expressed in the earth-fixed frame can be found by using the following transformation;

$$F_{earth}=R(\theta_3,\theta_2,\theta_1)^TF_{wing} \quad (4.4)$$

Invers of the rotational matrix given as follows;

$$R(\theta_3,\theta_2,\theta_1)^T=\begin{bmatrix}c\theta_2c\theta_3 & s\theta_1s\theta_2c\theta_3-c\theta_1s\theta_3 & c\theta_1s\theta_2c\theta_3+s\theta_1s\theta_3\\ c\theta_2s\theta_3 & s\theta_1s\theta_2s\theta_3+c\theta_1c\theta_3 & c\theta_1s\theta_2s\theta_3-s\theta_1c\theta_3\\ -s\theta_2 & s\theta_1c\theta_2 & c\theta_1c\theta_2\end{bmatrix} \quad (4.5)$$

4.3 Motion Kinematics

This part explains the wing trajectories with graphical and mathematical expressions. Also, motion figures are used in order to obtain better illustration of the wing motion for each case. Basically, three types of trajectory are used in the experiments. First one is the step function trajectories, which are used for P-constant calibration test. Second motion type is the pure pitch and plunge motion, which are considered in order to

investigate the effect of the impulsive motion, and to distinguish circularly and non-circularly ingredient of the aerodynamic forces. Finally, the last motion, which is used for simulating the hovering wing trajectory in a planar stroke plane, is the combined pitch and plunge motion case. Wing placement during the experiment is illustrated in Figure 4.11. Wing is placed to the water tank providing that the x axis of the wing-fixed coordinate system stays horizontal during the experiment.

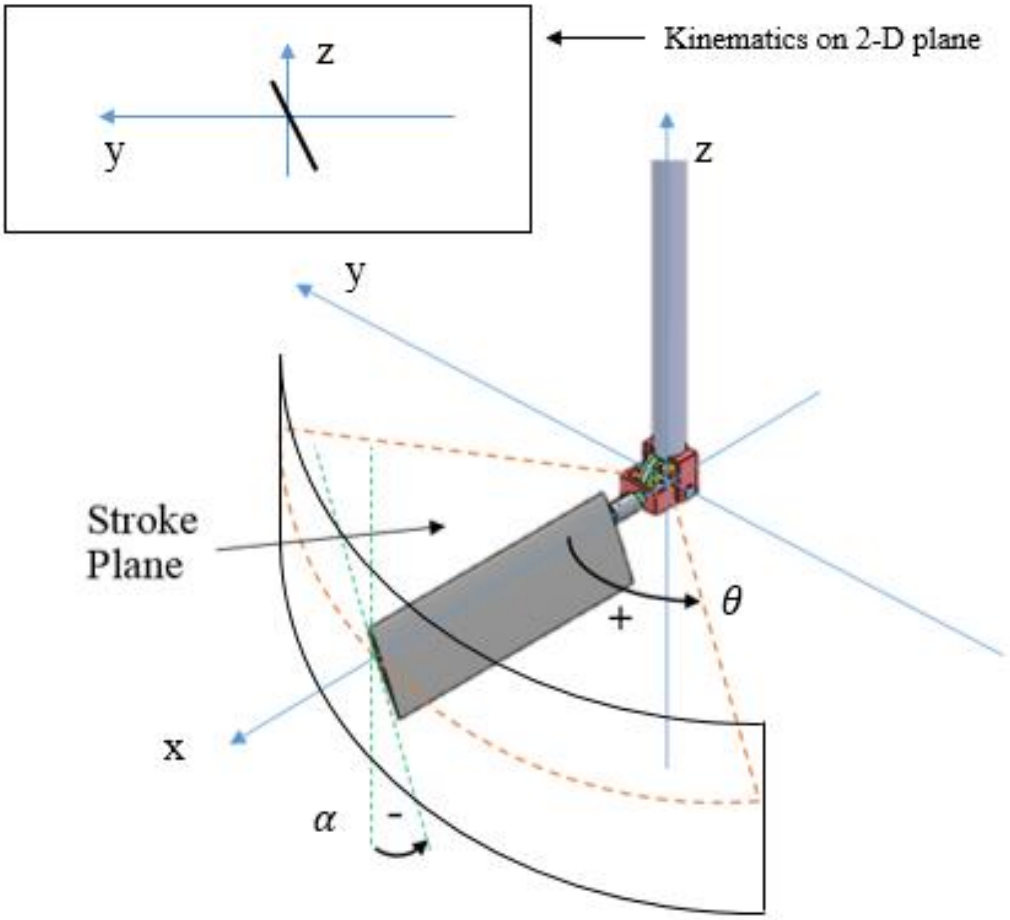

Figure 4.11 Wing trajectory sign convention and stroke plane illustration

4.3.1 Step Function Motion Trajectory

P-constant calibration is performed for pitch and plunge axis of the mechanism. Each axis is given a pure motion which is defined by step function. A Step function, having an amplitude of 20º, is given to the mechanism for pitch axis P-constant calibration

test. Plunge axis calibration is performed for plunge amplitude of 40º with a zero pitch. Eq.4.6 gives the mathematical expression for the wing motion that is used in pitch axis P-constant calibration. Also, Figure 4.12 shows the motion graphically.

$$Pitch:\ \zeta_{w,step}(A,T,\varphi,t) = \begin{matrix} +20°, & t(modT) < T/2 \\ -20°, & t(modT) > T/2 \end{matrix} \tag{4.6}$$

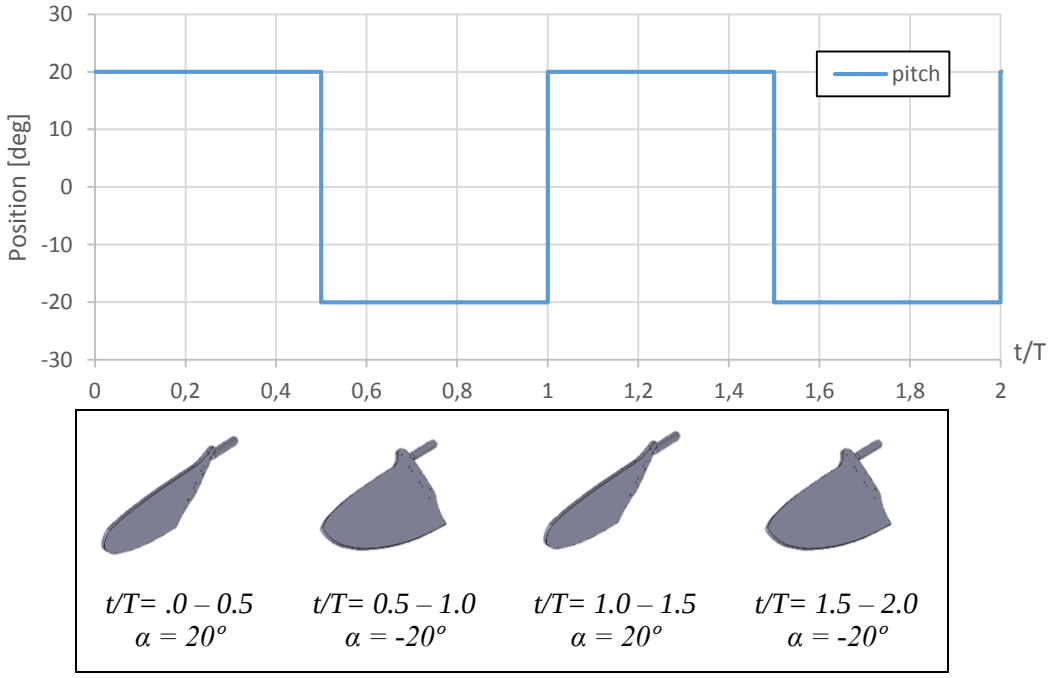

Figure 4.12 Pitch axis desired motion trajectory for P-constant calibration

Eq.4.7 gives the mathematical expression for the wing motion that is used in pitch axis P-constant calibration.

$$Yaw:\ \zeta_{w,step}(A,T,\varphi,t) = \begin{matrix} +20°, & t(modT) < T/2 \\ -20°, & t(modT) > T/2 \end{matrix} \tag{4.7}$$

Figure 4.13 shows the motion graphically. Also, illustration of the wing positions is given for different time internals.

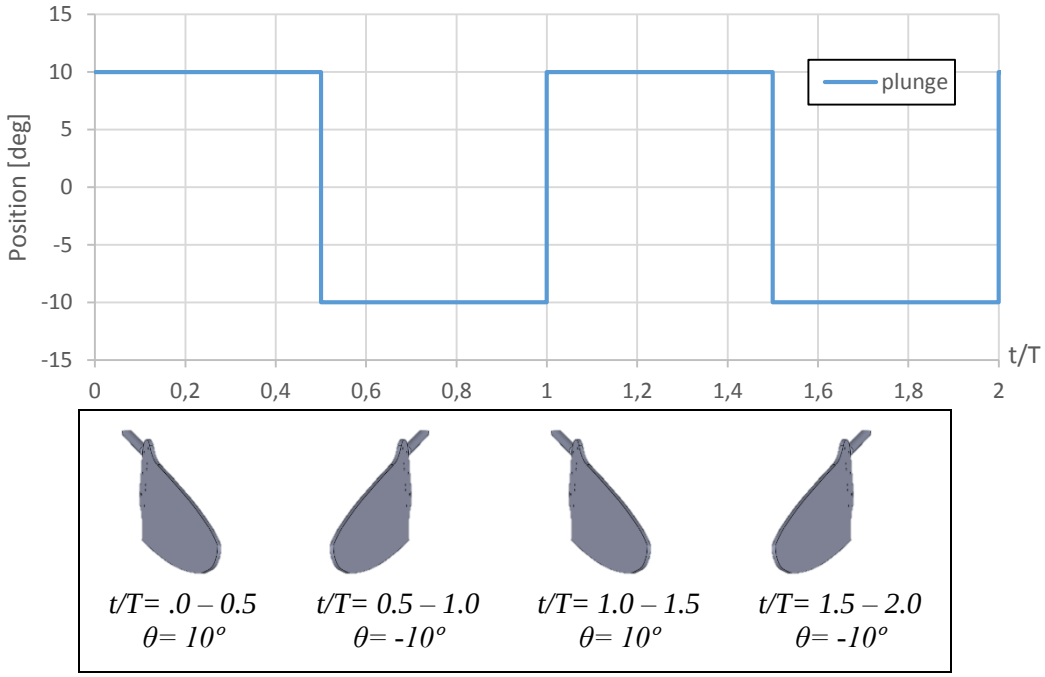

Figure 4.13 Plunge axis desired motion trajectory for P-constant calibration

4.3.2 Pure Pitch and Plunge Sinusoidal Motion Trajectory

Pure pitch motion is performed in order to understand the effect of the wing rotation at the end strokes (Figure 4.14). By doing so, positive attack angle is always preserved during the motion and additional lift generated due to wing rotation. Eq.4.8 gives the mathematical expression for pitch motion.

$$Pitch: \quad \zeta_{w,sine}(A,T,\varphi,t) = A * \sin(2\pi t/T + \varphi) \tag{4.8}$$

$$where, \qquad A = 30°, 45°, 57° \; and \; T = 7.14, \qquad \varphi = 0$$

Pure plunge motion is performed in order to understand the effect of the wing angular transition during the stroke (Figure 4.15). Eq.4.9 gives the mathematical expression for pitch motion.

$$Plunge: \zeta_{w,sine}(A,T,\varphi,t) = A * \sin(2\pi t/T + \varphi) \tag{4.9}$$

$$where, \qquad A = 57° \; and \; T = 7.14, \qquad \varphi = 0$$

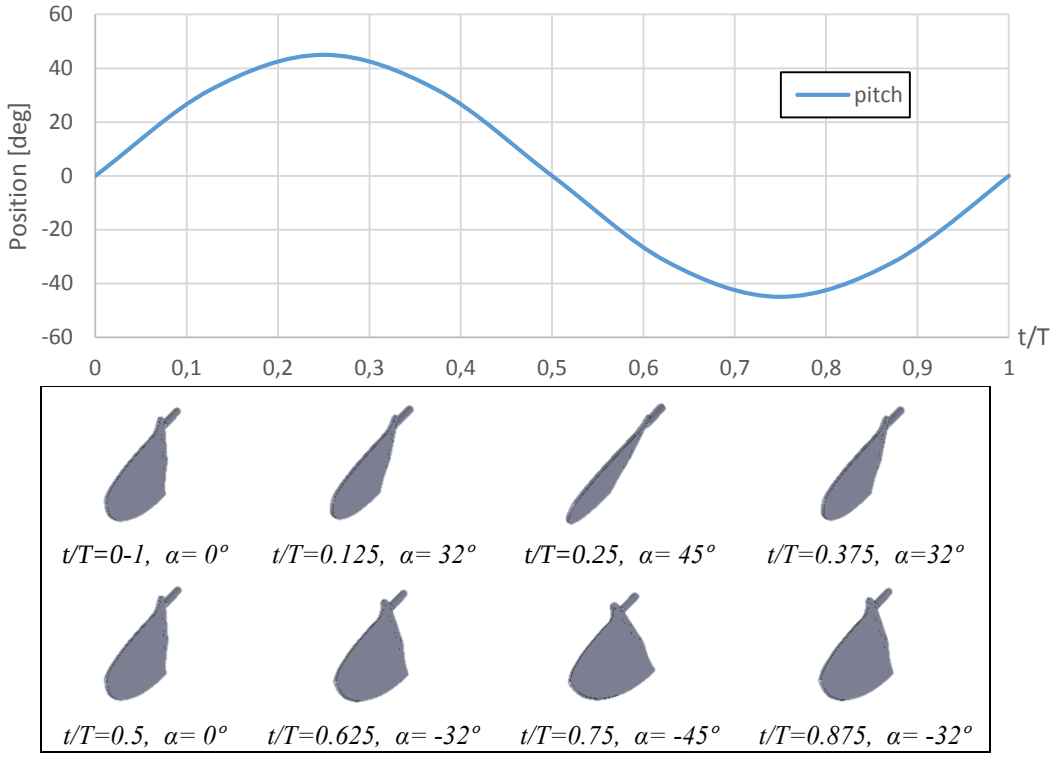

Figure 4.14 Sinusoidal pure pitch motion (A=45º, f=0.14)

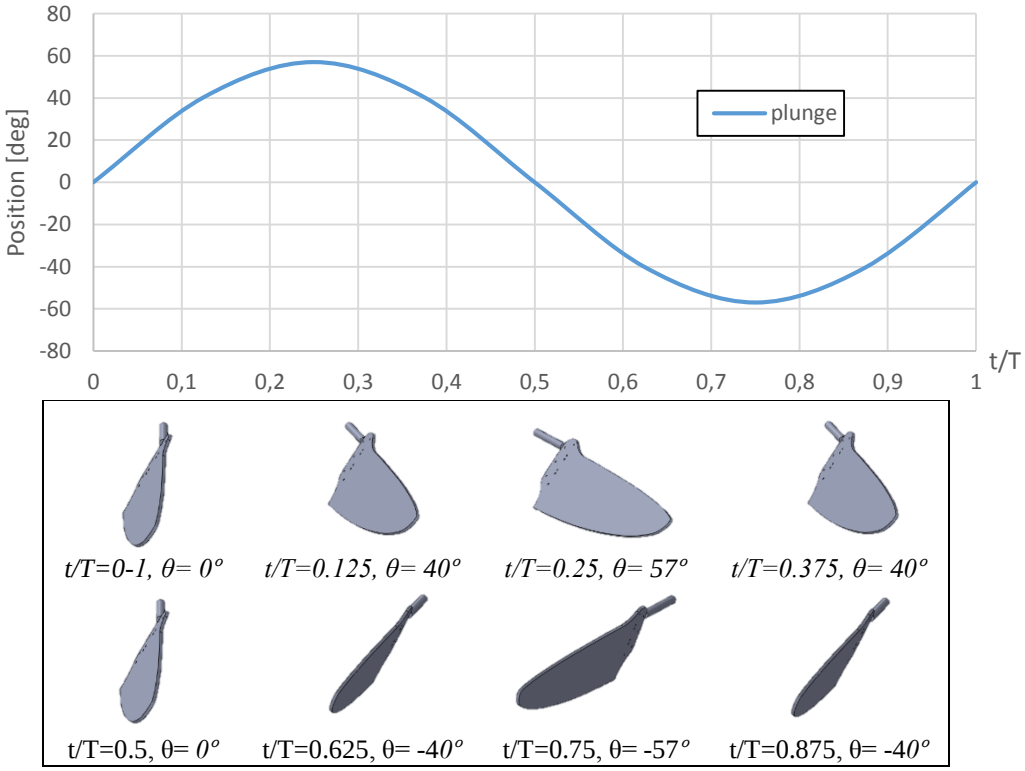

Figure 4.15 Sinusoidal pure Plunge motion with 45º constant attack angle (A=57º, f=0.14)

4.3.3 Combined Pitch and Plunge Sinusoidal Motion Trajectory

Combined pitch and plunge motion is used for mimicking the hovering insect flight. 90 degrees phase angle between pitch and plunge motion is introduced to achieve the desired trajectory. Eq. 4.10 gives the mathematical expression for pitch motion. Combined pitch and plunge motion can be seen in Figure 4.16.

$$Pitch: \quad \zeta_{w,sine}(A,T,\varphi,t) = A_1 * \sin\left(\frac{2\pi t}{T} + \varphi_1\right)$$

$$Plunge: \quad \zeta_{w,sine}(A,T,\varphi,t) = A_2 * \sin(2\pi t/T + \varphi_2) \qquad (4.10)$$

$$Where, \quad A_1 = 30°, 45°, 57°, \qquad A_2 = 57° \; and \; T = 7.14, \; \varphi_1 = \pi, \varphi_1 = \pi/2$$

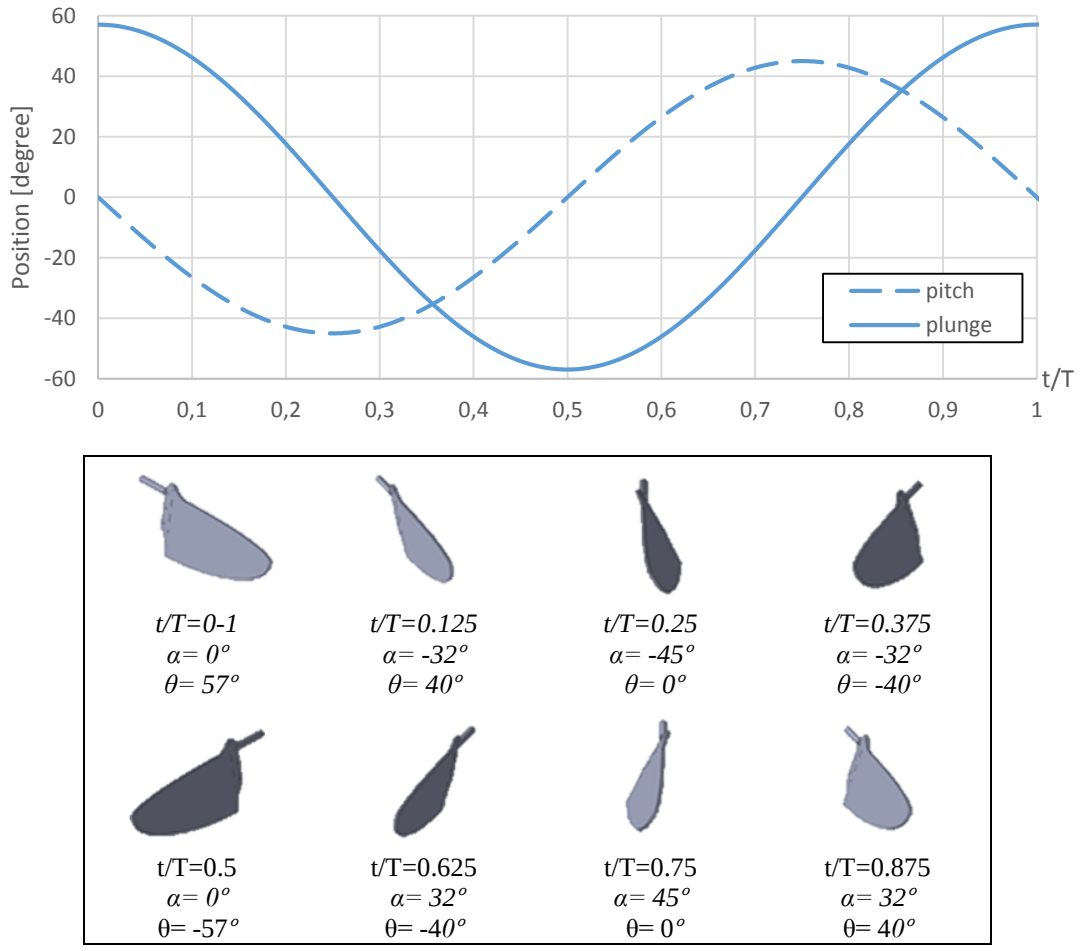

Figure 4.16 Sinusoidal combined pitch and plunge motion (A_{pitch}=45º, A_{plunge}= 50º f=0.14)

4.4 Validation Case

Morrison et. al [46] performed force measurement for Bio-inspired flapping motion of two angular degrees of freedom. The experiments are conducted at Reynolds number of 7100 and a reduced frequency of 0.21, which are properly scaled for a water tank. Results that are presented by Morrison et. al [46] are used as a validation data for the new experimental setup Time resolved phase-averaged force measurements are performed and development of two single peak during the sinusoidal flapping cycle are observed by Morrison et. al. [46] approximately 100 cycles from a single continuous motion excluding first fifteen and last partial cycle are used in order to obtain phase-averaged data. Furthermore, power requirements of the flapping wing are given in the study. The wing plunges through 114.6º of amplitude with 57.3º angle of attack at the mid stroke and change direction at end strokes as it shown in Figure 4.17. Schematic of the motion kinematic and experimental setup are given more detailed in following figure.

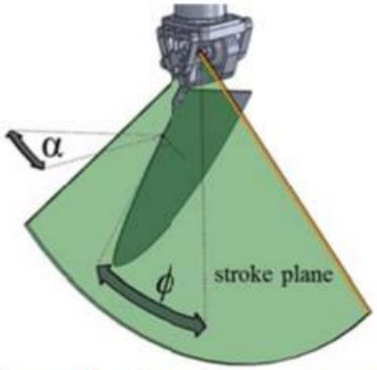

Figure 1. Coordinate system

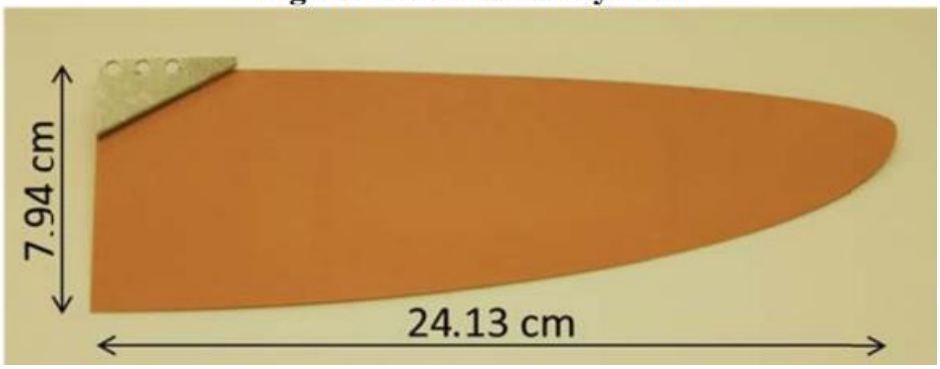

Figure 4.17 Experiment schematic of validation case and the wing that is used (from Ref. [46])

4.5 Summary of the Experimental Conditions

There are two major experiment campaign that are performing pure and combined pitch and plunge motions. Impulsive motion of the flapping wing is considered in campaign I. Pitch axis is given a constant speed pitching motion and plunge axis is tested for 58° angle of attack. Campaign 2 is considered combined pitch and plunge motion of the wing in a planar stroke plane. Case 3 is identical with the validation case, which is aiming to validate the new setup by means of comparing the results of Morrison et. al [46] with the current experimental data. Then, Case 1, Case 2 and Case 3 are repeated with the same motion of validation case with different pitching angles. Summary of the experimental conditions are tabulated in Table 4.3.

Table 4.3 Summary of the experimental conditions

Campaign	**I (Impulsive)**				**II (Sinusoidal)**		
Motion Type	**Pure pitch**		**Pure Plunge**		**Combined Pitch & plunge**		
Test Case	**1**	**2**	**1**	**2**	**1**	**2**	**3**
Pitch	**33 °/s**	**65 °/s**	**30°**	**45°**	**30°**	**45°**	**57°**
Plunge	**0°**		**58 °/s**		**57°**	**57°**	**57°**
Wing Models	Zimmerman Wing						
Wing Chord [m]	0.08						
Wing Span [m]	0.24						
Reynolds Number	$7x10^3$		$2x10^4$		7100		
Reduced Frequency	-		-		0.21		
Flapping frequency	-		-		0.14	0.14	0.14
Ref. Velocity [cm/s]	8		24		12.2	12.2	12.2

4.6 Calibration Procedure

Robot-Wings requires special calibrations for different experimental environments and wing models. Wing motion calibration can be done by means of two main

parameters. These parameters are being P – Constant and minimum PWM value. Each axes are given the motion defined by a step function for P- Constant calibration. Data collection during the P – Constant calibration is done 50 times for each axes in order to obtain phase average position data. Higher P - Constants cause overshooting position values on the other hand lower coefficients cannot catch up with the step function (Figure 4.18).

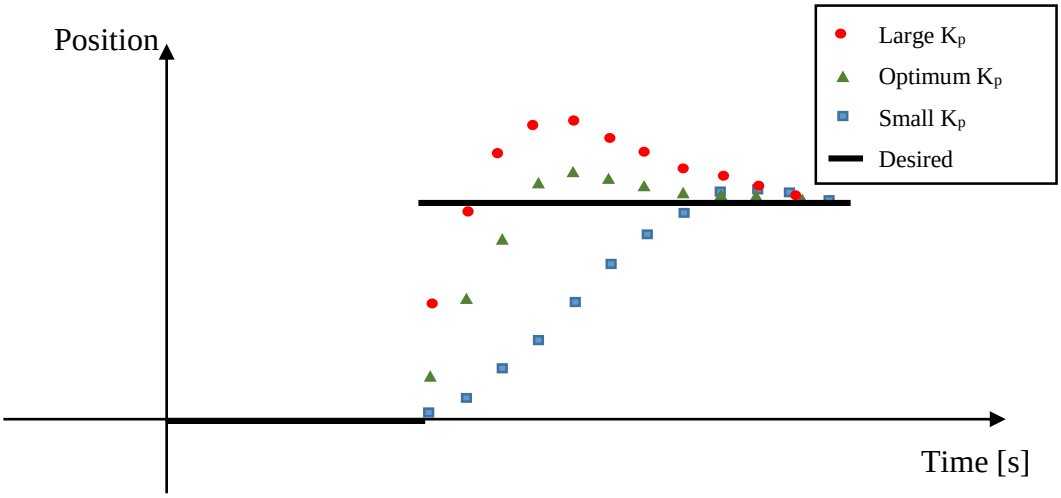

Figure 4.18 Step function motion response illustrations for different Kp

For example, a step function motion, which has 30° of amplitude with 5 sec period, is used in order to determine the P – Constant characteristics of each axes. NACA 0006 wing models, which have 6 cm chord and 18 cm wing span, is used during the calibration test. Experimental data for plunge axis is given in Figure 4.19 as an example.

Different proportional coefficients are tested for calibration. At the end 4.2 proportional constant is chosen as plunge axis P – Constant. During the plunge axis calibration test, only plunge axis is activated and the other two axes are expected to be constant

However, pitch and plunge axis have position uncertainties. Pitch axis has larger uncertainty compared to plunge axis. Mean value and standard deviation of pitch axis position data are respectively 0.40 and 1.73 whereas plunge axis data are 0.13 and

0.10. Note that, Position uncertainties have negligible values for sinusoidal and ramp functions compared to step function motion trajectories. Calibration tests are performed for each axes and P – Constant of 4 obtain for pitch and plunge axes.

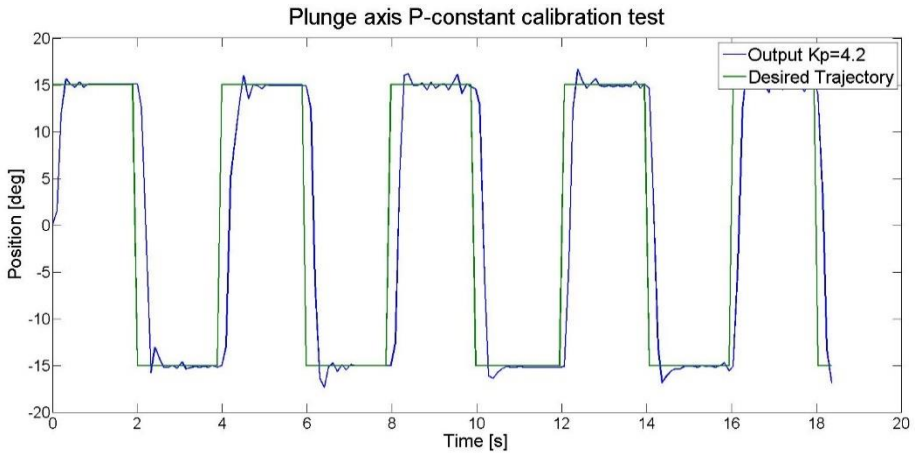

Figure 4.19 Plunge axis P-Constant calibration test data

Minimum PWM value calibration is done by using sinusoidal motion trajectory. Without any specified minimum PWM information, experimental position data cannot follow the sinusoidal trajectory especially around the peaks. A sinusoidal motion, which has 30° of amplitude and 5 sec period, is used in calibration tests. Minimum PWM value is determined as 20. Since this quantity is related to threshold value of the motor, testing for different wings is not necessary. In other words, this quantity is directly related with the electric motor not with the wings.

4.7 Experimental Procedure

Experimental procedure can be divided in to three part, namely the preparation, run, and data process. To begin with, water level in the tank should be measured before the experiment. The flapping axis is placed 20 cm beneath the water surface in the validation case accordingly the other cases use the same depth. Since the ATI NANO17 transducer is a delicate and expensive sensor, power supply voltage should be measured before connecting. The force and torque data are recorded with NI 6611

data acquisition board which can be connected to computer from USB port. All cable connections should be checked before powering up the instruments. A Labview program is used for reading and logging the output of the sensor. Sampling time of the flapping mechanism and the ATI NANO17 should be synchronized. Also, flapping wing calibration is done for each wing separately. Secondly the run phase is performed. After setting the wing initial position, bias of the sensor reading doe to gravitation should set to zero. Flapping cycles should be repeated 50 times in order to obtain phase averaged data. In addition, 15 minutes of pauses are given between all experiments in order to ensure that the water does not move. Furthermore, wing position is monitored during the experiments to avoid any positional drift due to backlash. Finally, after the experiments all data is saved. Finally, force and moment time history of the flapping motion are plotted.

CHAPTER 5

RESULTS AND DISCUSSION

This chapter is devoted to the discussion and comparison of all the results that are obtained from the experimental simulation of the baseline test cases. At first, calibration data for flapping mechanism is determined. In order to calibrate the flapping wing mechanism, different proportional constants and sensitivity coefficients are tested. In addition, heaving axis of the mechanism is fixed mechanically in order to prevent any position error due to backlash, since only pitch and plunge axis are used in the experiments. P- Constant of the heaving motor is set to zero for all experimental case because any unintentional activation of the heave axis could harm the mechanism. After that. Experimental setup is ready for testing of 3 baseline case. At first, impulsive cases with the Zimmerman wing are completed. After that, combined pitch and plunge motion is tested in Campaign 2. As a result, time history of aerodynamic forces during one complete flapping cycle are plotted. Results of Case 3 is compared with the Morrison's results [46]. All results, which are presented in this section, are filtered by using Butterworth filter with a 2.5 Hz cut-off frequency. Detailed information about the test cases will be given in relevant parts. To sum up, Chapter 5 is divided in 5 main sub section. First section, is about the calibration process. Following 3 part considers the pitching and plunging motion of the different wings and presents the aerodynamic forces and moments as results. In the last section, each case that is considered in this study are compared with each other.

5.1 Results of P-Constant Calibration Test

Calibration tests are performed for the pitch and plunge axes of the wing module 2 only. Since the validation case investigates the pitch plunge motion of a single wing. Note that, wing model is placed vertically in the Morrison's original experiment [46]. However, in the current experiment setup, horizontal placement of the wing is preferred since the water tank has longer dimensions in horizontal direction.

5.1.1 Pitch Axis Calibration

Six P-constant values from 1 to 6 implemented for pitch and plunge rotation axis control. Motions are repeated for 50 cycles and phase average data for one cycle is obtained for each wing. Same initial position, is used such as wing chord is aligned with vertical and wing span is aligned with horizontal. A wing trajectory of pure pitch motion, having 40º peak to peak amplitude and 4 s time period, is performed during the pitch axis P-Constant calibration test. Phase averaged position data for one flapping cycle of the pitch axis motion are plotted in Figure 5.1

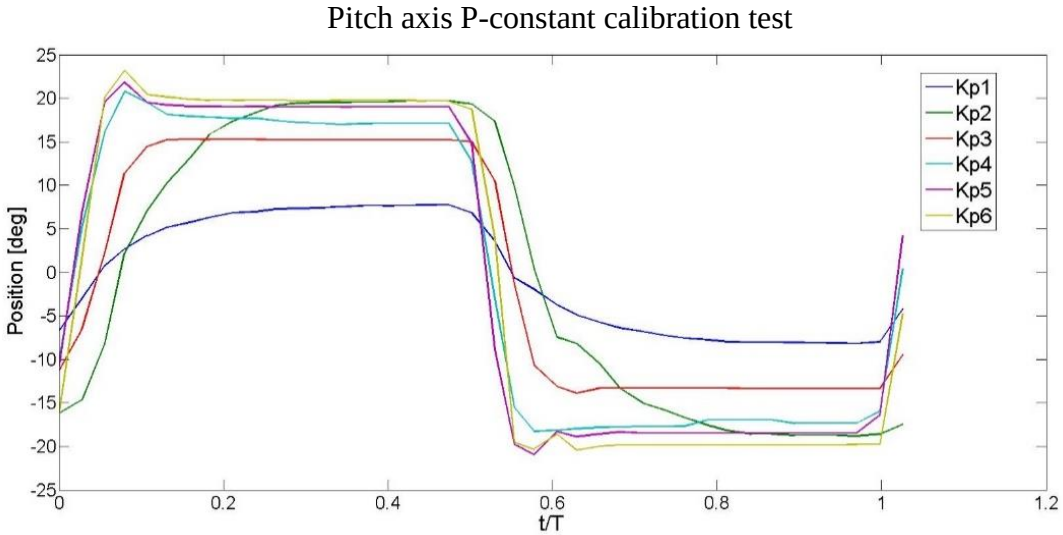

Figure 5.1 Time history of the pitch angle obtained from Wing Module 2 for a pure pitch motion ($A = 20°$, f=0.25 Hz, $\varphi = 0$, D=0) Zimmerman wing

P-Constants that are smaller than 5, resulted in undershoot in positions data whereas P-Constant value of 6 is causing overshoots. P-constant of 5 is the best choice for the pitch control.

5.1.2 Plunge Axis Calibration

Plunge angle position of the wing during pitch calibration has not any effect on the pitch axis motion. However, pitch angle position has a strong influence on the necessary plunge moment since the aerodynamic forces that are generating the plunge moment are dependent to pitch angle position of the wing. In order to ensure the maximum plunge moment generation, wing is placed with zero angle pitch position initially. Hence, the plunge moment is maximized. A wing trajectory of pure pitch motion, having 20º peak to peak amplitude and 4 s time period, is performed during the plunge axis P-Constant calibration test. Phase averaged position data for one flapping cycle of the pitch axis motion is plotted in Figure 5.2. P-Constants that are smaller than 4 resulted in undershoot in positions data whereas P-Constant values that are greater than 4 is caused overshoots. P-constant of 4 is the better choice for the plunge control. More detailed data about the calibration procedure are given in Appendix A.1.

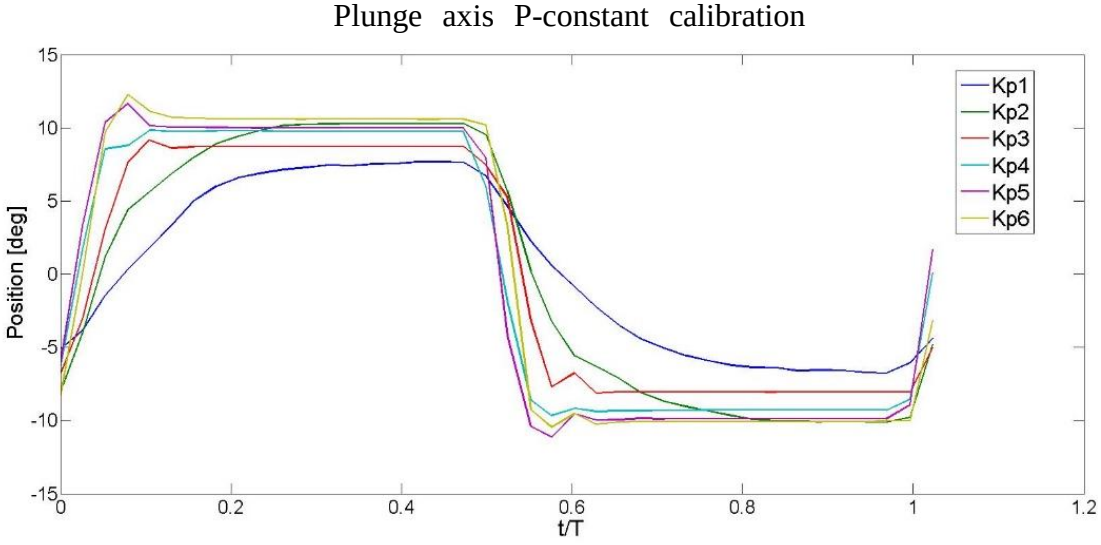

Figure 5.2 Time history of the plunge angle obtained from Wing Module 2 for a pure plunge motion ($A = 10°$, f=0.25 Hz, $\varphi = 0$, D=0) Zimmerman wing

5.1.3 Position Error History

Position error distribution is calculated by taking the phase average of raw data of 50 periods. It can be concluded that for low P-constants order of magnitude of the position error for pitch motion is twice of the plunge motion. The reason for this can be explain by the motion transmission factor. Plunge axis only uses timing belt for motion transmission whereas pitch axis uses three bevel gear addition to timing belt. That's why, position uncertainty of the pitch axis is higher than the plunge axis.

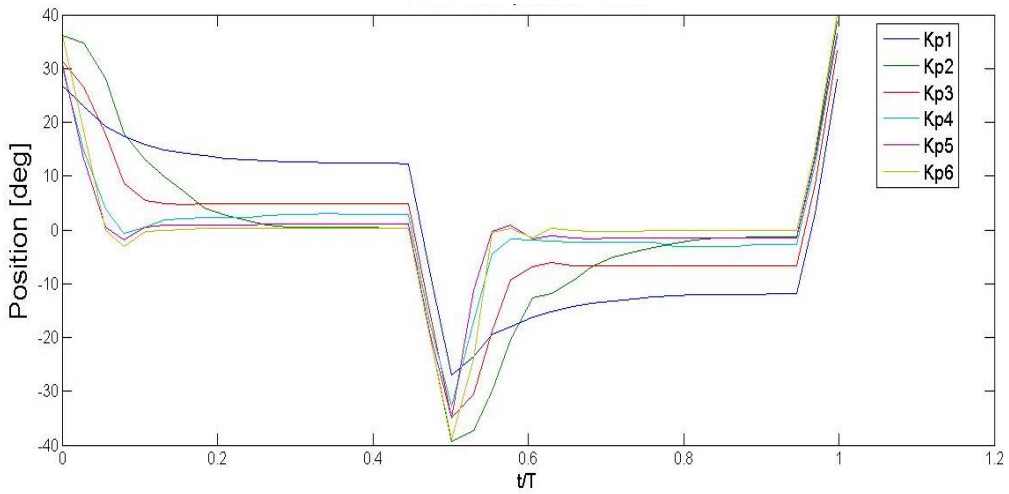

Figure 5.3 Time history of the pitch angle position error obtained from Wing Module 2 with a pure pitch motion ($A = 20°$, f=0.25 Hz) Zimmerman wing

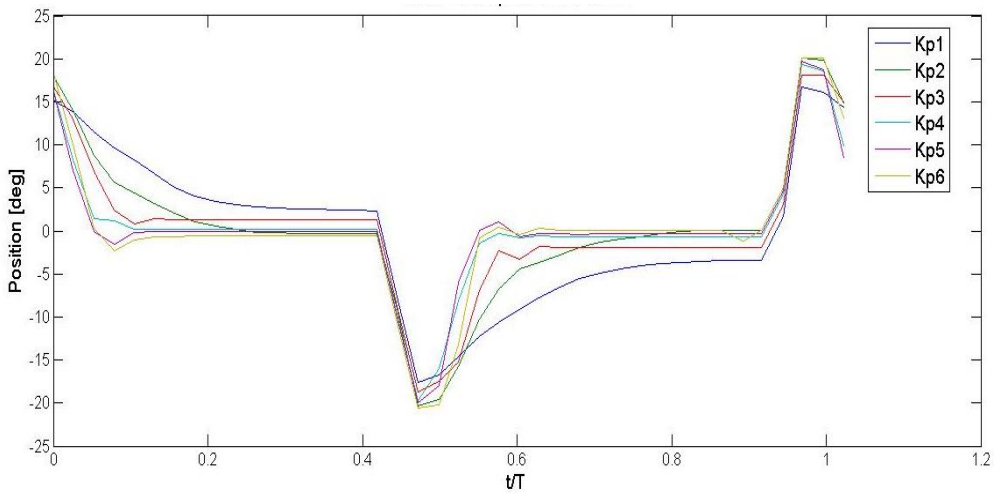

Figure 5.4 Time history of the plunge angle position error obtained from Wing Module 2 with a pure plunge motion ($A = 10°$, f=0.25 Hz) Zimmerman wing

5.2 Results of Pure Pitch Impulsive Motion

Impulsive pure pitch motion is tested with a constant velocities of 33 º/s and 65 º/s. This velocities are determined accordingly to initial velocities of the 30º and 57º sinusoidal pitching motions. Motion is limited in order to protect the sensor cable. Furthermore, in order to prevent impulsive termination of the motion, it is adjusted such that the pitch position approaches to the final value with a decaying gradient.

5.2.1 Case 1

Case 1 investigates the 33 º/s constant angular velocity pitch motion. Wing reaches 150º in 7 seconds. Figure 5.5 presents the time history of the motion graphically and Figure 5.6 shows the wing angular position at various instants.

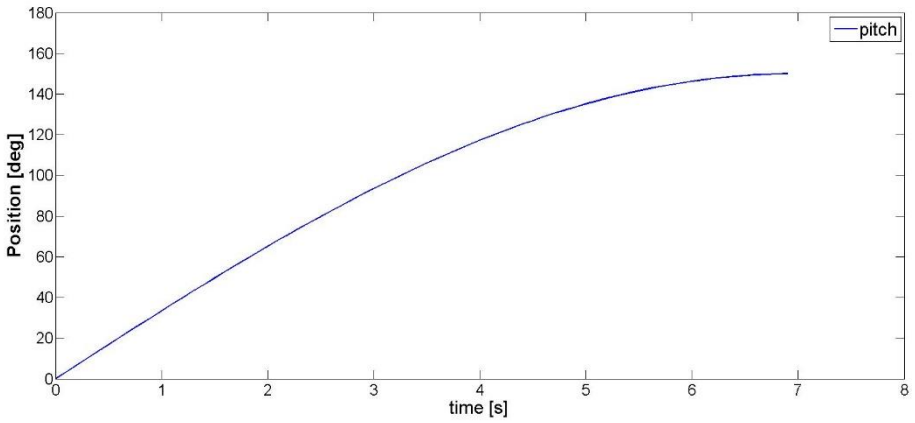

Figure 5.5 Time history of pitch angle for a pure pitch motion of 33 º/s

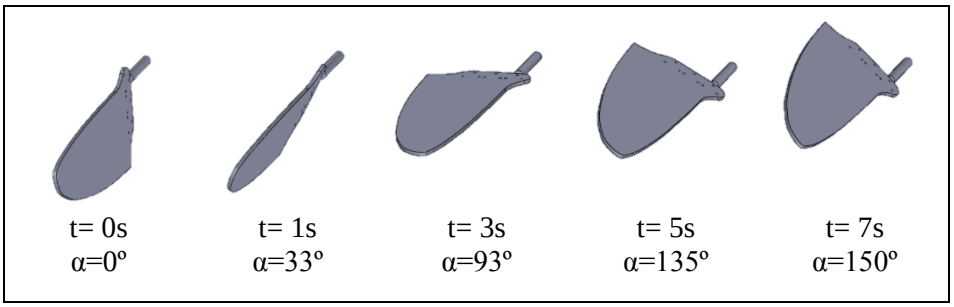

Figure 5.6 Wing position at different instants for a pure pitch motion of 33 º/s

Normal force time history for impulsive pitch case is shown in the Figure 5.9. Normal force increases with the impulsive start and after a while it reaches to a peak value and finally converges to a constant value. Since the impulsive pitching motion is performed with zero angular acceleration. It is expected to have a steady aerodynamic force measurement eventually. Frequency analysis of the force signal shows the uncertainties of the system due to mechanical imperfections. Figure 5.8 gives the frequency decomposition of the force signal.

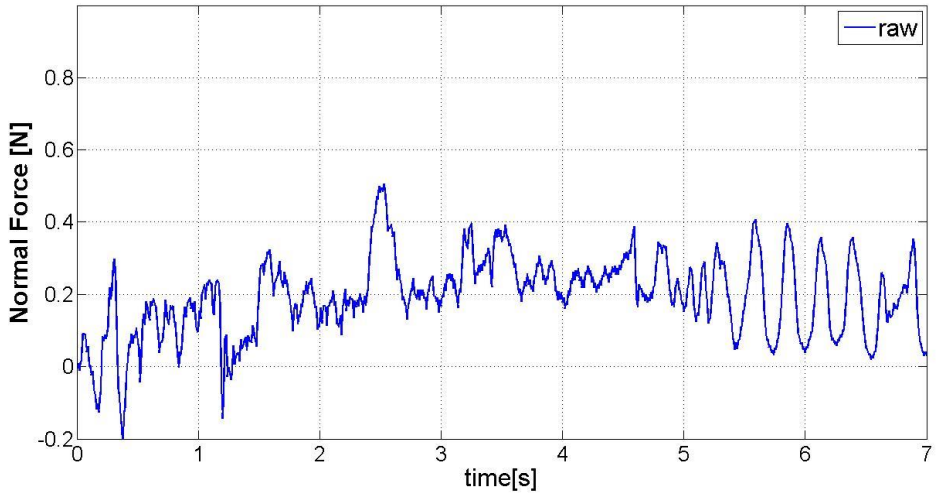

Figure 5.7 Time history of normal force component (raw data) for a pure pitch motion of 33 °/s

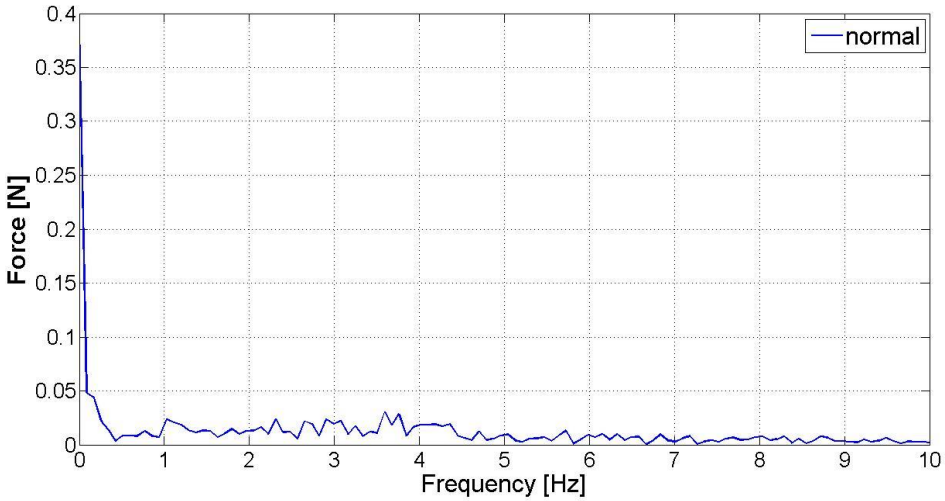

Figure 5.8 Normal force harmonic content for a pure pitch motion of 33 °/s

Fluctuations in the measurements are mainly generated by frequencies higher than 1 Hz. Note that, during the impulsive start normal force increases mainly because of Wagner effect. Force measurements is filtered by using a Butterworth filter with a cut-off frequency of 1 Hz (Figure 5.9).

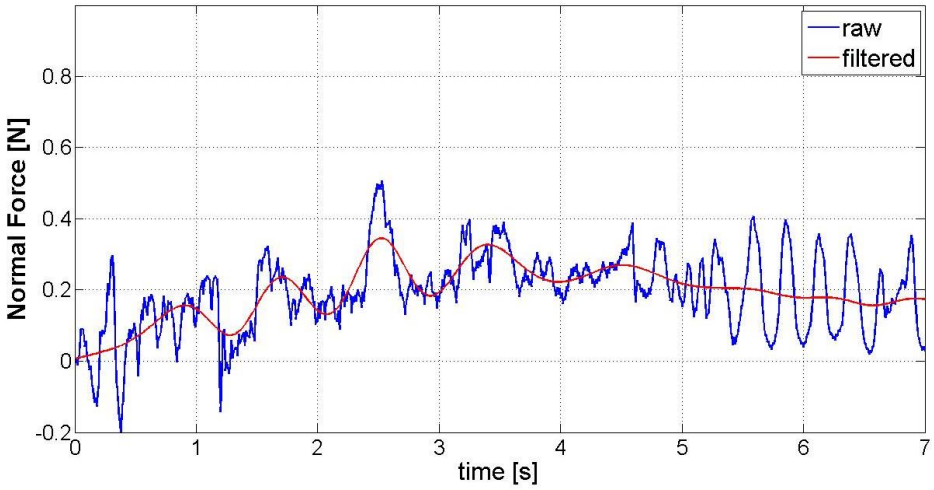

Figure 5.9 Time history of normal force component (filtered) for a pure pitch motion of 33 °/s

5.2.2 Case 2

Case 2 is the 65 °/s constant angular velocity pitch motion. Wing reaches 150º in 3.5 seconds. Figure 5.10 and Figure 5.11 shows the time history of the motion with wing view at different instants.

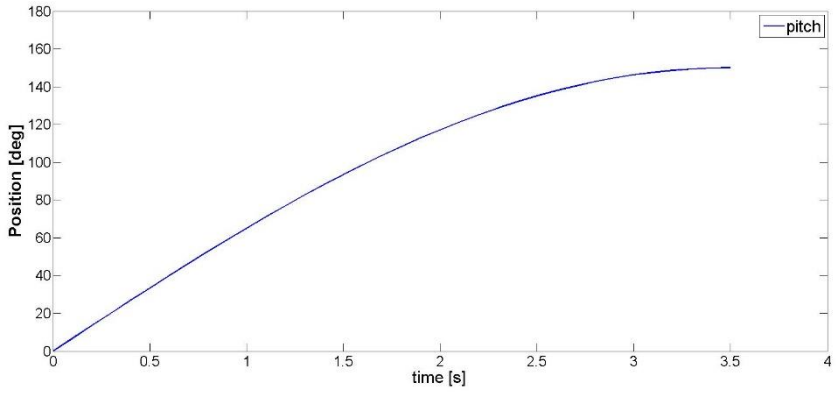

Figure 5.10 Time history of pitch angle for a pure pitch motion of 65 °/s

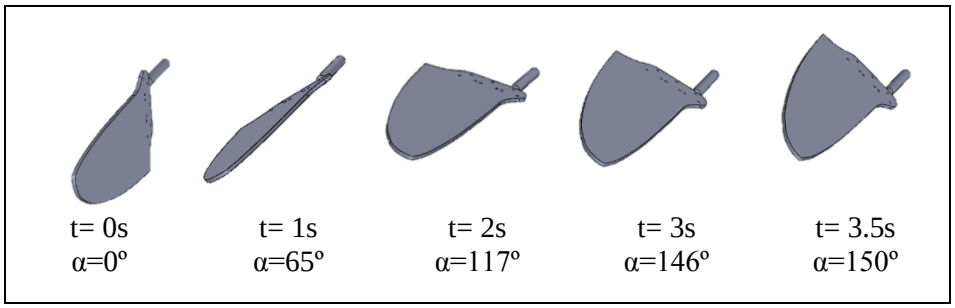

Figure 5.11 Wing position at different instants for a pure pitch motion of 65 °/s

Figure 5.12 shows the time history of normal force measurements during the constant pitching motion with 65 °/s. Frequency analysis of the force signal is shown in Figure 5.13. For this case, mechanical uncertainties are bigger than the previous case, also they start from 2 Hz. Note that, mechanical uncertainty increases proportionally with increasing pitching velocity.

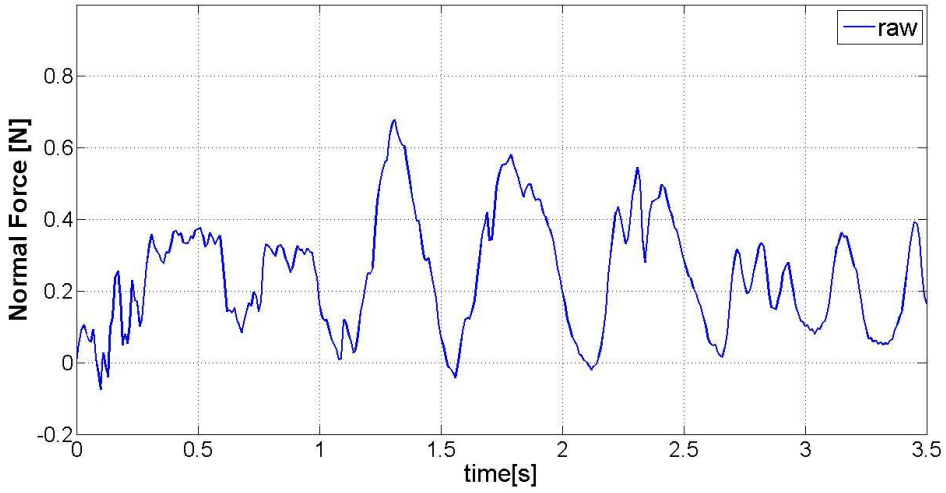

Figure 5.12 Time history of normal force component (raw data) for a pure pitch motion of 65 °/s

Force measurements is filtered by using a Butterworth filter with a cut-off frequency of 1 Hz. Figure 5.14 shows the time history of filtered normal force measurement. Filtered normal force data has less oscillations compared to Case 1 due to increased uncertainty frequency. Higher pitching velocities requires filtering with high cut-off frequency.

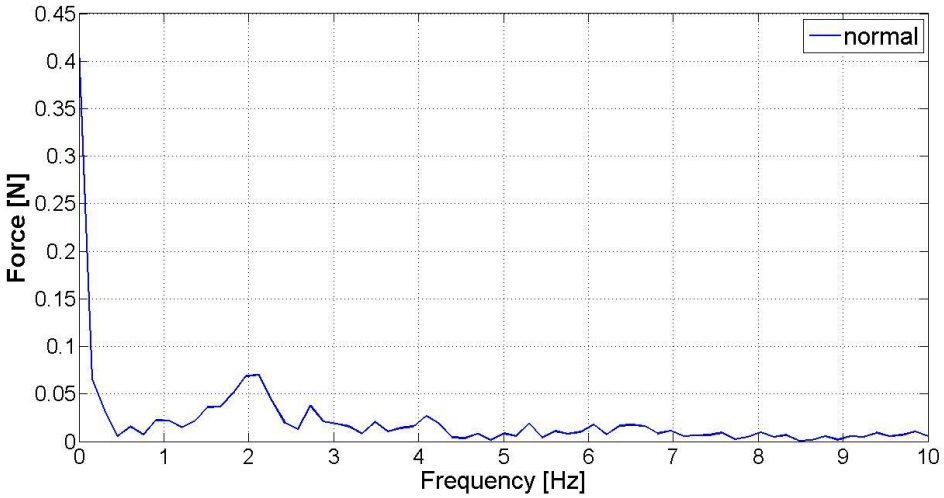

Figure 5.13 Normal force harmonic content for a pure pitch motion of 65 °/s

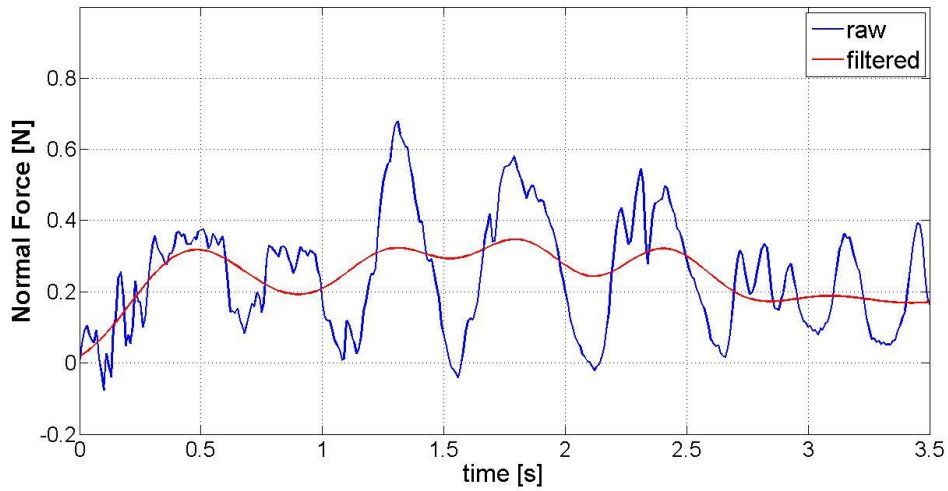

Figure 5.14 Time history of normal force component (filtered) for a pure pitch motion of 65 °/s

5.2.3 Comparison of the results

Comparison of the frequency composition of the normal force measurements of case 1 and case 2 is given in Figure 5.15. Magnitude of the error that is caused by mechanical uncertainties are less than 0.05 N for 33 °/s pitching velocity. On the other hand, magnitude of the error in normal force measurement is increased for the pitching velocity of 65 °/s. Hence, In order to have less uncertainty in the measurements system

should use low pitching velocities. Furthermore, this phenomenon indicates that pitch axes motion parts requires alterations.

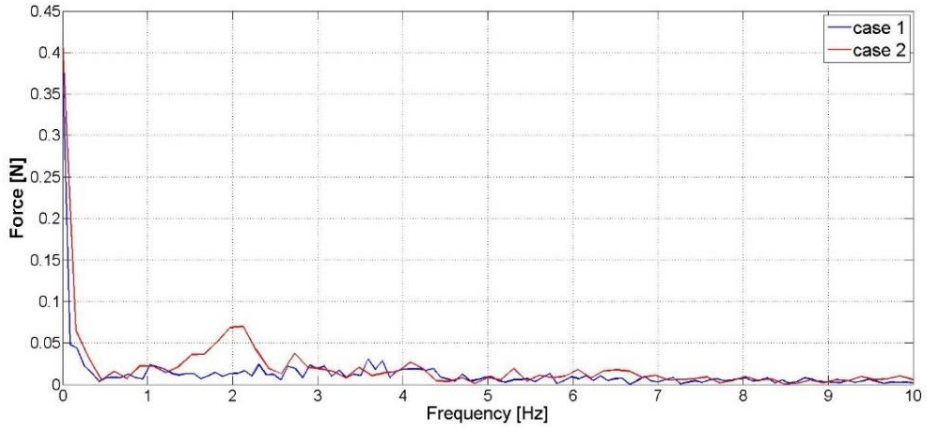

Figure 5.15 Normal force harmonic content comparison between case 1 (33 °/s) and case 2 (65 °/s)

Figure 5.16 shows the time history of the wing position for case 1 and case 2. In addition, Figure 5.17 gives the time history of force measurements for corresponding wing motions. Increasing the rotational velocity did not affect the maximum normal force measurement drastically. Although, the angular velocity of the pitch axes is doubled, maximum value of normal force is increased less than fifteen percent. Furthermore, for different velocities normal force approaches to nearly same value. Better physical reasoning can be obtain via flow measurements or CFD analysis.

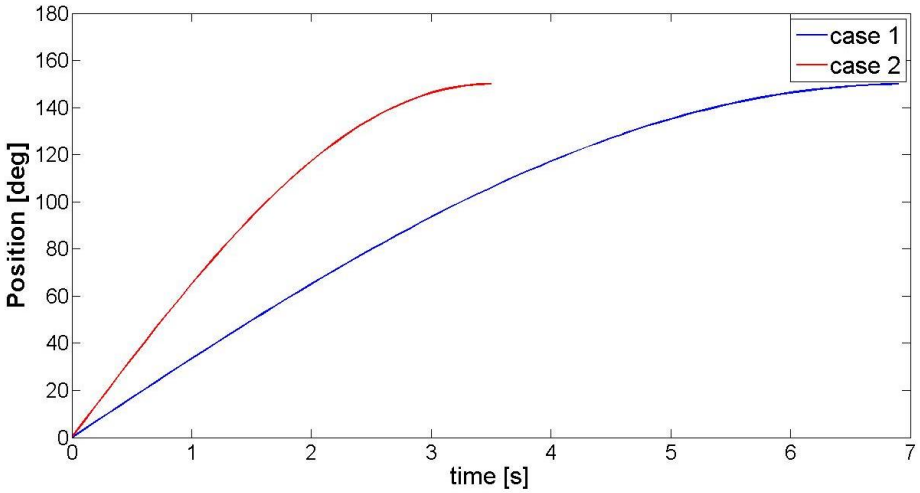

Figure 5.16 Time history of pitch angle for case 1 (33 °/s) and case 2 (65 °/s)

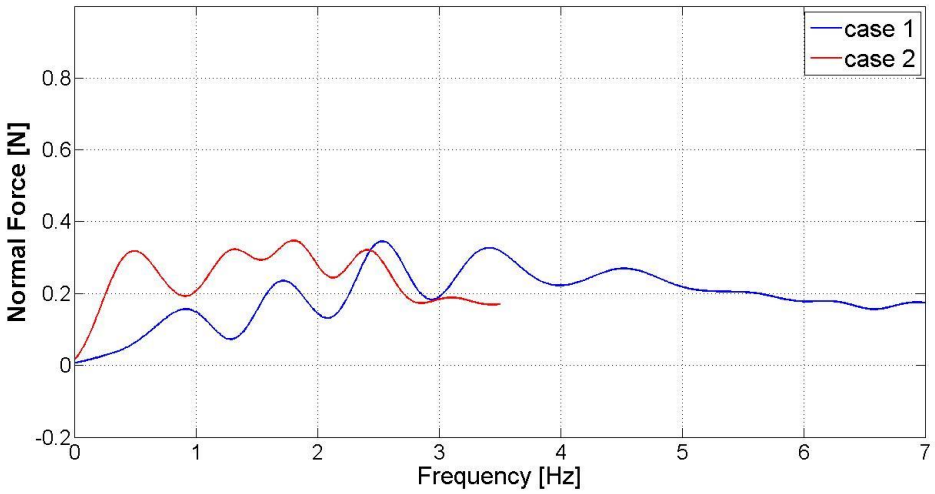

Figure 5.17 Time history of normal force for case 1 (33 º/s) and case 2 (65 º/s)

5.3 Results of Pure Plunge Impulsive Motion

Impulsive plunge motion is tested for constant pitch angle of 30º and 45º. Plunge motion starts with initial velocity and continue with constant velocity until the force measurement settle downs. Stroke limit is kept at 100º and angular speed for plunge motion is set to 58 º/s. Figure 5.18 shows the wing position time history for pure plunge motion, which is used in both case 1 and case 2.

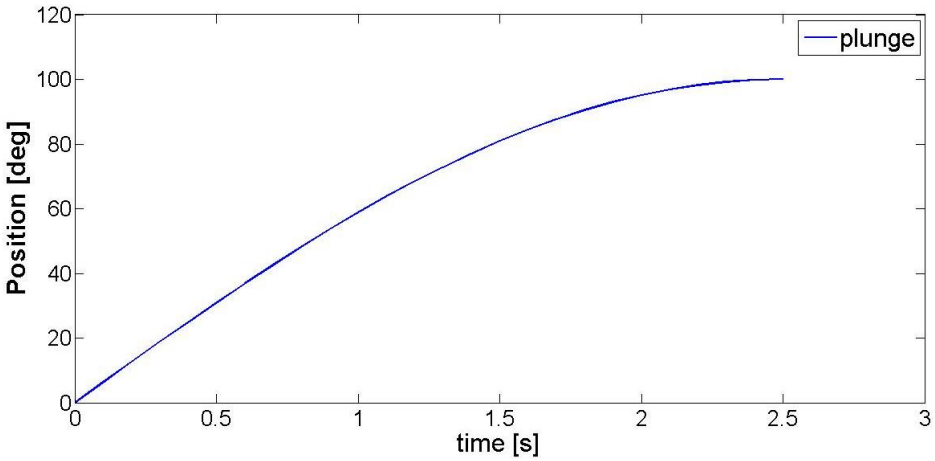

Figure 5.18 Time history of pitch angle for a pure plunge motion of 58 º/s

5.3.1 Case 1

Figure 5.19 gives the time history of normal force measurement raw data. Frequency decomposition of the raw data is obtained by applying FFT analysis to the raw data (Figure 5.20). Frequency analysis shows that the disturbances are between 1 Hz and 6 Hz. Figure 5.21 shows the time history of normal filtered force data.

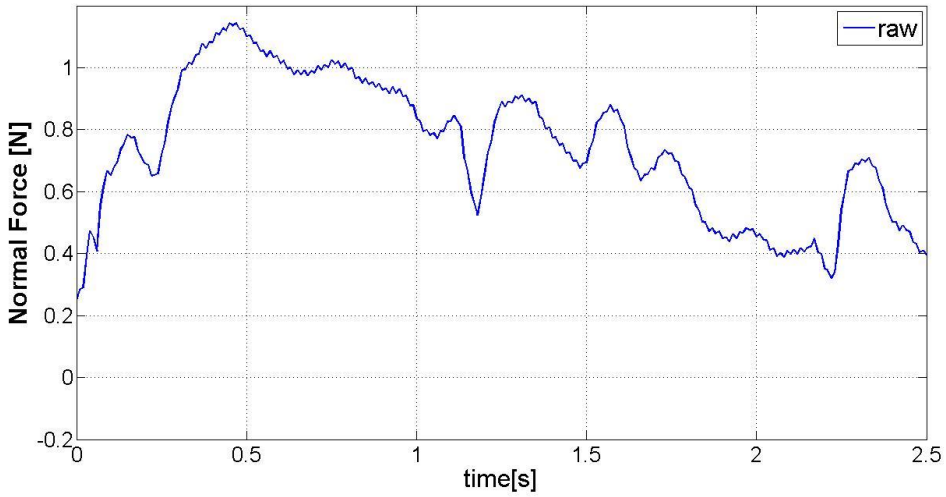

Figure 5.19 Time history of normal force (raw) for a pure plunge motion of 58 °/s with 30º constant pitch angle

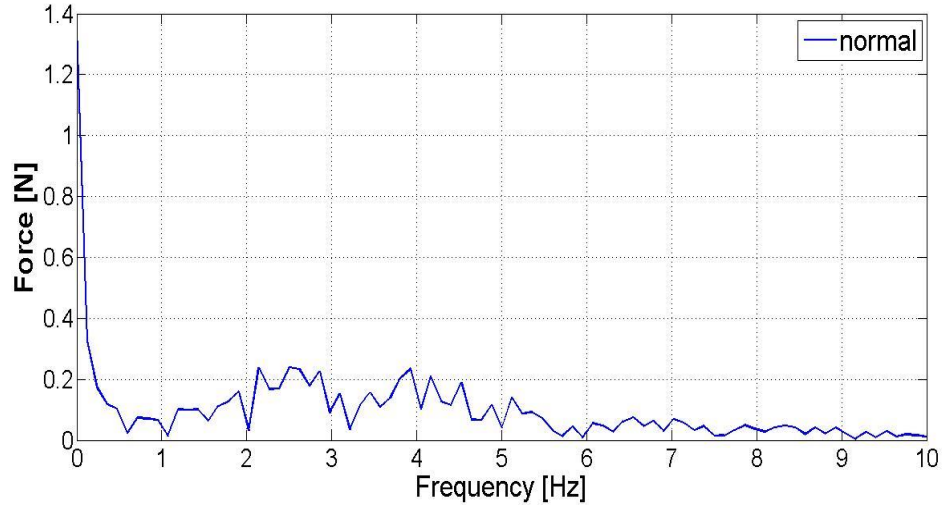

Figure 5.20 Normal force harmonic content for a pure plunge motion of 58 °/s with 30º constant pitch angle

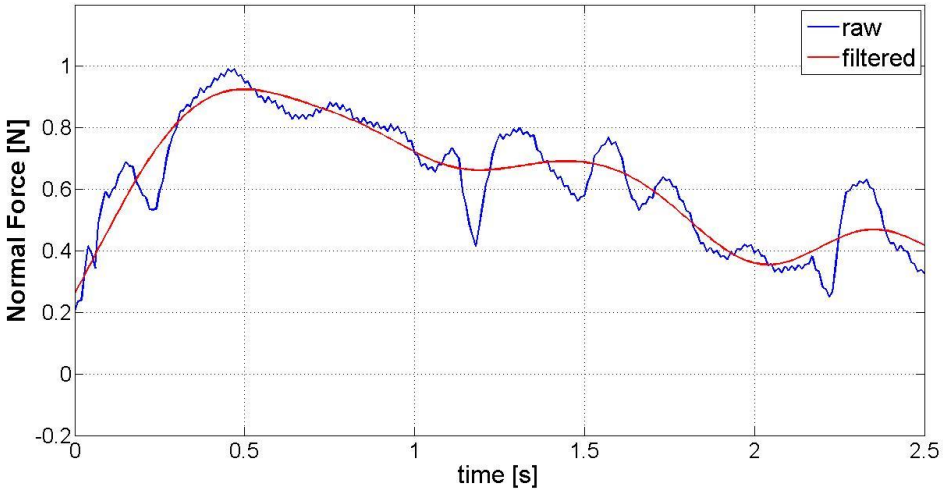

Figure 5.21 Time history of normal force (filtered) for a pure plunge motion of 58 °/s with 30º constant pitch angle

5.3.2 Case 2

Impulsive start with constant attack angle of 45º is used in case 2. Figure 5.22 shows the time history of the raw data of the normal force measurement.

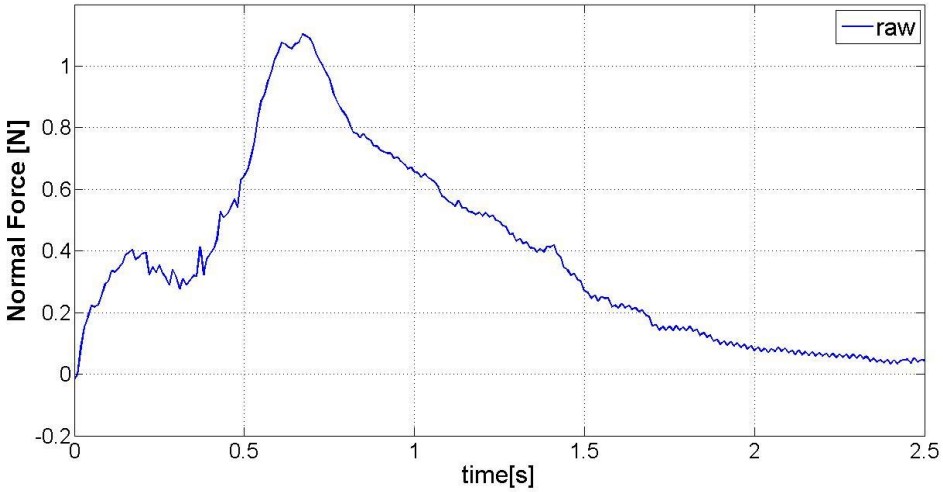

Figure 5.22 Time history of normal force (raw) for a pure plunge motion of 58 °/s with 45º constant pitch angle

Frequency analysis of the raw data is given in Figure 5.23. Normal force data is filtered by using a b Butterworth filter with cut-off frequency of 1.5 Hz. Filtered data is presented in Figure 5.24.

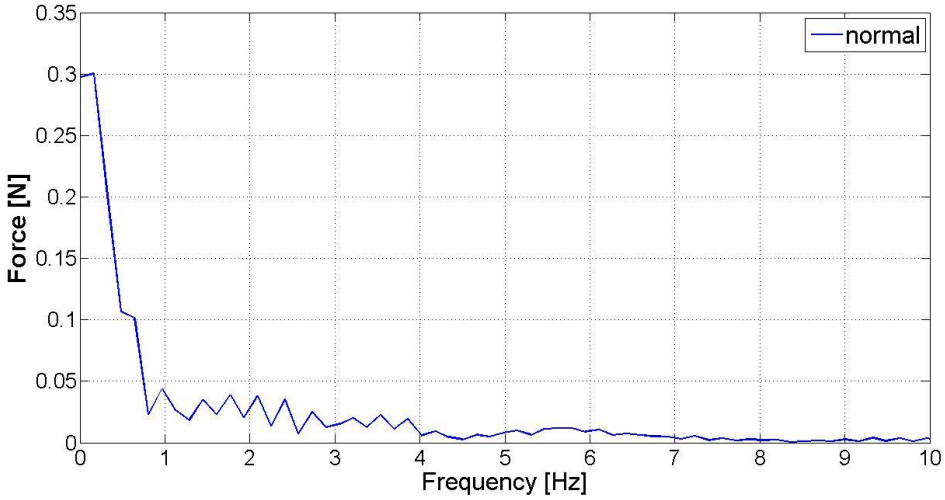

Figure 5.23 Normal force harmonic content for a pure plunge motion of 58 °/s with 45º constant pitch angle

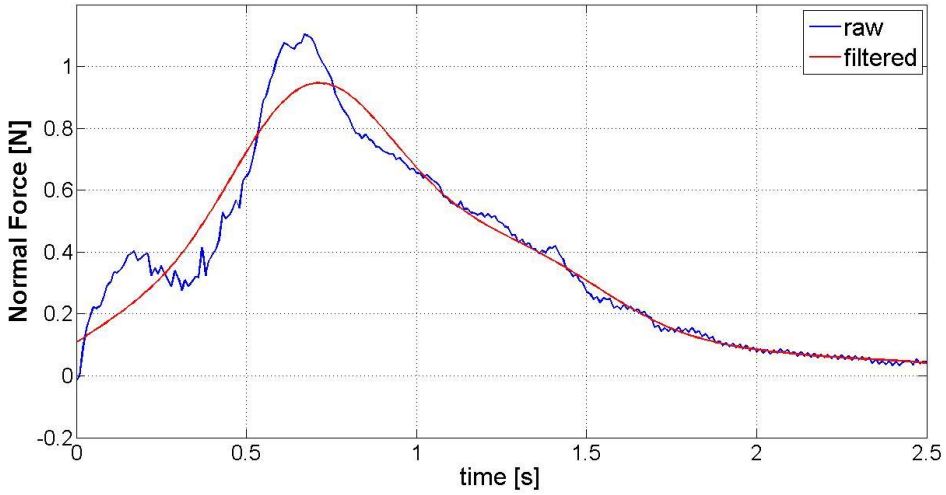

Figure 5.24 Time history of normal force (filtered) for a pure plunge motion of 58 °/s with 45º constant pitch angle

5.3.3 Comparison of the results

Frequency decomposition of the case 1 and case 2 are compared in Figure 5.25. Both case 1 and case 2 have similar frequency content with a slight differences in low and high frequencies. Time history of the normal force data compared in Figure 5.26.

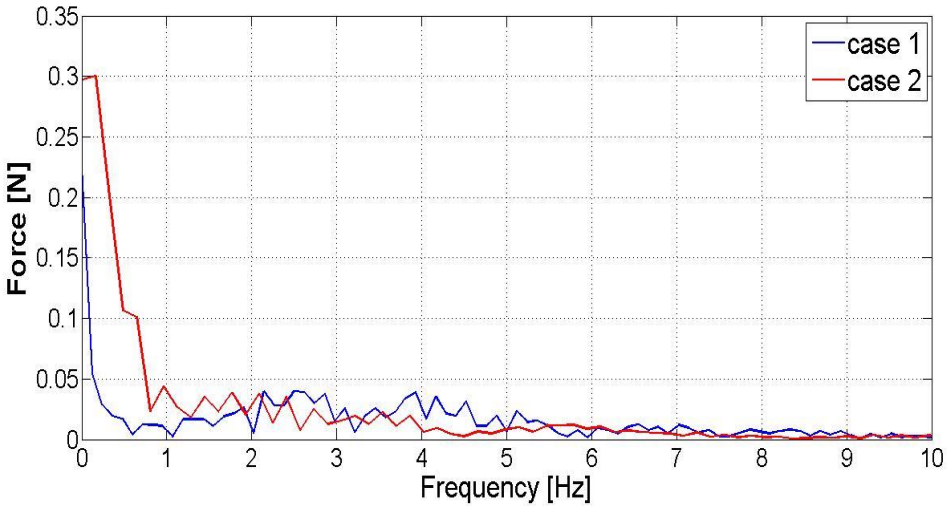

Figure 5.25 Normal force harmonic content for case1 (30º) and case 2 (45º)

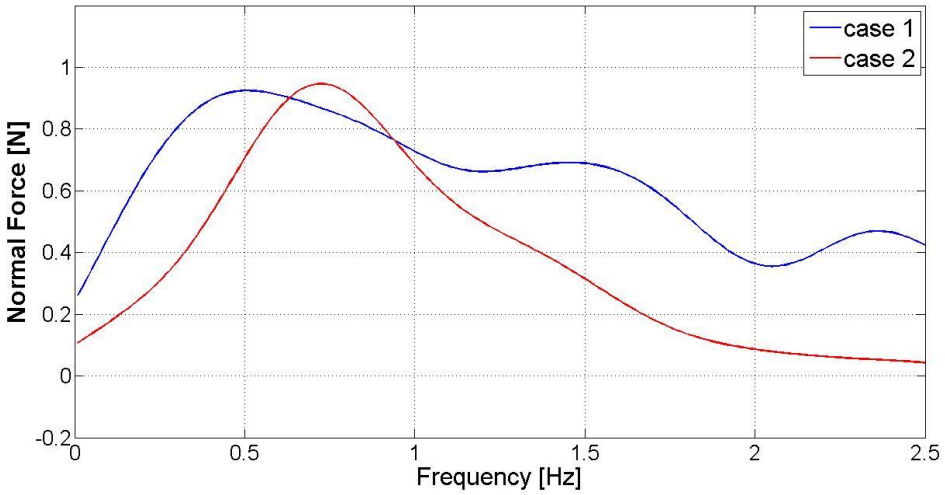

Figure 5.26 Time history of normal force (filtered) for case1 (30º) and case 2 (45º)

5.4 Results of Combined Pitch and Plunge Motion

5.4.1 Case 1

Case 1 considers a flapping trajectory of combined pitch and plunge motion with 30º pitch angle and 57º plunge angle at a frequency of 0.14. Figure 5.27 shows the motion trajectory graphically for both axes and wing position is illustrated in Figure 5.28 for a better understanding.

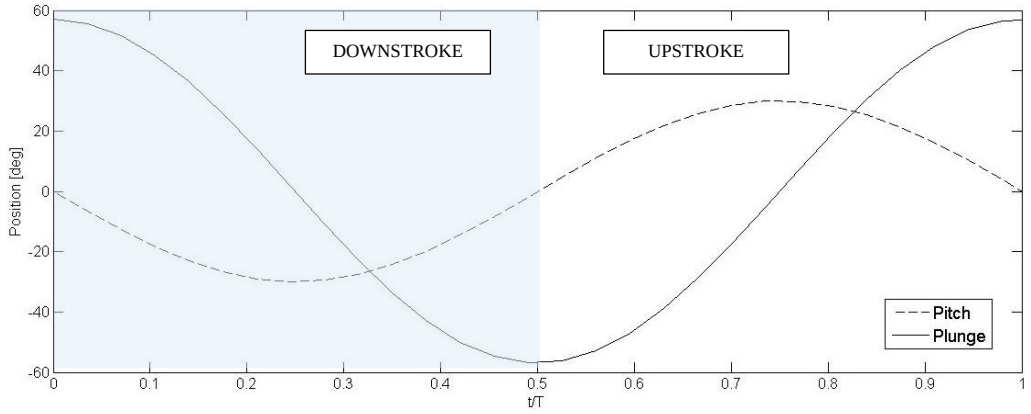

Figure 5.27 Time history of pitch and position angle for one period of a combined pitch and plunge motion (A_{pitch}=30º, A_{plunge}= 57º, f=0.14 Hz)

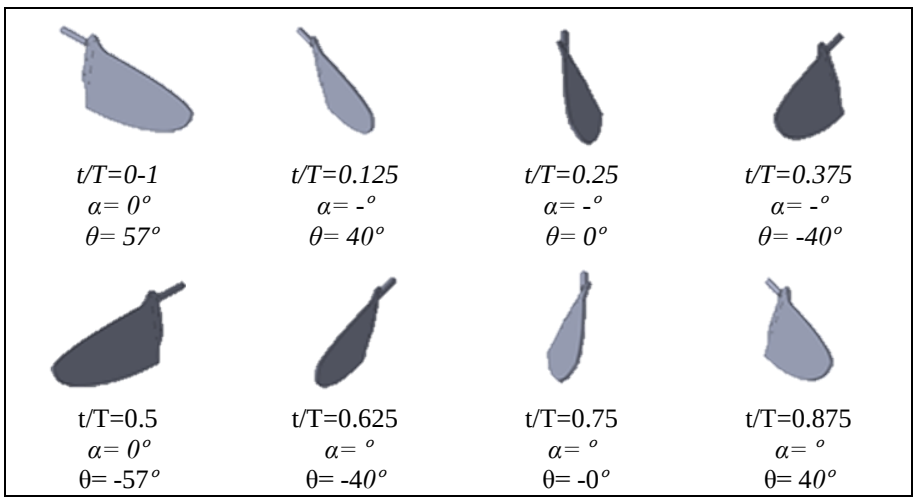

Figure 5.28 Wing position at different instants for a combined pitch and plunge motion (A_{pitch}=30º, A_{plunge}= 57º, f=0.14 Hz)

Raw force data for 10th period of the motion in normal and tangential directions to wing are given in Figure 5.29 and Figure 5.30. Tangential forces are nearly ten times smaller than the normal forces.

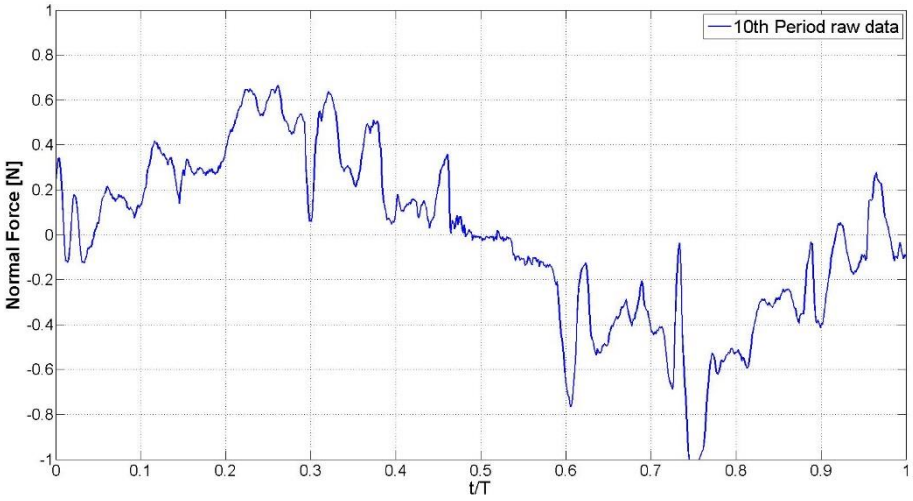

Figure 5.29 Time history of normal force (raw data) for a combined pitch-plunge motion of one period (A_{pitch}=30º, A_{plunge}= 57º, f=0.14 Hz)

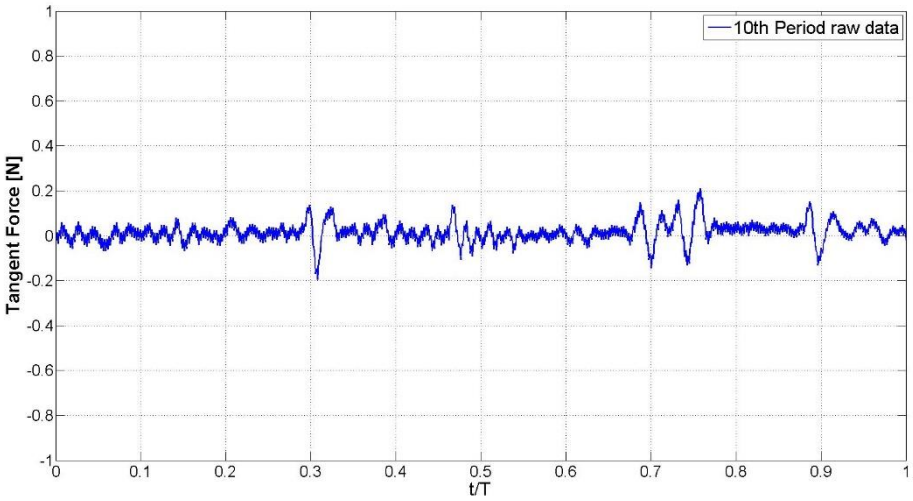

Figure 5.30 Time history of tangential force (raw data) for a combined pitch-plunge motion of one period (A_{pitch}=30º, A_{plunge}= 57º, f=0.14 Hz)

Fast Fourier Transform is applied to the data in order to obtain the frequency content of the data Figure 5.31. Raw data is filtered by using a Butterworth filter with a cut-

off frequency of 1.5 Hz. Results for phase averaged raw data of normal and tangential forces are presented in Figure 5.32 and Figure 5.33

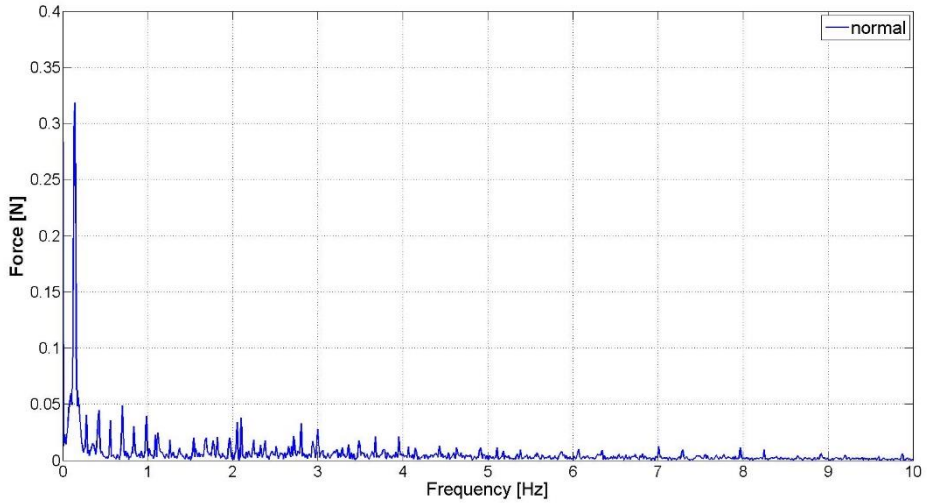

Figure 5.31 Normal force harmonic content for a combined pitch-plunge motion (A_{pitch}=30º, A_{plunge}= 57º, f=0.14 Hz)

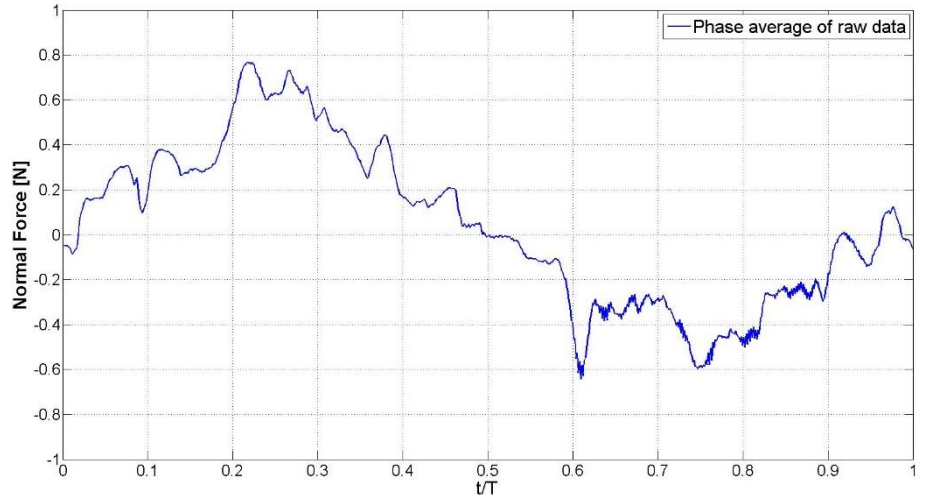

Figure 5.32 Time history of phase averaged normal force (raw data) for a combined pitch-plunge motion (A_{pitch}=30º, A_{plunge}= 57º, f=0.14 Hz)

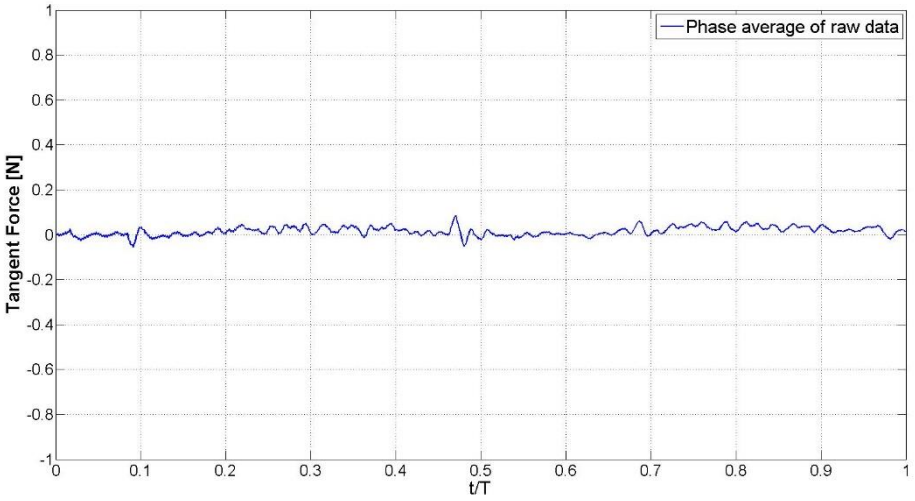

Figure 5.33 Time history of phase averaged tangential force (raw data) for a combined pitch-plunge motion (A_{pitch}=30º, A_{plunge}= 57º, f=0.14 Hz)

Phase average data is obtained from the filtered data by using a simple MATLAB code. Phase averaged and filtered normal and tangential force time history for a one flapping period are given in Figure 5.34 and Figure 5.35.

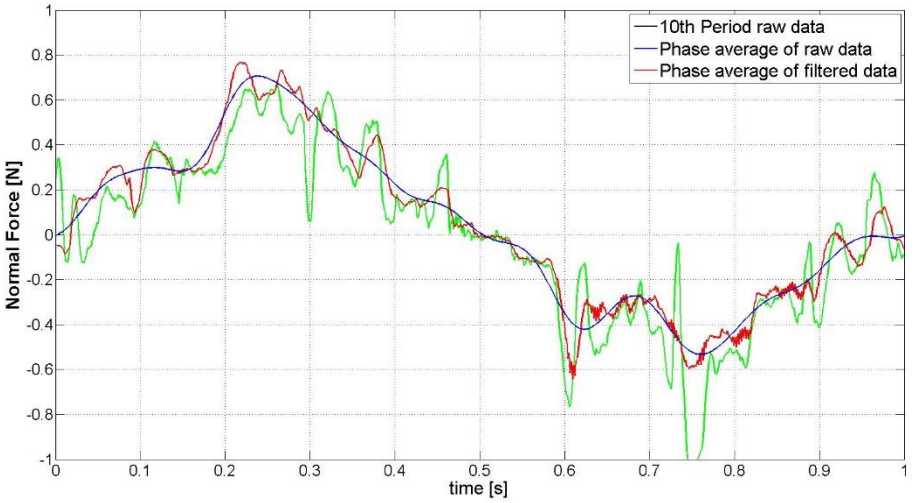

Figure 5.34 Time history of phase averaged normal force (filtered data) for a combined pitch-plunge motion (A_{pitch}=30º, A_{plunge}= 57º, f=0.14 Hz)

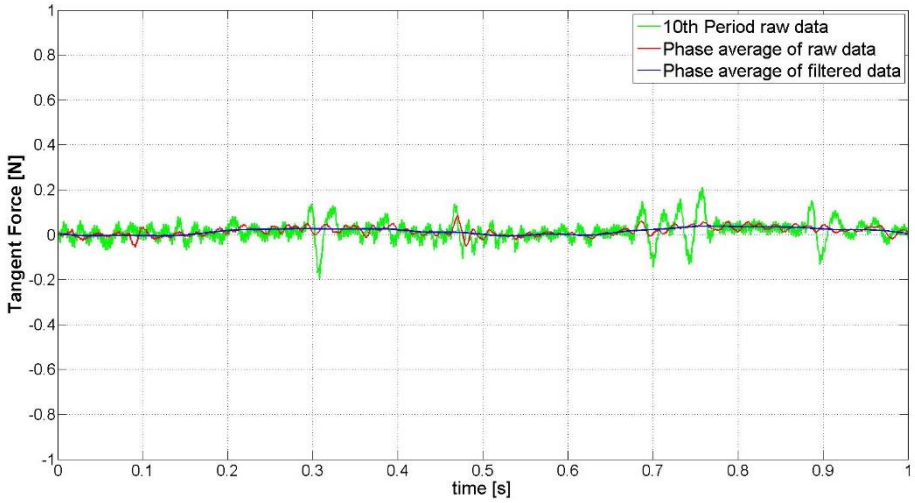

Figure 5.35 Time history of phase averaged tangential force (filtered data) for a combined pitch-plunge motion (A_{pitch}=30º, A_{plunge}= 57º, f=0.14 Hz)

Total aerodynamic force time history is obtained by adding up the normal and tangential vectors. Total force magnitude time history is given in Figure 5.36. Moreover, force vectors are shown in the Figure 5.37. Exact time and position of the wing is specified for each instant and force directions and magnitudes are properly illustrated.

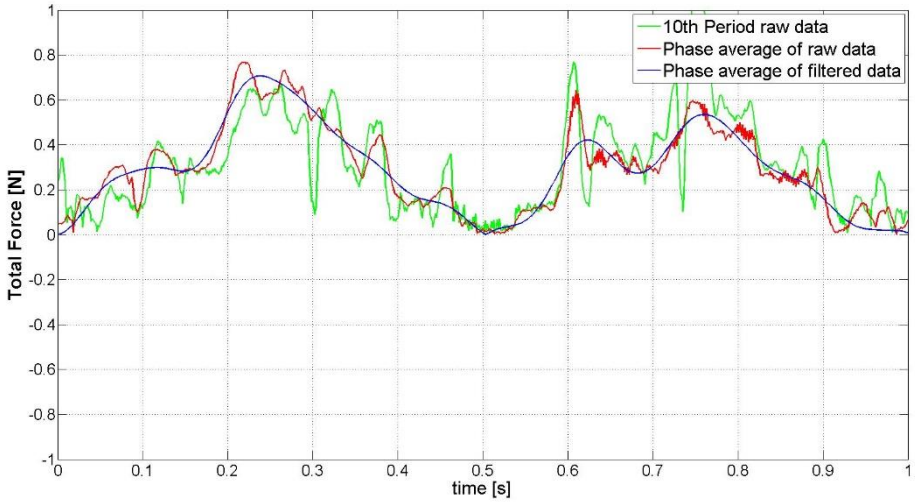

Figure 5.36 Time history of total force (phase averaged data) for a combined pitch-plunge motion (A_{pitch}=30º, A_{plunge}= 57º, f=0.14 Hz)

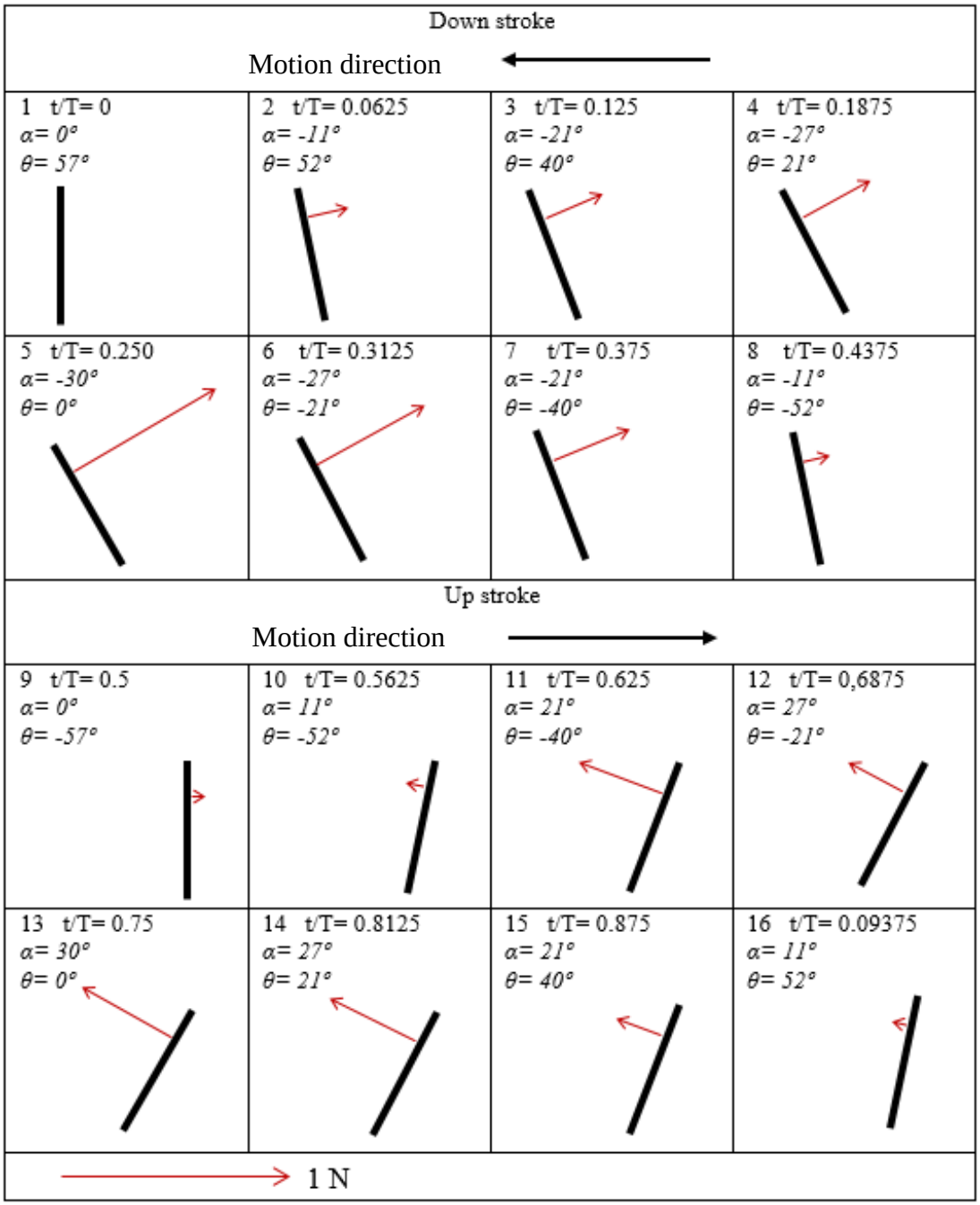

Figure 5.37 Definition of total 'thrust' force vector for a flapping motion of combined pitch-plunge motion (A_{pitch}=30º, A_{plunge}= 57º, f=0.14 Hz)

5.4.2 Case 2

A wing trajectory with same plunge motion, which has different pitch amplitude, is used in the Case 2. Figure 5.38 shows the position history of pitch and plunge angle for one period and Figure 5.39 illustrates the wing positions for case 2 at different instants.

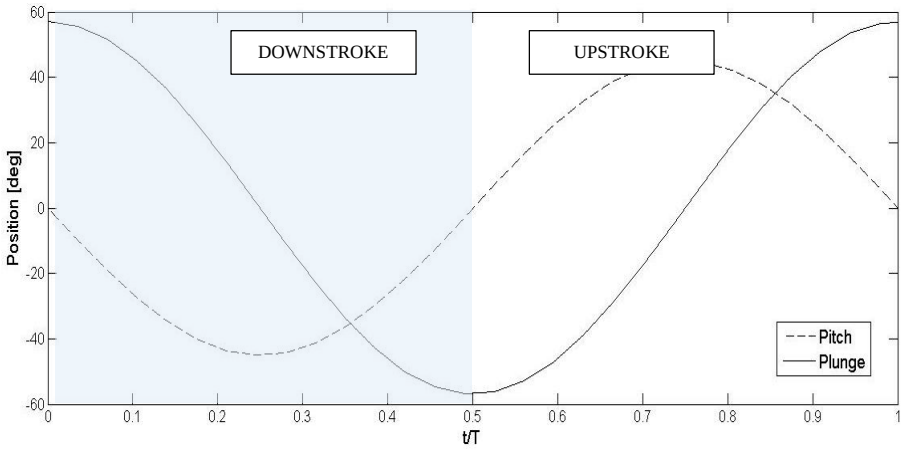

Figure 5.38 Time history of pitch and position angle for one period of a combined pitch and plunge motion (A_{pitch}= 45º, A_{plunge}= 57º, f=0.14 Hz)

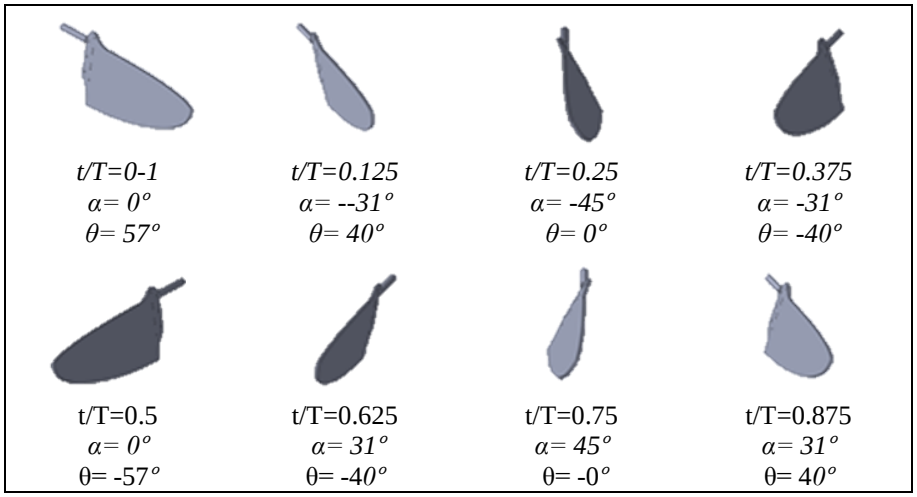

Figure 5.39 Wing position at different instants for a combined pitch and plunge motion (A_{pitch}= 45º, A_{plunge}= 57º, f=0.14 Hz)

Raw force data of 10th period of the motion for normal and tangential direction are given in Figure 5.40 and Figure 5.41. Frequency distribution of the raw data is given in the Figure 5.42.

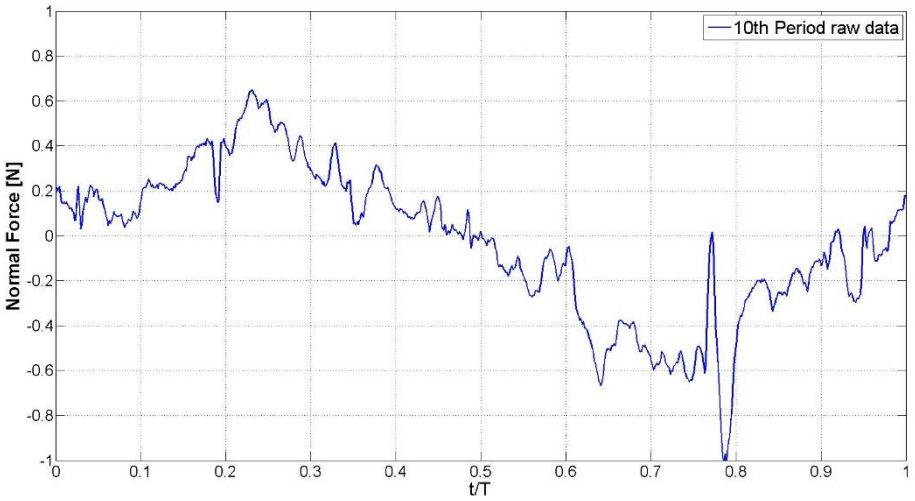

Figure 5.40 Time history of normal force (raw data) for a combined pitch-plunge motion (A_{pitch}= 45º, A_{plunge}= 57º, f=0.14 Hz)

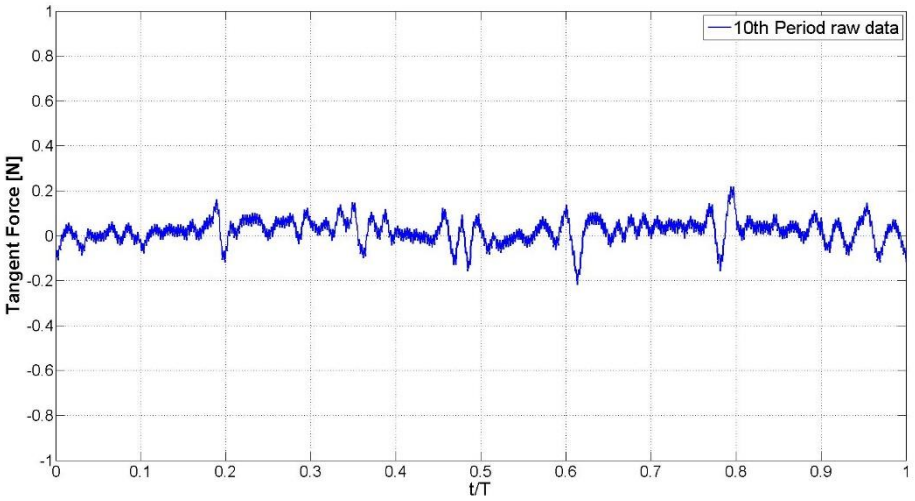

Figure 5.41 Time history of normal and tangential force (filtered raw data) for combined pitch-plunge motion (A_{pitch}= 45º, A_{plunge}= 57º, f=0.14 Hz)

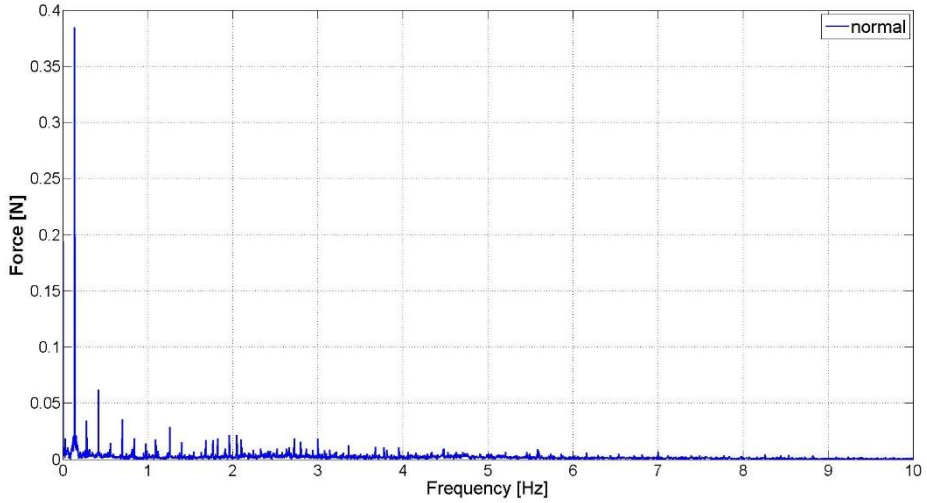

Figure 5.42 Normal force harmonic content for a combined pitch-plunge motion (A_{pitch}= 45º, A_{plunge}= 57º, f=0.14 Hz)

Phase average of raw data in normal and tangential directions are presented in Figure 5.43 and Figure 5.44.

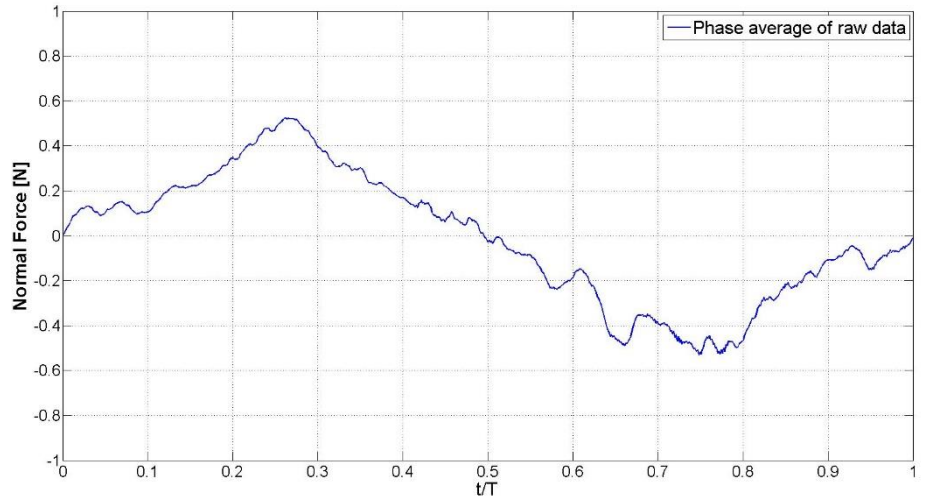

Figure 5.43 Time history of phase averaged normal force (raw data) for a combined pitch-plunge motion (A_{pitch}= 45º, A_{plunge}= 57º, f=0.14 Hz)

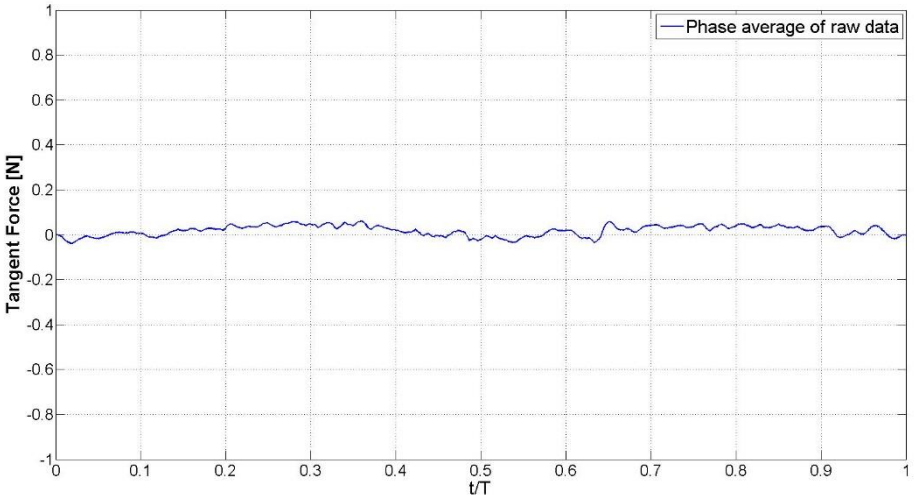

Figure 5.44 Time history of phase averaged tangential force (raw data) for a combined pitch-plunge motion (A_{pitch}= 45º, A_{plunge}= 57º, f=0.14 Hz)

Phase average of the filtered data is taken by using a simple MATLAB code. Phase averaged force data for normal and tangential direction are given in Figure 5.45 and Figure 5.46.

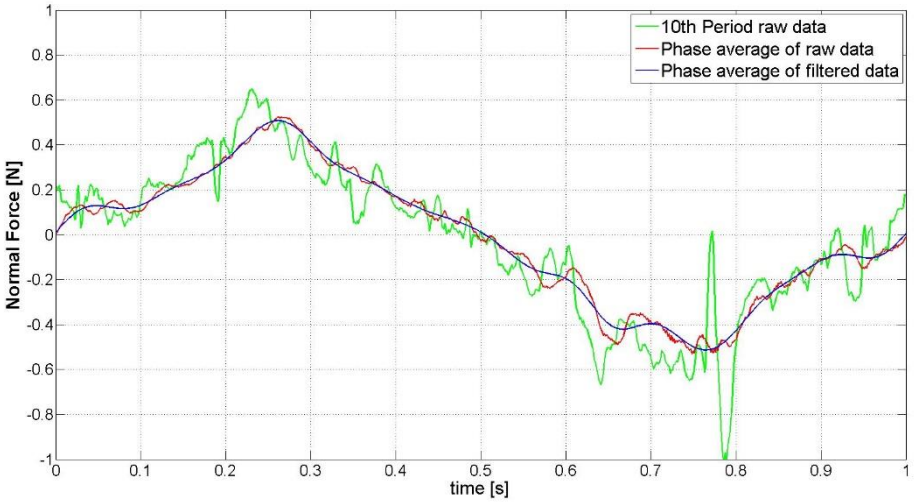

Figure 5.45 Time history of phase averaged normal force (filtered data) for a combined pitch-plunge motion (A_{pitch}= 45º, A_{plunge}= 57º, f=0.14 Hz)

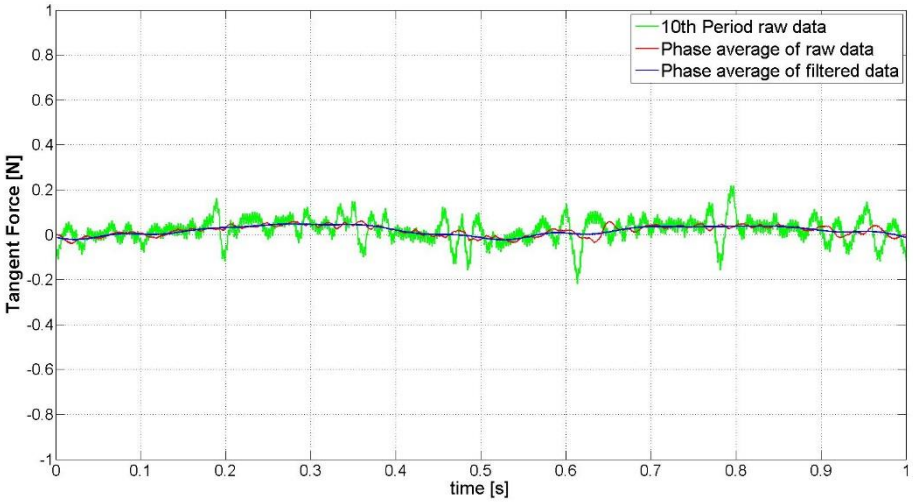

Figure 5.46 Time history of phase averaged tangential force (filtered data) for a combined pitch-plunge motion (A_{pitch}= 45º, A_{plunge}= 57º, f=0.14 Hz)

Total aerodynamic force is calculated by using normal and tangential force components is presented in Figure 5.47. Finally, Figure 5.48 shows the wing position and the total force vector for different instants.

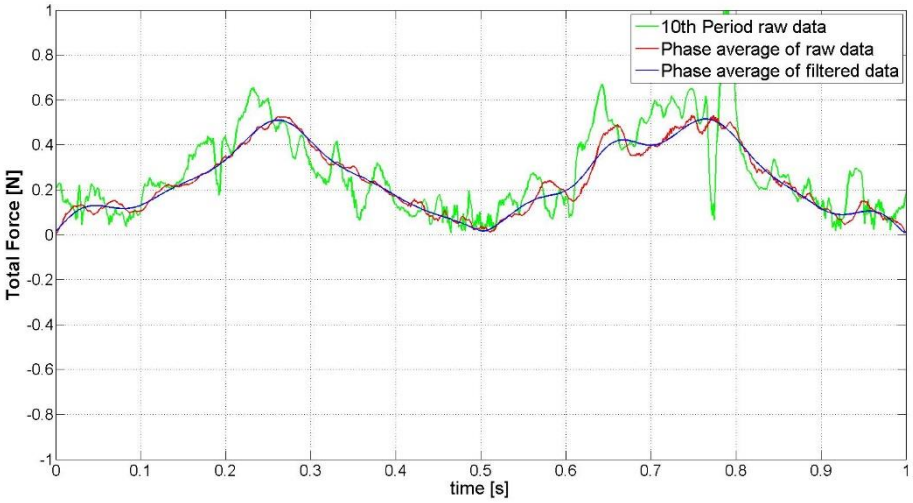

Figure 5.47 Time history of total force (phase averaged data) for a combined pitch-plunge motion (A_{pitch}= 45º, A_{plunge}= 57º, f=0.14 Hz)

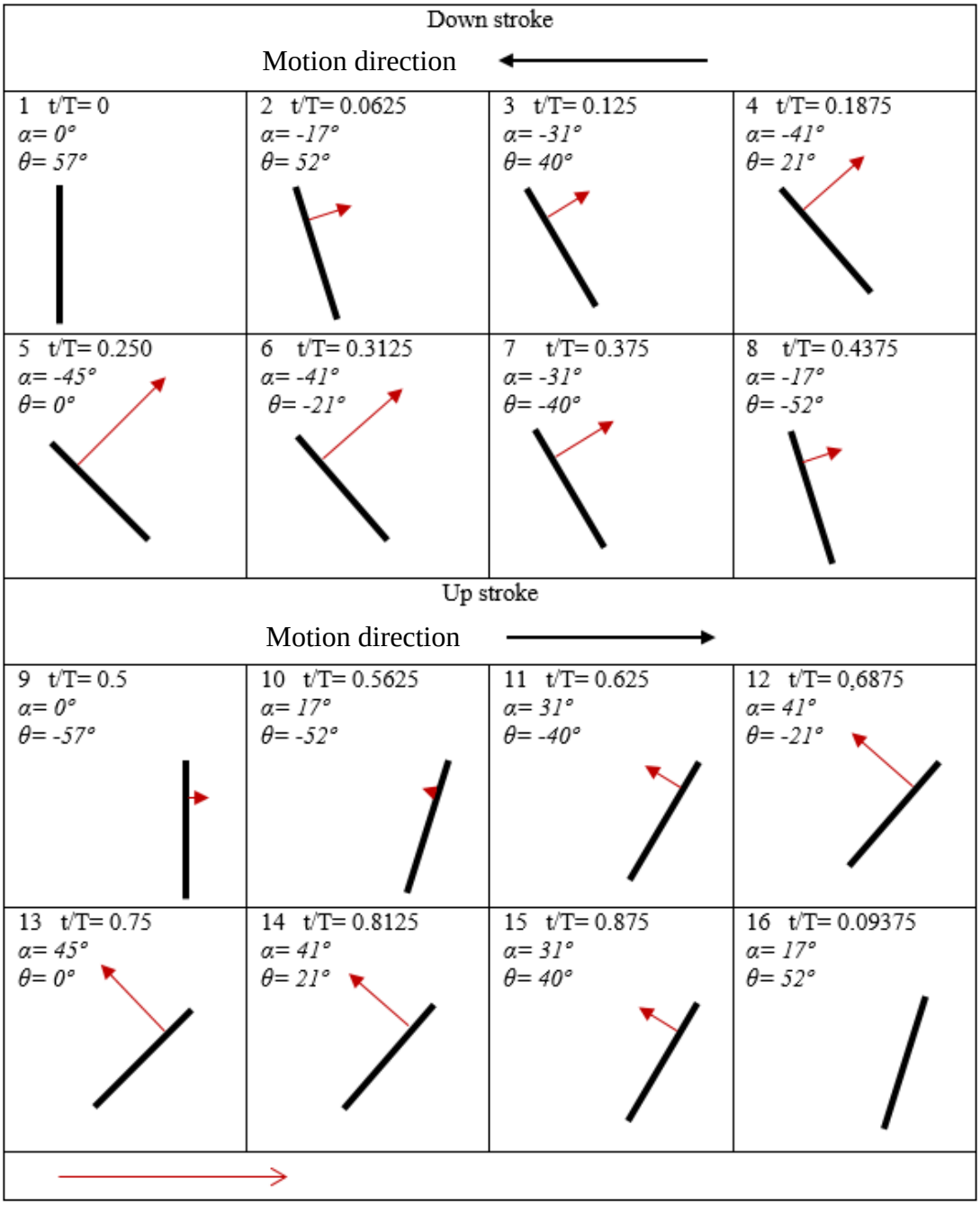

Figure 5.48 Definition of total 'thrust' force vector for a flapping motion of combined pitch-plunge motion (A_{pitch}= 45º, A_{plunge}= 57º, f=0.14 Hz)

5.4.3 Case 3

Motion kinematics, which are based on the kinematics of the Hawkmoth as measured by Willmott and Elington [53], are presented in the Morrison's study [46], in which wing motion of the Hawkmoth with two bio-inspired trajectory and a sinusoidal trajectory are tested (Figure 5.49). In the current study only the sinusoidal motion is considered. Pitch axis and plunge axis have 90 degrees phase shift in between. Wing reaches the maximum attack angle of 57 degree at the mid stroke (Figure 5.50). Frequency of the motion is 0.14 Hz accordingly to validation experiments.

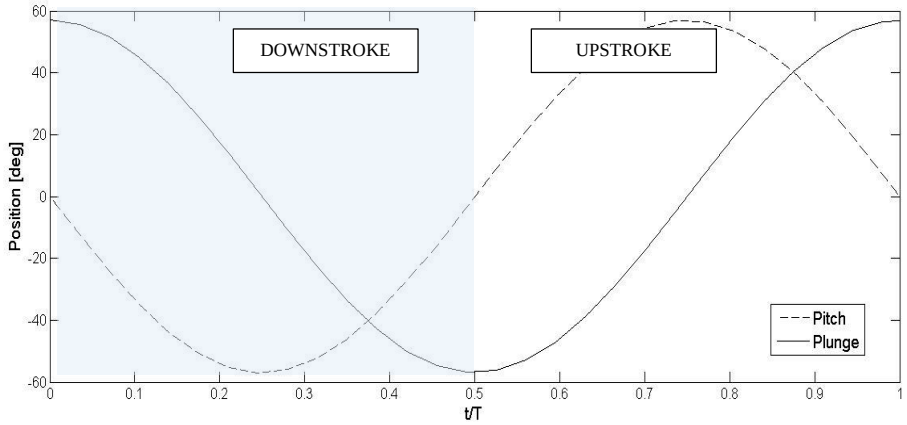

Figure 5.49 Time history of pitch and position angle for one period of a combined pitch and plunge motion (A_{pitch}=57º, A_{plunge}= 57º, f=0.14 Hz)

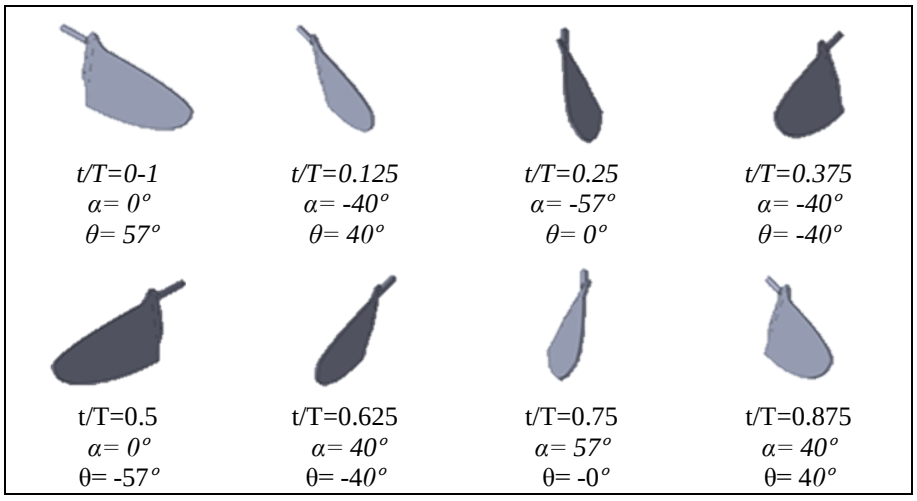

Figure 5.50 Wing position at different instants for a combined pitch and plunge motion (A_{pitch}=57º, A_{plunge}= 57º, f=0.14 Hz)

Figure 5.51 shows time history of the normal forces acting on the wing during the 10th period. General trend of the force variation for one period can be observed in both cases. Also, matching peak values for force measurements are observed.

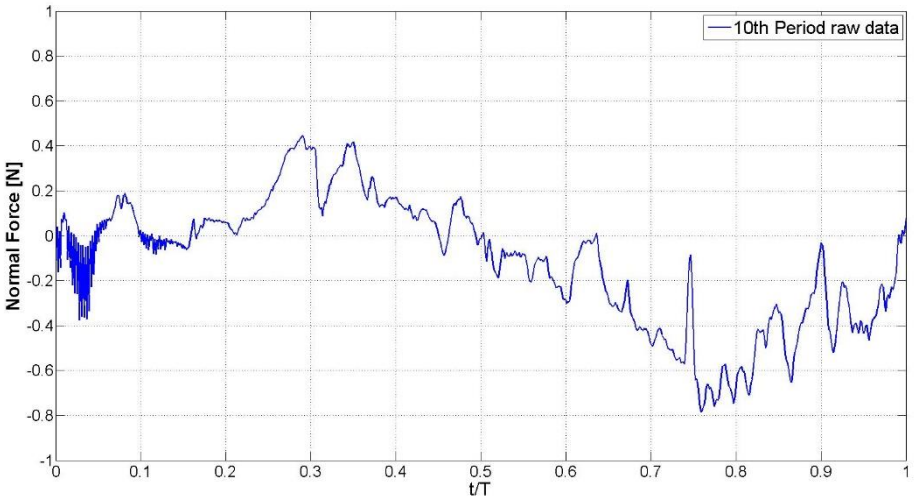

Figure 5.51 Time history of normal force (raw data) for a combined pitch-plunge motion (A_{pitch}=57º, A_{plunge}= 57º, f=0.14 Hz)

Figure 5.52 presents the time history of tangential forces. General trend for tangential forces are captured.

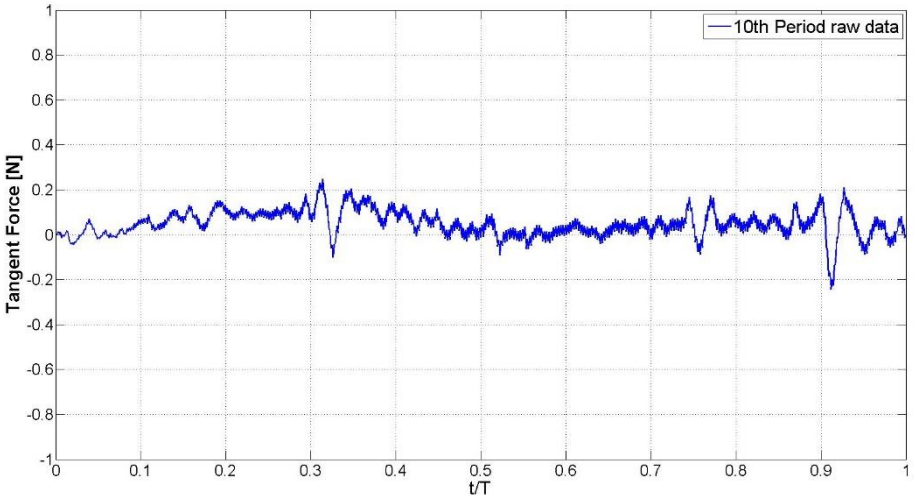

Figure 5.52 Time history of normal and tangential force (filtered raw data) for combined pitch-plunge motion (A_{pitch}=57º, A_{plunge}= 57º, f=0.14 Hz)

Frequency analysis of the force signal is presented in Figure 5.53. Phase averaged raw data results for normal and tangential direction are presented in Figure 5.54 and Figure 5.55.

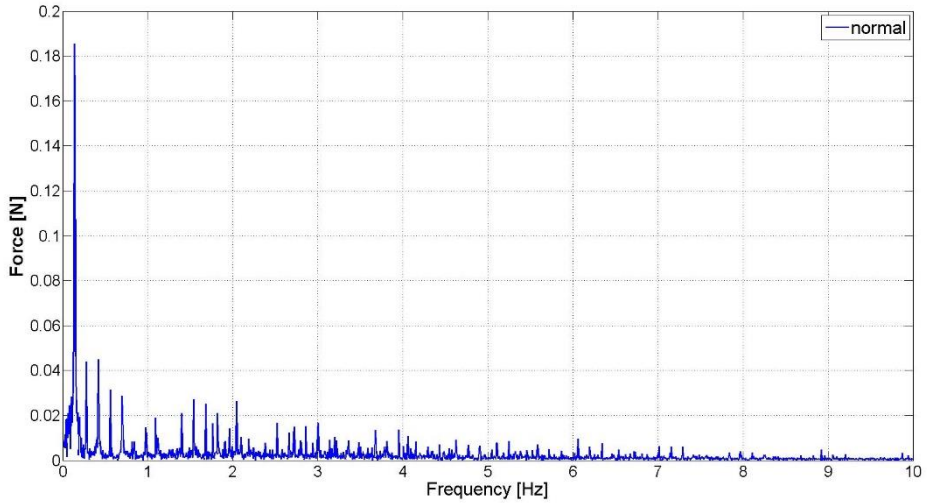

Figure 5.53 Normal force harmonic content for a combined pitch-plunge motion (A_{pitch}=57º, A_{plunge}= 57º, f=0.14 Hz)

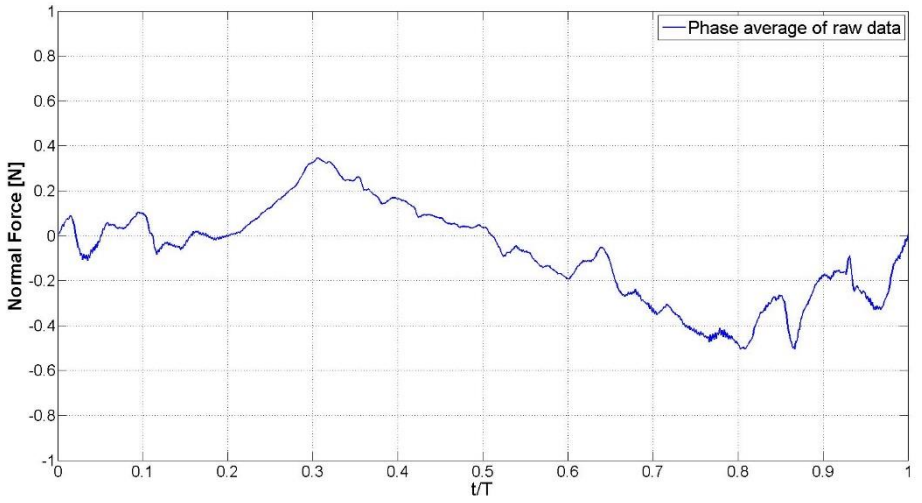

Figure 5.54 Time history of phase averaged normal force (raw data) for a combined pitch-plunge motion (A_{pitch}=57º, A_{plunge}= 57º, f=0.14 Hz)

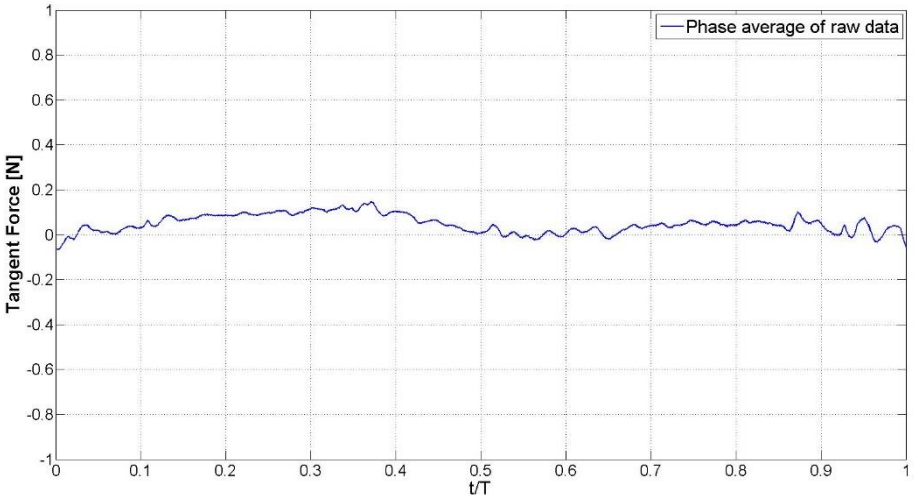

Figure 5.55 Time history of phase averaged tangential force (raw data) for a combined pitch-plunge motion (A_{pitch}=57º, A_{plunge}= 57º, f=0.14 Hz)

Phase average of the filtered normal and tangential forces are presented in Figure 5.56 and Figure 5.57 with comparison between the the current experiment and the validation case. The results are obtained from the experimental measurements with the ATI NANO17 of the test case are plotted and compared with the results from validation case. An open source software 'Graph digitizer' is used for extracting numerical data from the graphical results of the validation case [54].

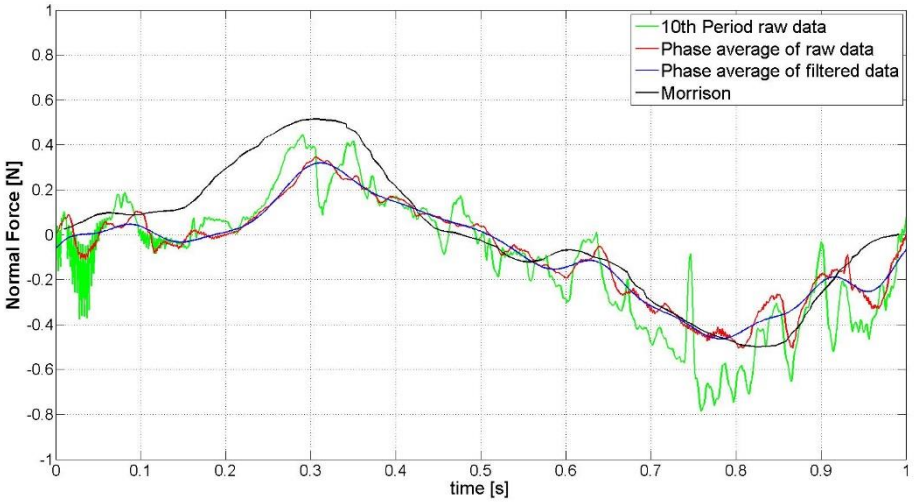

Figure 5.56 Time history of phase averaged normal force (filtered data) for a combined pitch-plunge motion (A_{pitch}=57º, A_{plunge}= 57º, f=0.14 Hz)

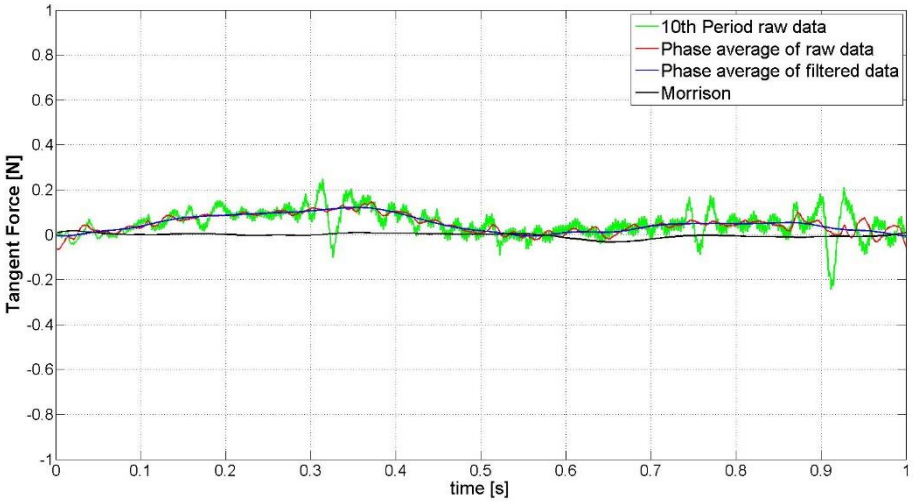

Figure 5.57 Time history of phase averaged tangential force (filtered data) for a combined pitch-plunge motion (A_{pitch}=57º, A_{plunge}= 57º, f=0.14 Hz)

Figure 5.58 shows the phase average of the filtered total forces with comparison between the the current experiment and the validation case. Finally, Figure 5.59 shows the wing position and the total force vector for different instants.

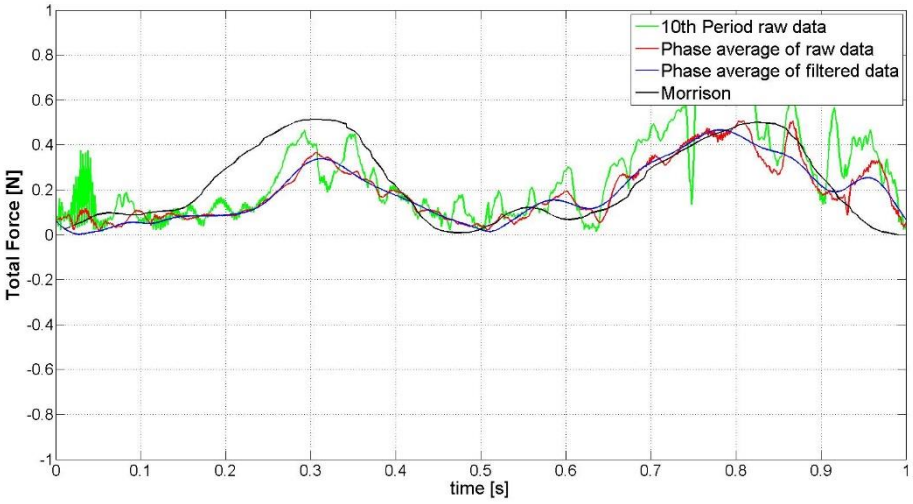

Figure 5.58 Time history of total force (phase averaged data) for a combined pitch-plunge motion (A_{pitch}=57º, A_{plunge}= 57º, f=0.14 Hz)

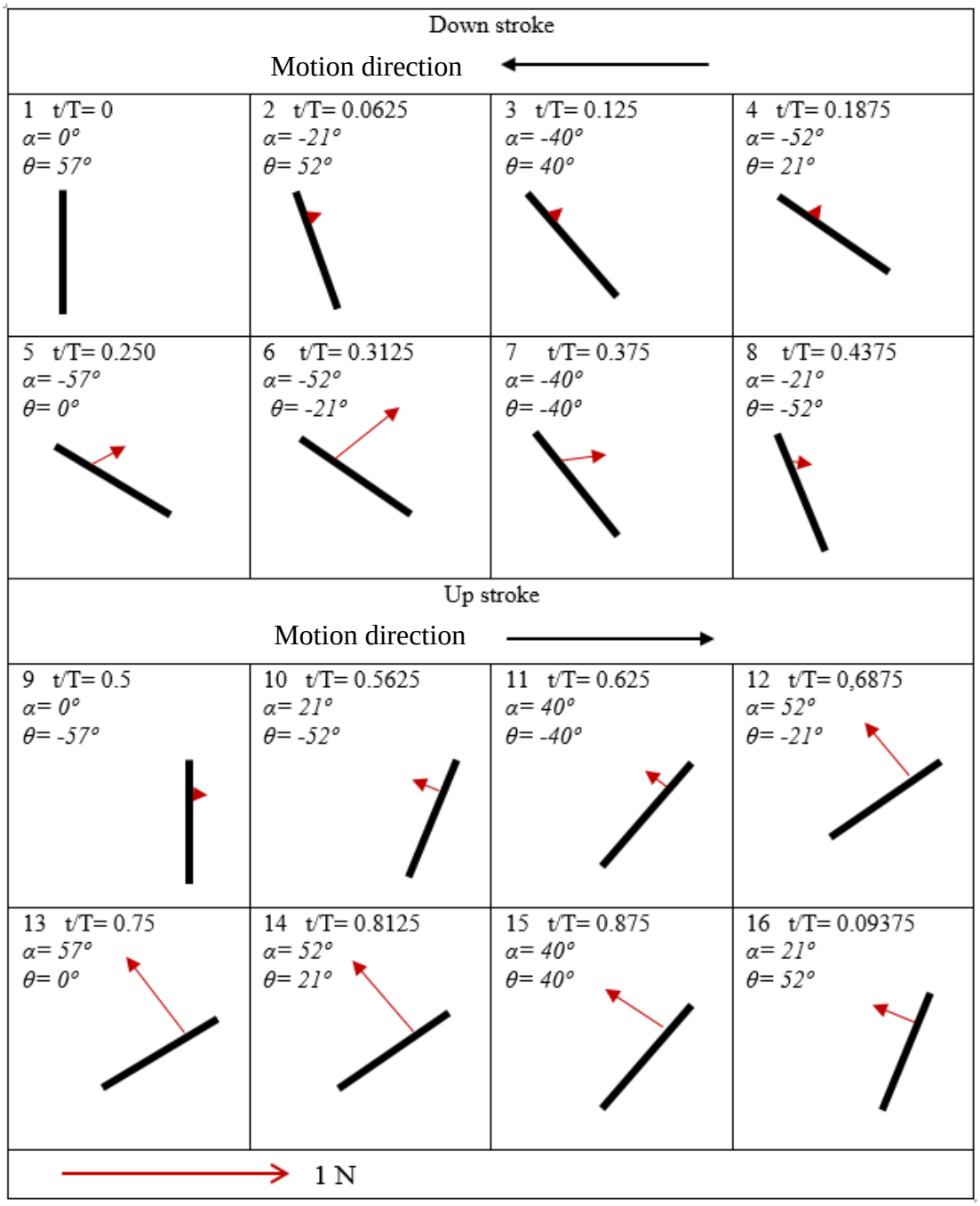

Figure 5.59 Definition of total 'thrust' force vector for a flapping motion of combined pitch-plunge motion (A_{pitch}=57º, A_{plunge}= 57º, f=0.14 Hz)

5.4.4 Comparison of the Results

Kinematics of the case 3 and the Morrison's experiment are same whereas case 1 and case2 use different pitch angle values. Low angle of attack pitching trajectories gave high normal force whereas the tangential force generation increases with increasing attack angle. Figure 5.60 and Figure 5.61 shows the time history of phase averaged normal and tangential forces for one period. Also, total force time history given in Figure 5.62.

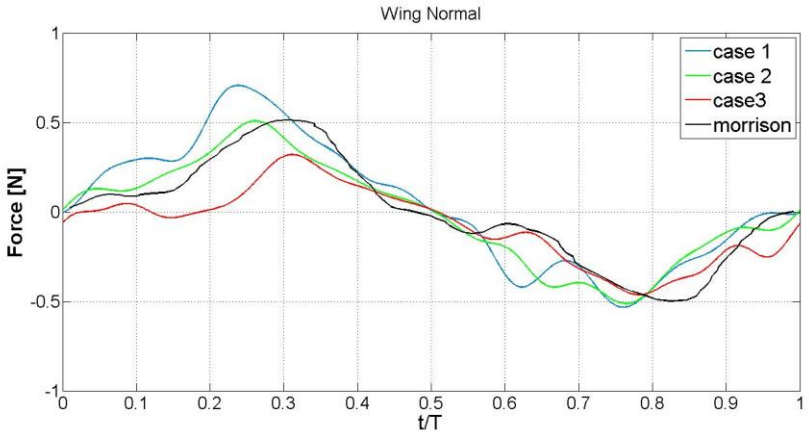

Figure 5.60 Comparison of the phase averaged normal force time histories of case 1 (A_{pitch}=30º), case 2 (A_{pitch}=45º), case 3 (A_{pitch}=57º) and Morrison's experiment (A_{pitch}=57º) for one period of flapping motion

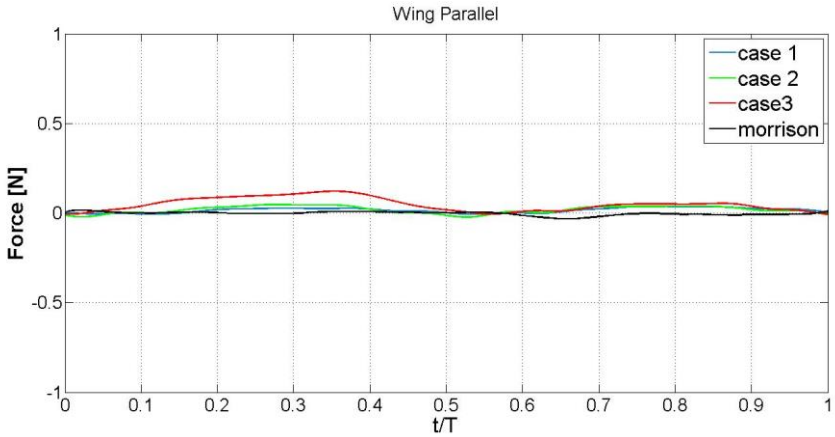

Figure 5.61 Comparison of the phase averaged tangent force time histories of case 1 (A_{pitch}=30º), case 2 (A_{pitch}=45º), case 3 (A_{pitch}=57º) and Morrison's experiment (A_{pitch}=57º) for one period of flapping motion

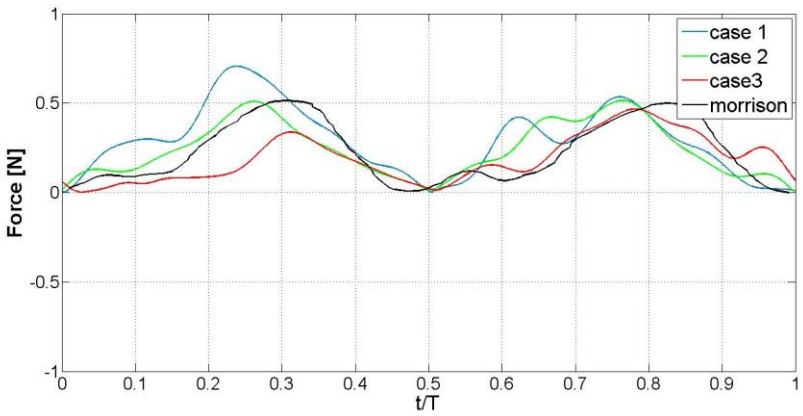

Figure 5.62 Comparison of the phase averaged total force time histories of case 1 (A_{pitch}=30º), case 2 (A_{pitch}=45º), case 3 (A_{pitch}=57º) and Morrison's experiment (A_{pitch}=57º) for one period of flapping motion

Peak force measurements are observed at 0.25 t/T and 0.75 t/T. Also maximum plunge velocity and the maximum pitch angle are also occurs at 0.25 t/T and 0.75 t/T. Furthermore; at 0.5 t/T, plunge velocity and pitch angle decay to zero. Total force measurements of Case 1-3 show that magnitude of force vectors also become zero at 0.5 t/T. Moreover, force measurements at downstroke and upstroke shows slight differences. Mechanical uncertainties that are presented due to production quality can cause these differences. To sum up, it can be said that the mechanism gives fairly good results comparing to validation case. However, it still needs further improvements.

CHAPTER 6

CONCLUSION

6.1 General Conclusions

The first part of the study mainly is focused on design and manufacturing procedure of a novel-flapping wing mechanism. Adjustable kinematic of the mechanism enables the investigation of various flapping trajectories. Each wing has three degrees of freedom around pitch, heave and plunge axes. That enables the investigation of 3-D flows around the flapping wings. Two wing model can be placed in tandem configuration and symmetric configuration. Flapping trajectories such as dragonfly's can be obtained by using tandem configuration. Furthermore, flapping trajectories similar to hummingbird and most of the insects can be created by symmetric or mono wing configuration. Modular structure of the wings enables a wide range of applications. Wings are controlled by special micro controllers by means of P-Control. Calibration of the wings is done by optimizing the P-constant and minimum PWM value.

Second part of the study involves calibration of the mechanism with different wings as well as validation of the mechanism is included. Also test procedure, dynamic scaling for finding the scaled frequency and data process are mentioned. Force and moment measurements for two different test campaign are completed with a flat plate Zimmerman wing rectangular wings. Force, moment and power time histories are plotted for one flapping cycle. Data are obtained by taking phase average of 50 flapping cycle. Calibration of coefficients of the flapping mechanism are determined.

Force and moment measurements are compared and discussed. Moreover, Validation test results are compared in order to check the reliability of the system. After validation procedure complete, similar motion with different pitching angle are tested. In brief, Second part of the study mainly focus on the testing with the system and investigating a simple back and forth flapping trajectory in hover flight with zero free stream velocity.

6.2 Recommendations for Further Studies

It is strongly suggested to take PIV measurements with the system. Comparing force and moment time history with the PIV measurements will help to develop an understanding of the source of the aerodynamic forces. To put it differently, correlation between vortex structure and the aerodynamic force development can be defined. Secondly, making alterations on mechanical wrist and gear box can increase the performance of the machine. Backlash of the gears generate position uncertainty. Lastly, preparing a Labview program for both flapping mechanism and the measurements instruments can solve the synchronizing problem. Current mechanism uses motor position data as feedback data during the motion. However, data from actual wing location is not collected. That's why, any uncertainty that are originated from the transmission cannot be reduced or sensed. Installing position sensors to the wing would definitely increase the wing trajectory precision of the flapping machine.

REFERENCES

[1] Ho, S., Nassef, H., Pornsinsirirak, N., Tai, Y., Ho, C., "Unsteadyaerodynamics and flow control for flapping wing flyers," *Progress in Aerospace Sciences,* vol. 39, pp. 635-681, 2003.

[2] Tennekes, H., The simple science of flight (from insects to jumbo jets), Boston, MA: MIT, 1996.

[3] Ellington, C. P., "Insects versus birds: the great divide," in *44th AIAA Aerospace Science Meeting and Exhibit*, Reno, Nevada, 9-12 January 2006.

[4] Merlin, P. W., "Design and Development of the Blackbird: Challenges and Lessons Learned," in *47th AIAA Aerospace Sciences Meeting Including The New Horizons Forum and Aerospace Exposition*, Orlando, Florida, 5-8 January 2009.

[5] Ben-Gida, H., Kirchhefer, A., Taylor, Z.J., Bezner-Kerr, W., Guglielmo, C.G., Kopp, G. A.,Gutka, R, "Estimation of unsteady aerodynamics in the wake of a freely flying European Starling (Sturnus vulgaris)," *PLoS ONE,* p. 8(11): e80086. doi:10.1371/journal.pone.0080086, 2013.

[6] Shyy, W., Lian, Y., Tang, J., Viieru, D., andLiu, H., Aerodynamics of Low Reynolds Number Flyers, New York: Cambridge Univ. Press, 2008.

[7] Mueller, T. J., Delaurier, J. D. , Fixed and Flapping Wing Aerodynamics for Micro Air Vehicle Applications, Reston, Virginia: AIAA, 2001.

[8] McMichael, J.M., and Francis, M.S, "Micro Air Vehicles – Toward a New Dimension in Flight," Defense Advanced Research Projects Agency (DARPA), Technical Report, 1997.

[9] Dickinson, M.H., "Solving the Mystery of Insect Flight," *Scientific American*, pp. 35-41, 2001.

[10] Güngör, A., Mutlu, T., Kurtuluş, D. F. , "Designing a Robotic Flapping Wing Mechanism in Order to Mimic the Insect Flight," in *7th Ankara International Aerospace Conference*, Ankara, 2013.

[11] Breitenstein, O., Bouabdallah, S., Leutenegger, S., Siegwart, R., "Development of a Flapping Wing Mechanism," Autonomous system Lab (ASL) Swiss federal Institude of Technology (ETH), Zurich, 2009.

[12] Sane, S. P. , "The aerodynamics of insect flight," *The Journal of Experimental Biology*, vol. 206, pp. 4191-4208, 2003.

[13] Walker, P.B., "Growth of circulation about a wing and an apparatus for measuring," ARC report, 1931.

[14] Dickinson, M. H., Götz, K. G., "Unsteady aerodynamic performance of model wings at low Reynolds numbers," *The Journal of Experimantal Biology*, vol. 174, pp. 45-64, 1993.

[15] Weis-Fogh, T., "Quick estimates of flight fitness in hovering animals, including novel mechanism for lift production," *The Journal of Experimantal Biology*, vol. 59, pp. 169-230, 1973.

[16] Lehmann, F.O., Sane, S.P., Dickinson, M.H. , " The aerodynamic effects of wing-wing interaction in flapping insect wings," *Lournal of Experimental Biology*, vol. 208, pp. 3075-3092, 2005.

[17] Dickinson, M. H., "The effects of wing rotation on unsteady aerodynamic performance at low Reynolds number," *The Journal of Experimantal Biology*, vol. 192, pp. 179-206, 1994.

[18] Birch, J. M., Dickinson, M. H. , "The influence of wing–wake interactions on the production of aerodynamic forces in flapping flight," *The Journal of Experimantal Biology*, vol. 206, pp. 2257-2272, 2003.

[19] Kramer, M., "Die zunahme des maximalauftriebes von tragflugeln bei plotzlicher anstellwinkelvergrosserung," . *Z Flugtech Motorluftschiff*, vol. 23, pp. 185-189, 1932.

[20] Bennett, L., "Insect flight: lift and the rate of change of incidence," *Science*, vol. 167, pp. 177-179, 1970.

[21] Gisler, S. , "Unsteady aerodynamics and control issues in flapping flight," Studies on mechatronics, Autonomous System Lab (ASL) , Swiss Federal Institute of Technology (ETH), Zurich, 2008.

[22] Steven, R. S., Fry, N., and Dickinson, M. H. , "The aerodynamics of hovering flight in drosphila," *J Exp Biol*, vol. 208, pp. 2303-2318, 2005.

[23] Birch, J. M., and Dickinson, M. H., "Spanwise flow and the attachment of the leading -edge vortex on insect wings," *Nature*, vol. 412, pp. 729-733, 2001.

[24] Liu, H.,and Kawachi, K., "A numerical study of insect flight," *Journal of Computational Physics*, vol. 146, pp. 124-156, 1998.

[25] Lighthill, M., "On Weis-Fogh mechanism of lift generation," *J. Fluid Mech.*, vol. 60, pp. 1-17, 1973.

[26] Sane, S. P., "Steady or Unsteady? Uncovering the Aerodynamic Mechanisms of Insect Flight," *Journal of Experimental Biology*, vol. 214, pp. 349-351, 2011.

[27] Dickinson, M. H., Lehmann, F.-O., and Sane, S., "Wing Rotation and the Aerodynamic Basis of Insect Flight," *Science*, vol. 284, pp. 1954-1960, 1999.

[28] Günaydınoğlu, E., Low Reynolds numbar aerodynamics of flapping airfoils in hover and forward flight, M.S. Thesis, Middle East Technical University METU (Ankara-Turkey), September 2010.

[29] George, R. B., Colton, M. B., Mattson, C. A., and Thomson, S. L, "A differentially driven flapping wing mechanism for force analysis and trajectory optimization," *International Journal of Micro Air Vehicles*, vol. 4, no. 1, pp. 31-49, 2012.

[30] Isaac, K. M., Colozza, A., Rolwes, J., "Force Measurements on a Flapping and Pitching Wing at Low Reynolds Numbers," in *44th AIAA Aerospace Sciences Meeting*, Reno, NV, 2006.

[31] Knoller, R., "Die Gestze des Luftwiderstandes," *Flug- und Motortechnik(Wien)*, vol. 3, no. 21, pp. 1-7, 1909.

[32] Betz, A., "Ein Beitrag zur Erlaerung des Segelfluges," *Zeitschrift fur Flugtechnik und Motorluftschiffahrt*, vol. 3, pp. 269-272, 1912.

[33] Dial,K. P., Tobalske, B. W., Peacock. W. L., "Kinematics of flap-bounding flight in the zebra finch over a wide range of speeds," *The Journal of Experimental biology*, vol. 202, pp. 1725-1739, 1999.

[34] Lehmann, F. O., Pick, S., "The aerodynamic benefit of wing-wing interaction depends on stroke trajectory in flapping insect wings," *The Journal of Experimental Biology*, vol. 210, pp. 1362-1377, 2007.

[35] Tobalske, B. W., Warrick, D. R., Clark, C. J., Powers, D. R., Hedrick, T. L., Hyder, G. A., Biewener,A. A. , "Three-dimensional kinematics of hummingbird," *The Journal of Experimental Biology*, vol. 210, pp. 2368-2382, 2007.

[36] Wood, R. J., "The first takeoff of a biologically-inspired at-scale robotic insect," *IEEE Trans. on Robotics,* vol. 24, no. 2, pp. 341-347, 2008.

[37] Croon, G.C.H.E., van Oudheusden, B.W., Remes, B.D.W., De Wagter, C., Ruijsink, R.,, "Design, Aerodynamics, and Autonomy of the DelFly," in *International Workshop on Bio-Inspired Robots from April 6 to 8, 2011*, Nantes, France, April 6 to 8, 2011.

[38] Bruggeman, B., Improving flight performance of DelFly II in hover by improving wing design and driving mechanism, Master Thesis, Faculty of Aerospace Engineering Delft University of Technology, October 2010.

[39] Frontzek, H., Knubben, E., Gaissert, N., Stoll, W., Festo AG&Co. KG, "festo," [Online]. Available: http://www.festo.com/. [Accessed 6 January 2014].

[40] Perez-Arancibia, N.O., Ma, K., Galloway, K., Greenberg, J., and Wood, R. J., "First Controlled Vertical Flight of a Biologically Inspired Microrobot," *Bioinspiration & Biomimetics,* vol. 6, no. 036009, 2011.

[41] De Wagter, C., Koopmans, A., de Croon, G.C.H.E., Remes, B.D.W., Ruijsink, R., "Autonomous Wind Tunnel Free-Flight of a Flapping Wing MAV," in *EuroGNC 2013*, Delft, 2013.

[42] Berg, C. V. D., and Ellington, C. P., "The three–dimensional leading–edge vortex of a 'hovering' model hawkmoth," *Philosophical Transactions of the Royal Society of London Series B Biological Sciences,* vol. 284, pp. 329-340, 1997.

[43] Simith, M. J. C., "Wing-drive mechanism, vehicle employing same, and method for controlling the wing-drive mechanism and vehicle employing same," *US/WA patent US,* 6,206,324 B1, 27 March 2001.

[44] Simith, M. J. C., "Wing-drive mechanism and vehicle employing same," *US/FL patent US*, 6,565,039 B2, 20 May 2003.

[45] Lai, W., Yan, J., Motamed, M., and Green, S., "Force Measurements on a Scaled Mechanical Model of Dragonfly in Forward Flight," in *12th International Conference on Advanced Robotics*,, 18-20 July2005.

[46] Morrison, C. L., Vandenheede, R. R. R, Kumar, D., Bernal, L. P., and Cesnik, C., "Force Measurements of a Flapping Wing with Two Angular Degrees of Freedom and Bio-Inspired Kinematics," in *50th AIAA Aerospace Sciences Meeting including the New Horizons Forum and Aerospace Exposi*, Nashville, Tennessee, 9-12 January 2012.

[47] DiLeo, C., and Deng, X., "Experimental Testbed and Prototype Development for a Dragonfly-Isnpired Robot," in *Conference on Intelligent Robots and Systems*, San Diego, 2007.

[48] Hu, Z., McCauley, R., Schaeffer, S., and Deng, X., "Aerodynamcis of dragon flight and robotic design," in *IEEE International Conference on Robotics and Automation*, Kobe, Japan, 2009.

[49] Deng, X., "engineering.purdue," Bio-Robotics Lab Purdue University, [Online]. Available: https://engineering.purdue.edu/~xdeng/equipment.html. [Accessed December 2012].

[50] Maybury, W. J., and Lehmann, F. O., "The fluid dynamics of flight control by kinematic," *The Journal of Experimental Biology*, vol. 207, pp. 4707-4726, 2004.

[51] Dickinson, M. H., "washington," Dickinson Lab University of hington, January 2013. [Online]. Available: http://depts.washington.edu/flyarama/media-gallery/. [Accessed january 2014].

[52] Kurtuluş, D. F., Numerical and Experimental Analysis of Flapping Motion in Hover. Application to Micro Air Vehicle, Joint Ph.D. Thesis, Poitiers University/ENSMA (Poitiers-France) and METU (Ankara-Turkey), June 2005.

[53] Willmott, A. P., and Ellinton, C. P, "The mechanics of the flight in the hawkmoth Manduca Sexta. I. Kinematics of hovering and forward flight," *Journal of Experimental Biology,* vol. 200, pp. 2705-22.

[54] "getdata-graph-digitizer," [Online]. Available: http://getdata-graph-digitizer.com/index.php. [Accessed 05 01 2014].

[55] ATI Industrial Automation, Inc., "ati-ia," 5 2003. [Online]. Available: http://www.ati-ia.com/app_content/documents/9610-05-1019%20%20ISA%20FT-16%20(ALL).pdf. [Accessed 3 1 2013].

[56] Sturgis, C., Chambers, R. , "ati-ia," ATI Industrial Automation, 1 11 2010. [Online]. Available: http://www.ati-ia.com/app_content/Documents/9230-05-1364.pdf. [Accessed 3 1 2013].

APPENDIX A

RESULTS OF THE CASE STUDIES

In this part raw data of the calibration test are presented for each proportional constant 'Kp'. Also, position error history of the motions are plotted for different proportional constants agein. In addition, Pure pitch, pure plunge and combined pitch&plunge case results are given. These results are presented only first four succesive period of the flapping motion.

A.1 Results of P-Constant Calibration Test

A.1.1 Pitch Axis Calibration Raw Data

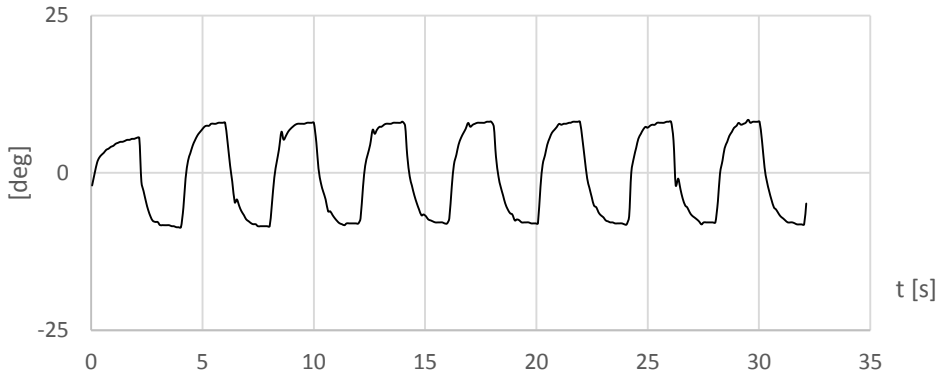

Figure A.1 Time history of the pitching angle obtained from Wing Module 2 with a pure pitching ($K_p = 1,\ A = 20°, f = 0.25\ Hz$) Zimmerman wing

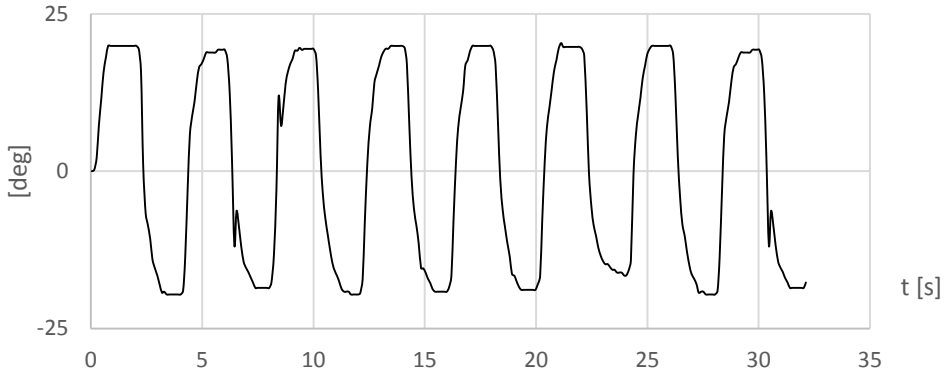

Figure A.2 Time history of the pitching angle obtained from Wing Module 2 with a pure pitching ($K_p = 2,\ A = 20°, f = 0.25\ Hz$) Zimmerman wing

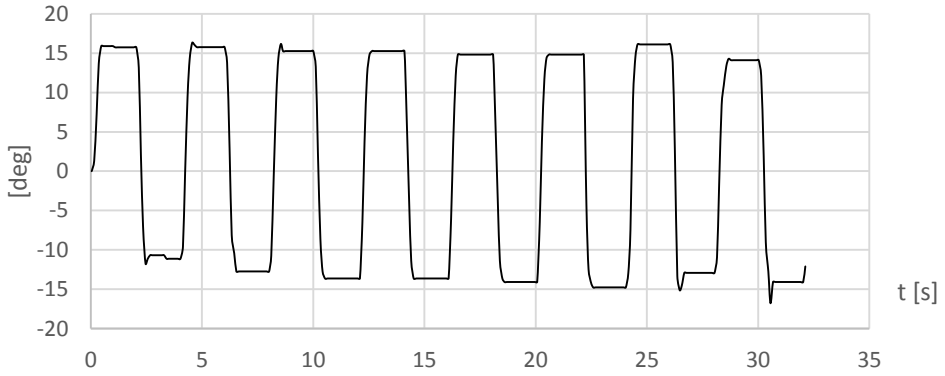

Figure A.3 Time history of the pitching angle obtained from Wing Module 2 with a pure pitching ($K_p = 3,\ A = 20°, f = 0.25\ Hz$) Zimmerman wing

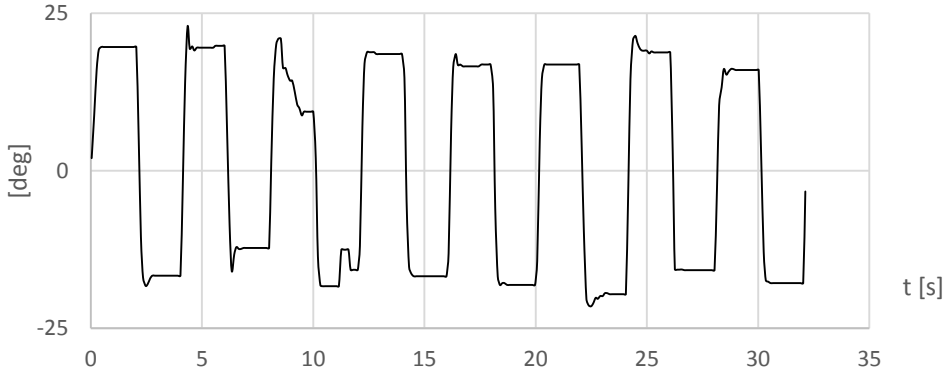

Figure A.4 Time history of the pitching angle obtained from Wing Module 2 with a pure pitching ($K_p = 4,\ A = 20°, f = 0.25\ Hz$) Zimmerman wing

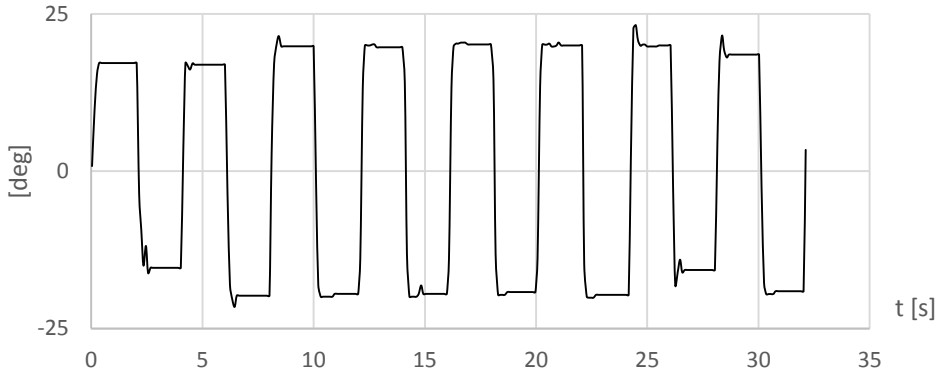

Figure A.5 Time history of the pitching angle obtained from Wing Module 2 with a pure pitching ($K_p = 5,\ A = 20°, f = 0.25\ Hz$) Zimmerman wing

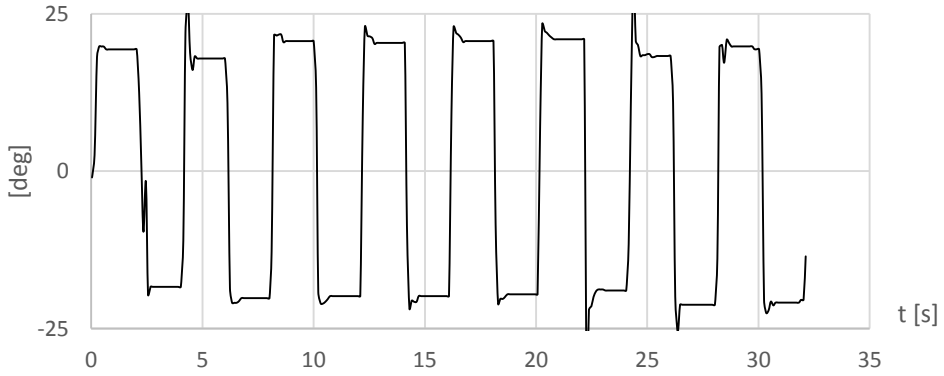

Figure A.6 Time history of the pitching angle obtained from Wing Module 2 with a pure pitching ($K_p = 6,\ A = 20°, f = 0.25\ Hz$) Zimmerman wing

A.1.2 Plunge Axis Calibration Data

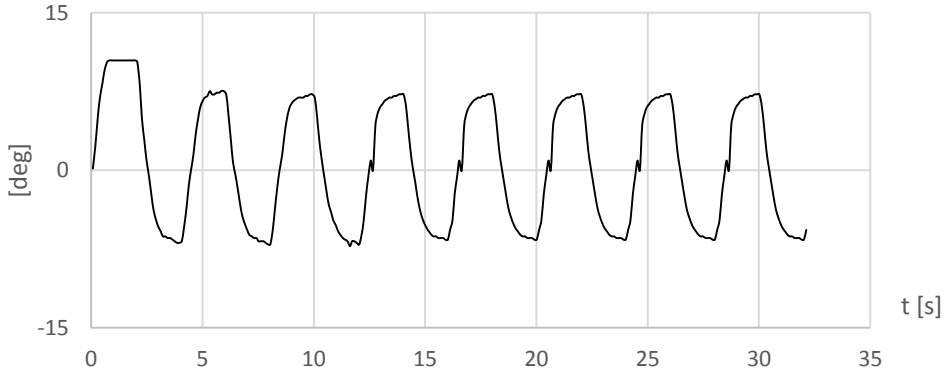

Figure A.7 Time history of the plunge angle obtained from Wing Module 2 with a pure plunging ($K_p = 1,\ A = 10°, f = 0.25\ Hz$) Zimmerman wing

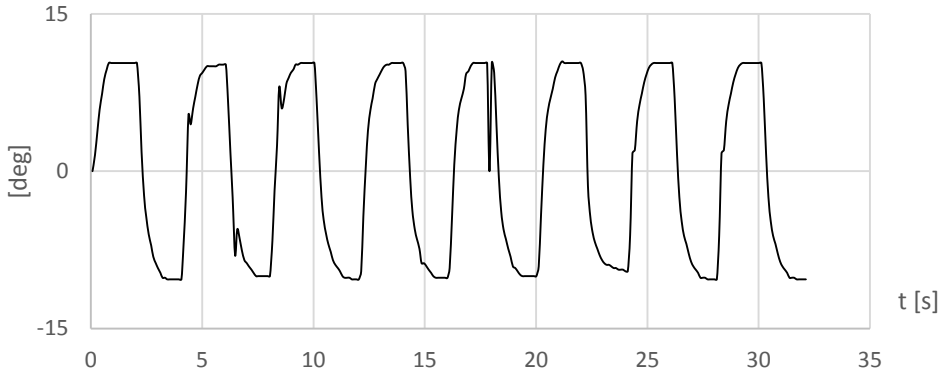

Figure A.8 Time history of the plunge angle obtained from Wing Module 2 with a pure plunging ($K_p = 2,\ A = 10°, f = 0.25\ Hz$) Zimmerman wing

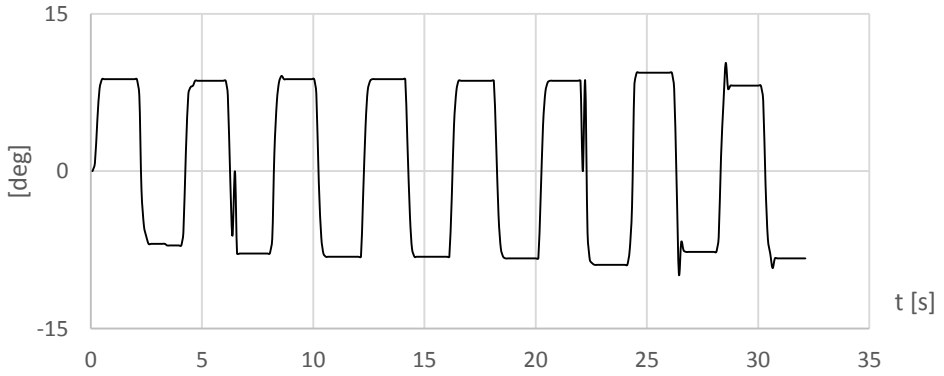

Figure A.9 Time history of the plunge angle obtained from Wing Module 2 with a pure plunging ($K_p = 3,\ A = 10°, f = 0.25\ Hz$) Zimmerman wing

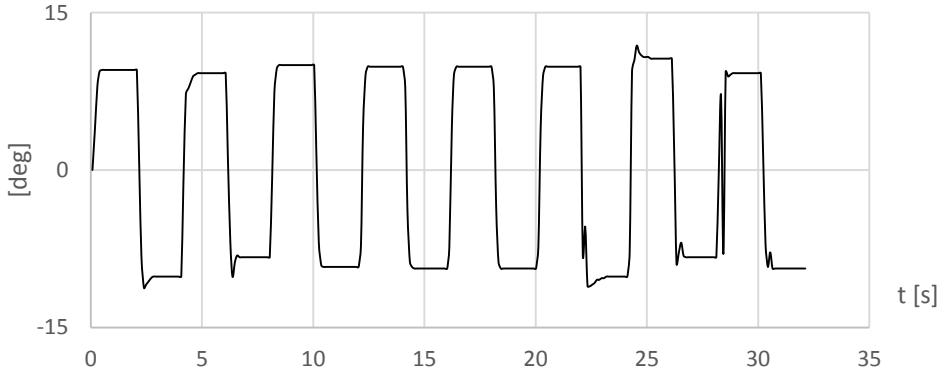

Figure A.10 Time history of the plunge angle obtained from Wing Module 2 with a pure plunging ($K_p = 4,\ A = 10°, f = 0.25\ Hz$) Zimmerman wing

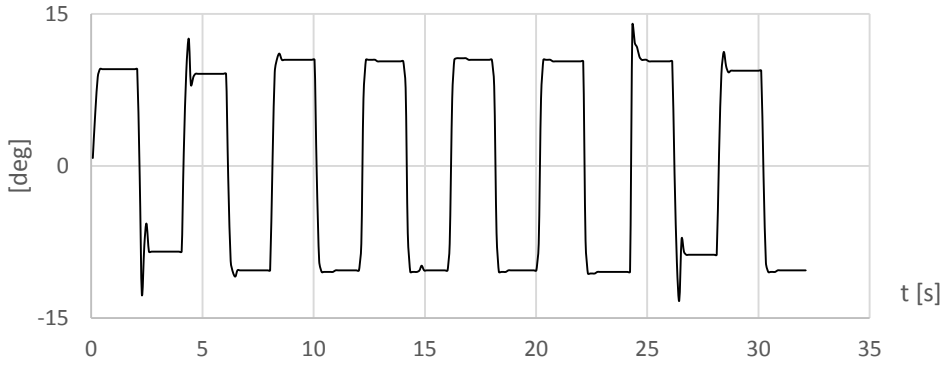

Figure A.11 Time history of the plunge angle obtained from Wing Module 2 with a pure plunging ($K_p = 5,\ A = 10°, f = 0.25\ Hz$) Zimmerman wing

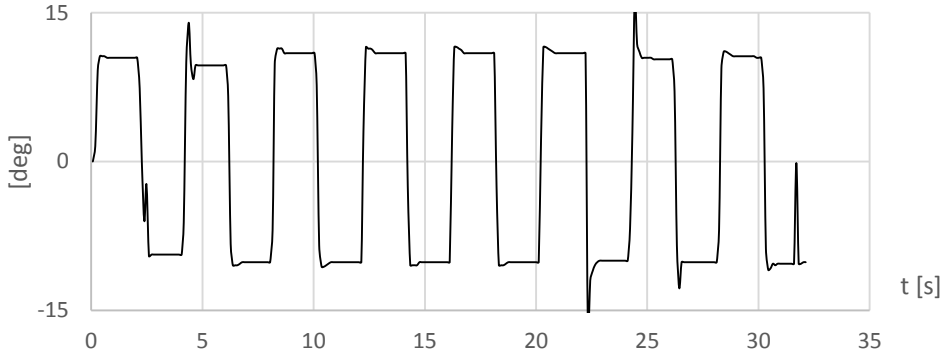

Figure A.12 Time history of the plunge angle obtained from Wing Module 2 with a pure plunging ($K_p = 6,\ A = 10°, f = 0.25\ Hz$) Zimmerman wing

A.2 Results of Combined Pitch And Plunge Motions

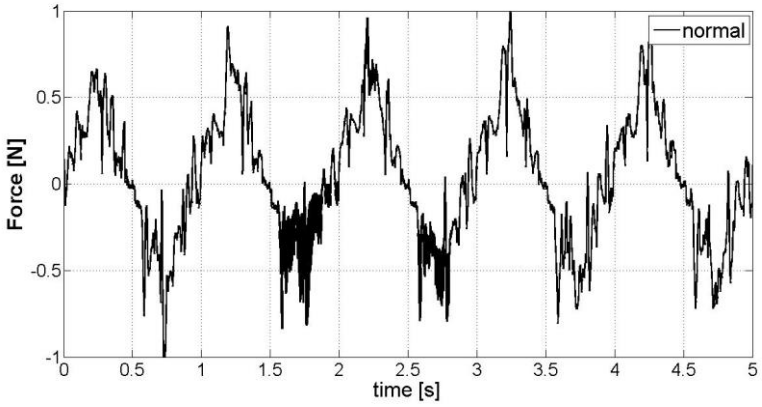

Figure A.13 Raw data of normal force time history Case 1 (A_{pitch}=30º, A_{plunge}= 57º, f=0.14 Hz)

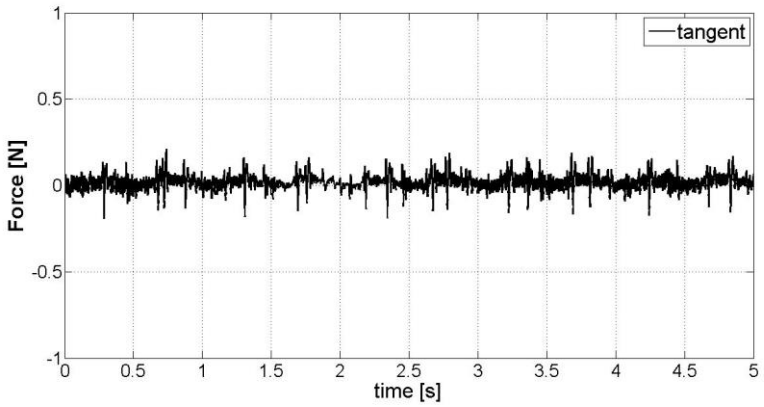

Figure A.14 Raw data of tangential force time history Case 1 (A_{pitch}=30º, A_{plunge}= 57º, f=0.14 Hz)

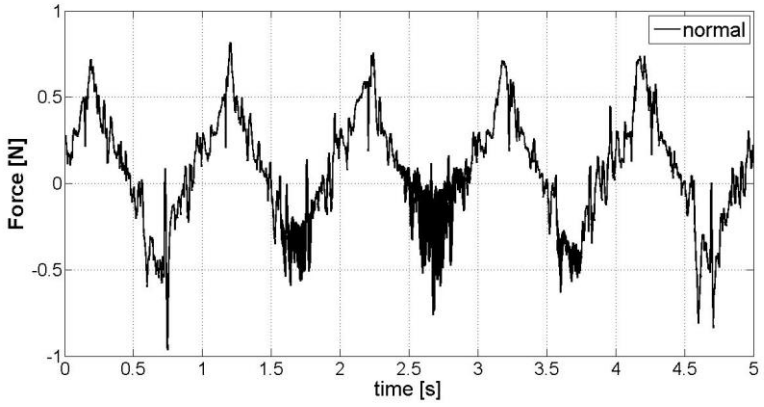

Figure A.15 Raw data of normal force time history Case 2 (A_{pitch}=45º, A_{plunge}= 57º, f=0.14 Hz)

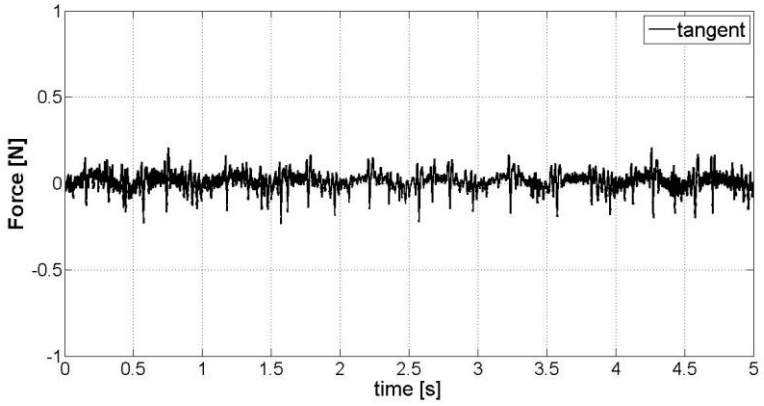

Figure A.16 Raw data of tangential force time history Case 2 (A_{pitch}=45º, A_{plunge}= 57º, f=0.14 Hz)

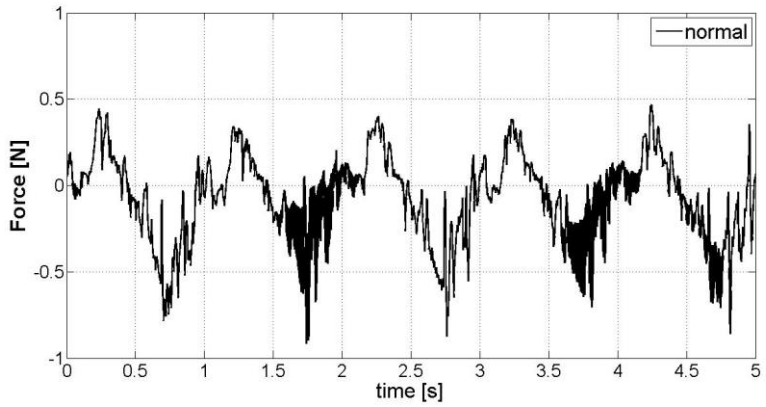

Figure A.17 Raw data of normal force time history Case 3 (A_{pitch}=57º, A_{plunge}= 57º, f=0.14 Hz)

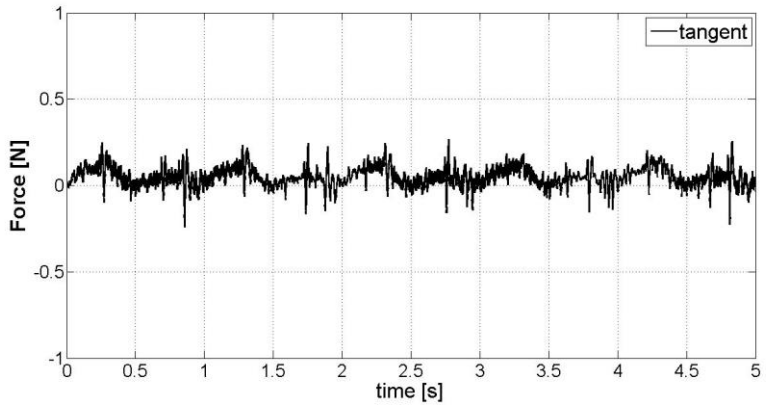

Figure A.18 Raw data of tangential force time history Case 3 (A_{pitch}=57º, A_{plunge}= 57º, f=0.14 Hz)

A.3 Results of the Validation Case

This part gives the original results that are presented in the Morrison's study. Time History for the angular position of the wings given in Figure A.19. Only the sinusoidal motion results are used for validation experiments. Figure A.20 gives the force measurement results. Lastly, Figure A.21 shows the total aerodynamic force coefficient graphs for three different trajectory.

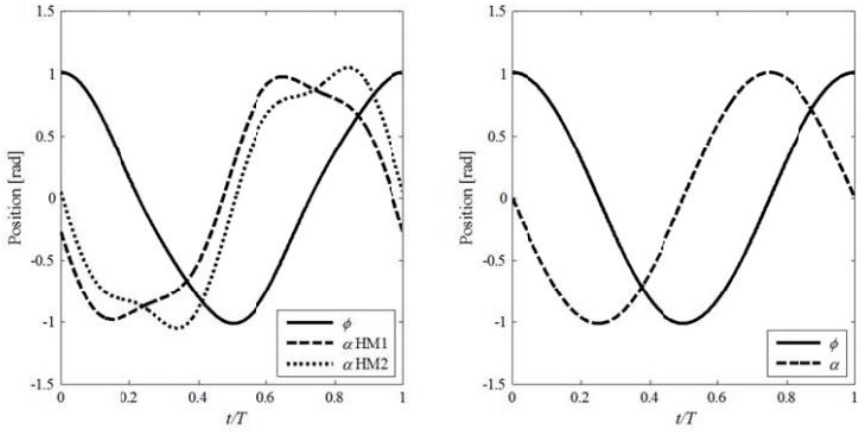

Figure A.19 Flapping angle and incidence angle time histories used in the Morrison's experiment. (a) bio-inspired motions. (b) sinusoidal motion (from Ref. [46])

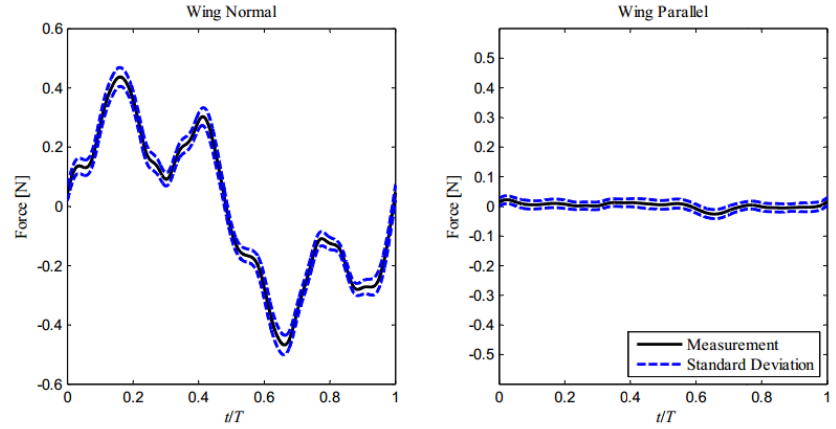

Figure A.20 Processed force signal and standard deviation for sinusoidal motion of combined pitch and plunge (from Ref. [46])

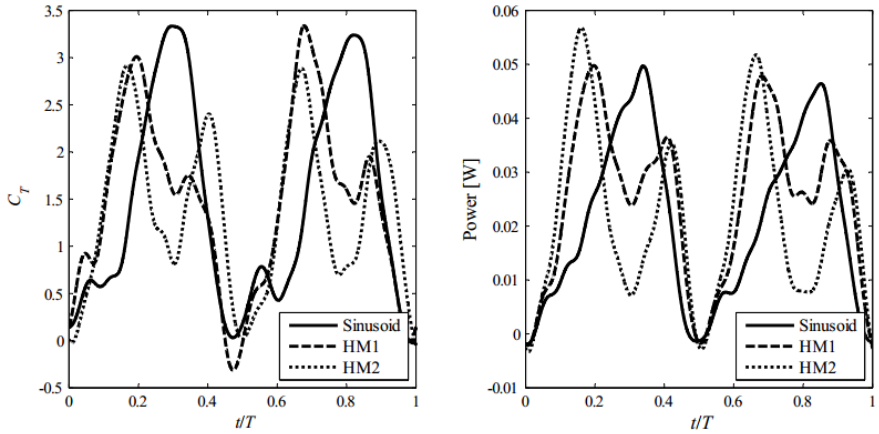

Figure A.21 Processed force and power time histories for sinusoidal, HM1 and HM2 bio-inspired motions of Hawkmott wing model (from Ref. [46])

A.4 Data Analysis

In this Part an in house MATLAB code is given. This code is used for analyzing the raw force measurements of the ATI NANO17. First, the data is filtered by using a Butterworth filter. Second, the code is used for omitting the initial flapping periods. Then, phase average of the data is performed. Finally, raw data, filtered data and phase averaged data are plotted.

MATLAB Code:

```
%************************************************************
%*                                                          *
%*  ATI NANO 17 Data Analyzer Version 1.5                   *
%*                                                          *
%*  Written By Talha MUTLU - 13.02.2014                     *
%*                                                          *
%*  Department of Aerospace Engineering                     *
%*  Middle East Technical University                        *
%*                                                          *
%*  Date: 16.01.2014                                        *
%*                                                          *
%************************************************************
%*
%*  Clear the Workspace before starting the analysis
%*
clc
clear all
close all
%*
%%  Load input file 'force.xlsx'
%*  Data Formant: t,t/T,F_n,F_t
%*  t       :   time                        [s]
%*  t/T     :   non-dimensional time         -
%*  F_n     :   Normal Force                [N]
%*  F_t     :   Tangential Force            [N]
%*
[data, txt] = xlsread('force.xlsx');
%*
%%  Filter force measurement by using Butterworth filter
%*
cut_off_freq = 1.5;
samp_freq=100;
[b,a] = butter(5,2*cut_off_freq/samp_freq,'low');
fdata(:,1:2)=data(:,1:2);
fdata(:,3:4) = filter(b,a,data(:,3:4));
l=length(fdata);
%reverse the data string
for j=1:l
 fdata1(j,3:4)=fdata(l+1-j,3:4);
end
```

```
%filter again to cancel out the phase shift
fdata2(:,3:4) = filter(b,a,fdata1(:,3:4));
%reverse the data string to original order
for j=1:l
 fdata(j,3:4)=fdata2(l+1-j,3:4);
end
%*
%% FFT Analysis
%*
C1=data(:,3);
L1 = length(C1); % Length of signal
T=0.01; % Sample time
Fs=1/T; % Sampling frequency
t = (0:L1-1)*T;                % Time vector
C1n=C1-C1(1,1)*ones(L1,1);
%*
C2=data(:,3);
L2 = length(C2) % Length of signal
T=0.01; % Sample time
Fs=1/T % Sampling frequency
t = (0:L2-1)*T;                % Time vector
C2n=C2-C2(1,1)*ones(L2,1);
%*
Y1 = fft(C1n)/L1;
f1 = Fs/2*linspace(0,1,L1/2+1);
%*
Y2 = fft(C2n)/L2;
f2 = Fs/2*linspace(0,1,L2/2+1);
%*
%% Phase average filtered data force
%* Normal force
N_phase = floor(length(fdata)/714)-1;
for j=1:714
    sum = 0;
    for i=1:N_phase
        temp = fdata(j+714*(i-1),3);
        sum = sum + temp;
    end
    phase_avg1(j) = sum / N_phase;
end
%* Tangential force
for j=1:714
    sum = 0;
    for i=1:N_phase
        temp = fdata(j+714*(i-1),4);
        sum = sum + temp;
    end
    phase_avg2(j) = sum / N_phase;
end
%*
%% Phase average raw data force
%* Normal force
N_phase = floor(length(data)/714)-1;
for j=1:714
    sum = 0;
    for i=1:N_phase
        temp = data(j+714*(i-1),3);
        sum = sum + temp;
```

```
    end
    phase_avg1r(j) = sum / N_phase;
end
%* Tangential force
for j=1:714
    sum = 0;
    for i=1:N_phase
        temp = data(j+714*(i-1),4);
        sum = sum + temp;
    end
    phase_avg2r(j) = sum / N_phase;
end
%*
%% Calculate Raw Total Force
for j=1:714
    total1(j)= sqrt(data(j,3)^2+data(j,4)^2);
end
%*
%% Calculate Phase Averaged and Filtered Total Force,
%*
for j=1:714
    total(j)= sqrt(phase_avg1(j)^2+phase_avg2(j)^2);
end
%*
%% Calculate Phase Averaged Raw Total Force,
%*
for j=1:714
    totalr(j)= sqrt(phase_avg1r(j)^2+phase_avg2r(j)^2);
end
%*
%%  Plot Raw and Filtered Data of Normal Force, Tangential Force,
Total Force
%*
 figure(1)
plot(data(:,2),data(:,3),'b','linewidth',2);
set(gca,'fontsize',20,'Xlim',[0 1],'Ylim' ,[-1 1])
 h(3) = legend('10th Period raw data');
 h(1) = xlabel('t/T','fontsize',24);
 h(2) = ylabel('Normal Force[N]','fontsize',24,'fontweight','bold');
 set(h(3),'fontsize',24)
 grid on
%*
 figure(2)
plot(data(:,2),data(:,4),'b','linewidth',2);
set(gca,'fontsize',20,'Xlim',[0 1],'Ylim',[-1 1])
 h(3) = legend('10th Period raw data');
 h(1) = xlabel('t/T','fontsize',24);
 h(2) = ylabel('Tangent   Force[N]'
,'fontsize',24,'fontweight','bold');
 set(h(3),'fontsize',24)
 grid on
%*
figure(3)
plot(f1,2*abs(Y1(1:L1/2+1)),'b','linewidth',2)
set(gca,'fontsize',20,'Xlim',[0 10])
hold on
 h(3) = legend('normal');
 h(1) = xlabel('Frequency [Hz]','fontsize',24);
```

```
 h(2) = ylabel('Force [N]','fontsize',24,'fontweight','bold');
set(h(3),'fontsize',24)
 grid on
[max1,I1]=max(abs(Y1));
f_max=f1(I1);
%*
figure(4)
plot([1:714]/714,phase_avg1r,'b','linewidth',2)
set(gca,'fontsize',20,'Xlim',[0 1],'Ylim' ,[-1 1])
 h(3) = legend('Phase average of raw data');
 h(1) = xlabel('t/T','fontsize',24);
 h(2) = ylabel('Normal Force[N]','fontsize',24,'fontweight','bold');
 set(h(3),'fontsize',24)
 grid on
%*
figure(5)
plot([1:714]/714,phase_avg2r,'b','linewidth',2)
 set(gca,'fontsize',20,'Xlim',[0 1],'Ylim',[-1 1])
 h(3) = legend('Phase average of raw data');
 h(1) = xlabel('t/T','fontsize',24);
 h(2) = ylabel('Tangent   Force[N]'
,'fontsize',24,'fontweight','bold');
 set(h(3),'fontsize',24)
 grid on
%*
%%  Plot Normal Force, Tangential Force, Total Force
%*
 figure(6)
plot(data(:,2),data(:,3),'g','linewidth',2);
set(gca,'fontsize',20,'Xlim',[0 1],'Ylim' ,[-1 1])
 hold on
plot([1:714]/714,phase_avg1r,'r','linewidth',2)
plot([1:714]/714,phase_avg1,'b','linewidth',2)
 h(3) = legend('10th Period raw data','Phase average of raw
data','Phase average of filtered data');
 h(1) = xlabel('time [s]','fontsize',24);
 h(2) = ylabel('Normal Force[N]','fontsize',24,'fontweight','bold');
set(h(3),'fontsize',24)
 grid on
%*
 figure(7)
plot(data(:,2),data(:,4),'g','linewidth',2);
set(gca,'fontsize',20,'Xlim',[0 1],'Ylim',[-1 1])
 hold on
plot([1:714]/714,phase_avg2r,'r','linewidth',2)
plot([1:714]/714,phase_avg2,'b','linewidth',2)
 h(3) = legend('10th Period raw data','Phase average of raw
data','Phase average of filtered data');
 h(1) = xlabel('time [s]','fontsize',24);
 h(2) = ylabel('Tangent Force  [N]'
,'fontsize',24,'fontweight','bold');
 set(h(3),'fontsize',24)
 grid on
%*
  figure(8)
plot([1:714]/714,total1,'g','linewidth',2)
set(gca,'fontsize',20,'Xlim',[0 1],'Ylim',[-1 1])
 hold on
```

```
plot([1:714]/714,totalr,'r','linewidth',2)
plot([1:714]/714,total,'b','linewidth',2)
 h(3) = legend('10th Period raw data','Phase average of raw
data','Phase average of filtered data');
 h(1) = xlabel('time [s]','fontsize',24);
 h(2) = ylabel('Total Force [N]','fontsize',24,'fontweight','bold');
 set(h(3),'fontsize',24)
 grid on
```

APPENDIX B

EXPERIMENTAL SETUP DETAILS

Detailed drawings of flapping wing mechanism and the specification of ATI NANO17 are presented with technical drawings. All dimensions are in millimeters [mm] unless otherwise specified.

B.1 Flapping Wing Mechanism Drawings

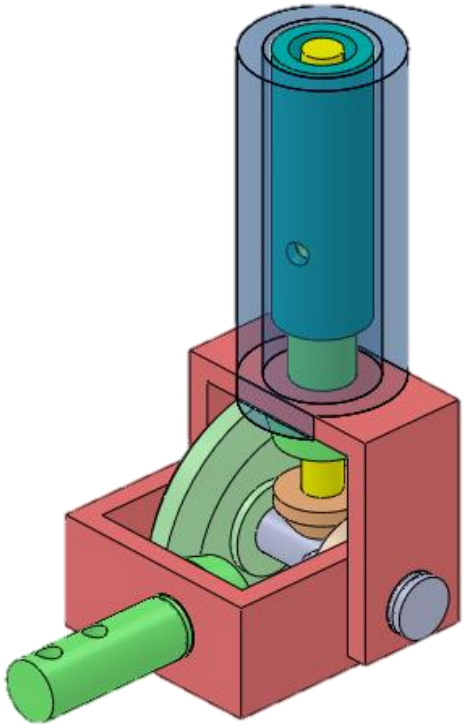

Figure B.1 Mechanical wrist CAD drawing

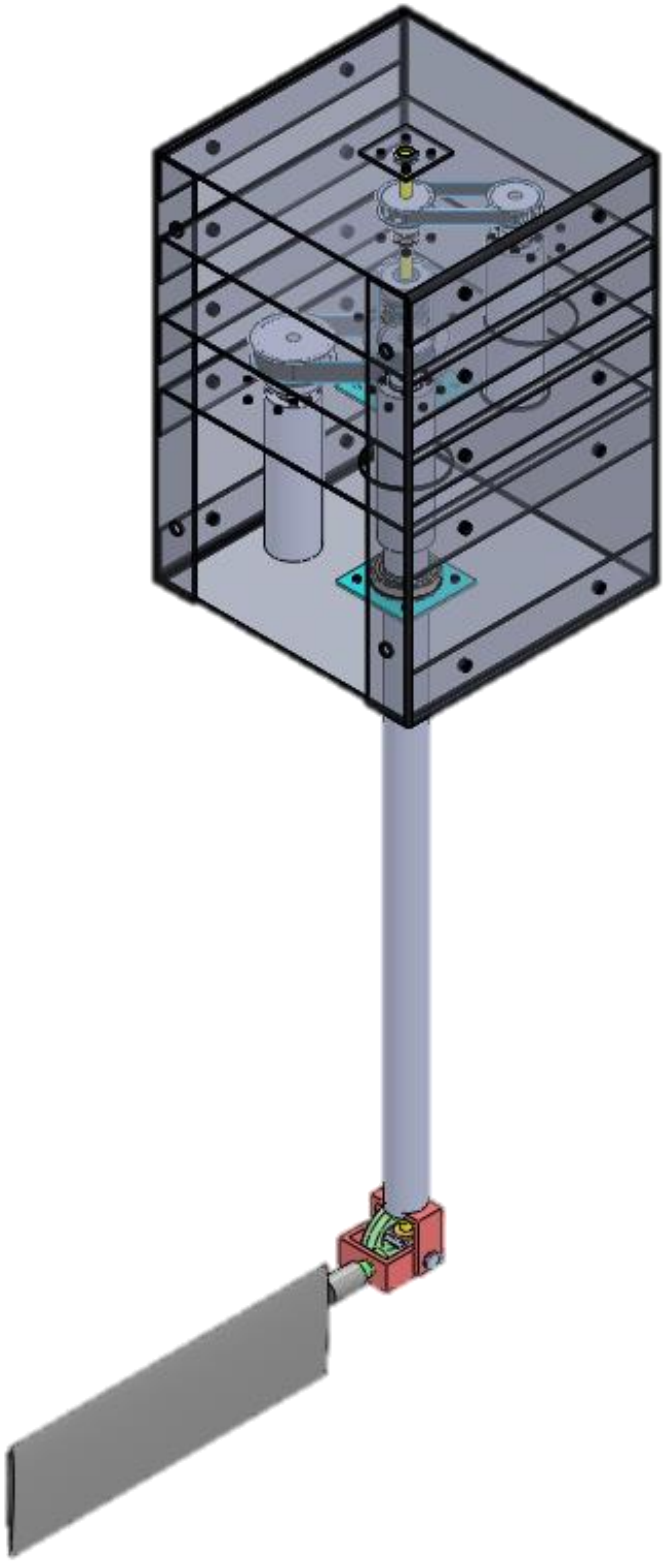

Figure B.2 Flapping wing mechanism wing module CAD drawing

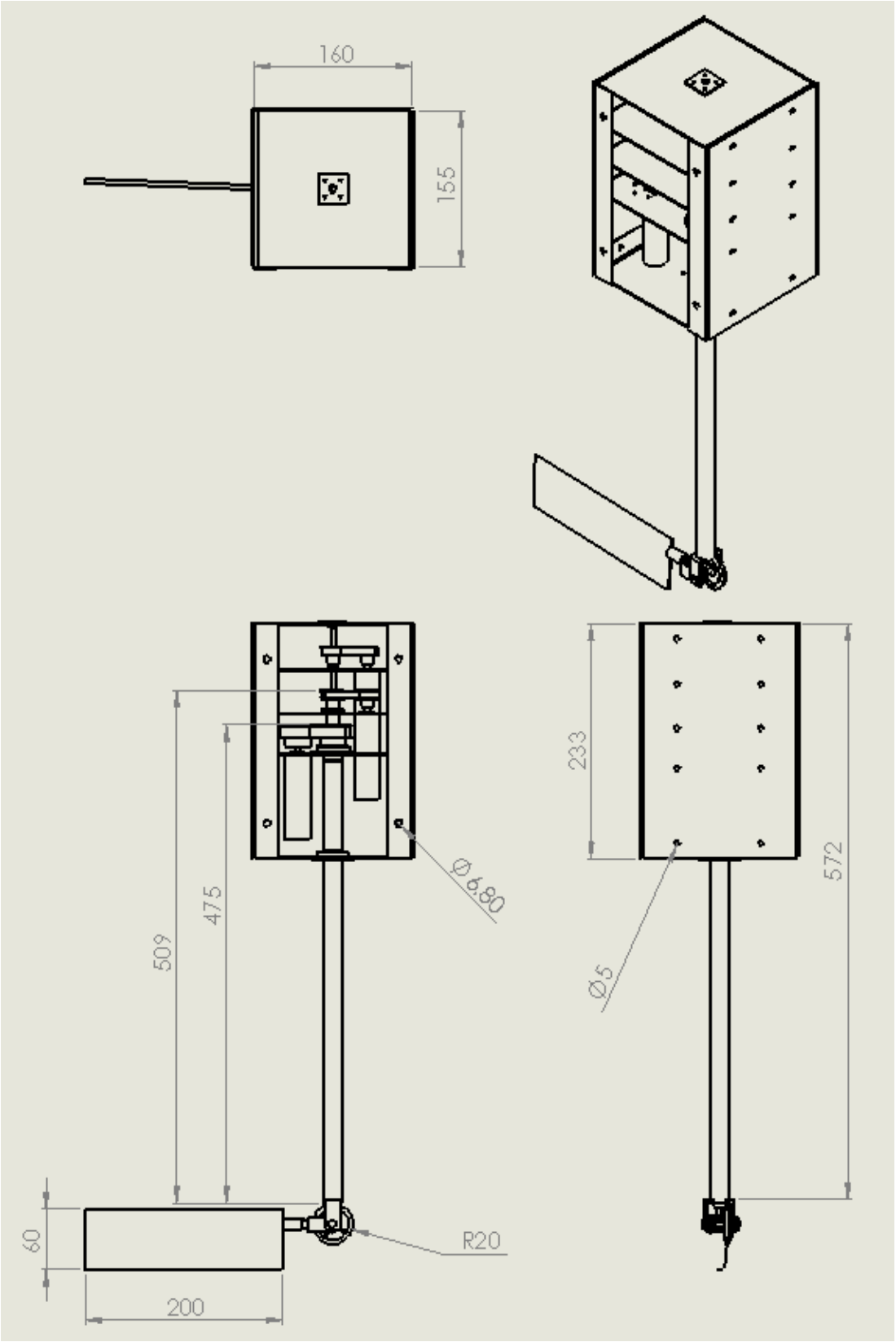

Figure B.3 Technical drawings of the wing module with dimensions (unless otherwise specified all dimensions are in millimeter)

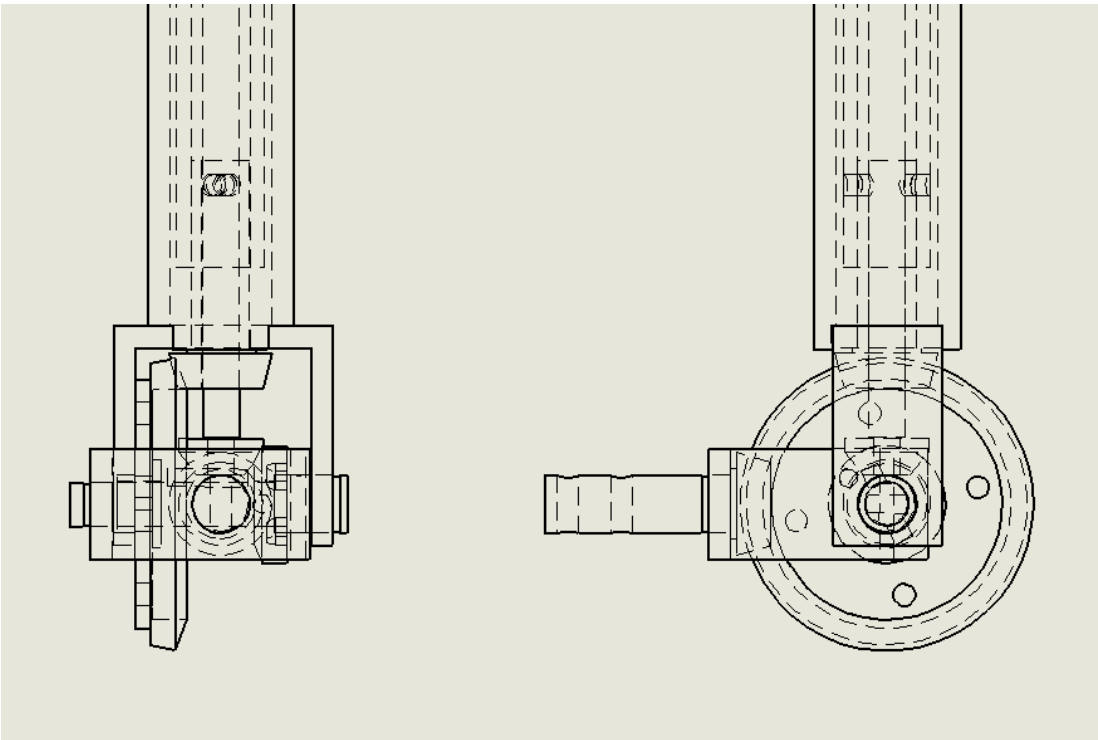

Figure B.4 Drawings of mechanical wrist mechanism

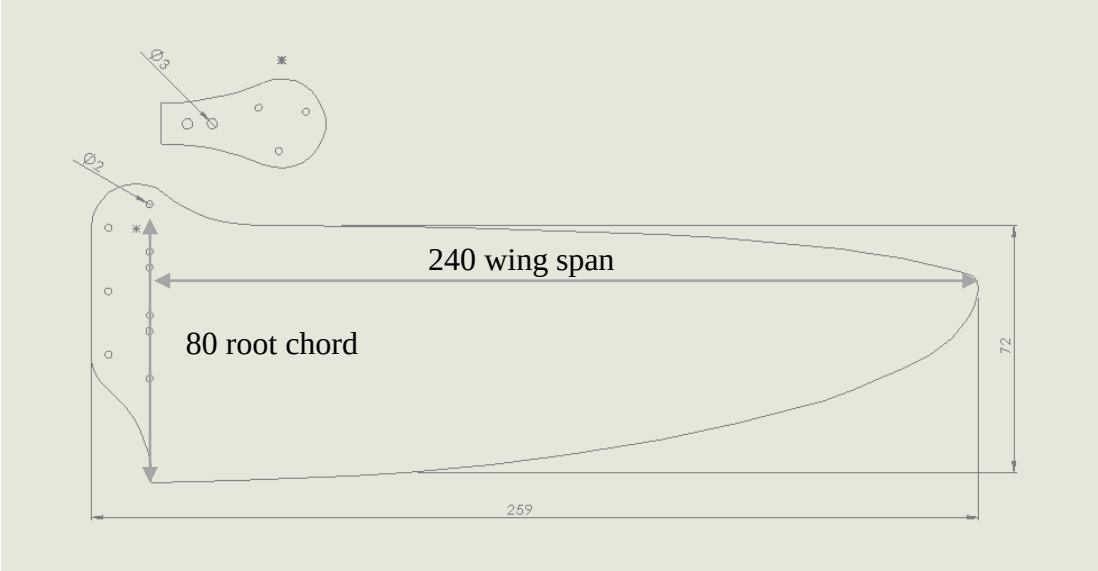

Figure B.5 Wing and connection part drawing

B.2 Force and Moment Measurement System Specifications

Table B.1 ATI NANO17 calibration specifications (from Ref. [55])

Calibration	SI-12-0.12	SI-25-0.25	SI-50-0.5
Rated Sensing Ranges			
Fx, Fy	±12.0 N	±25 N	±50 N
Fz	±17 N	±35 N	±70 N
Tx, Ty, Tz	±120 Nmm	±250 Nmm	±500 Nmm
Resualution (16-bit)			
Fx, Fy	1/1280 N	1/640 N	1/320 N
Fz	1/1280 N	1/640 N	1/320 N
Tx, Ty, Tz	1/256 Nmm	1/128 Nmm	1/64 Nmm
Counts Value (16-bit)			
Fx, Fy, Fz	1280 / N	640 / N	320 / N
Tx, Ty, Tz	256 / Nmm	128 / Nmm	64 / Nmm
Tool Transform Factor	0.05 mm/unit	0.05 mm/unit	0.05 mm/unit

Table B.2 ATI NANO17 physical specifications (from Ref. [55])

Physical Properties	
Stiffness (Calculated)	
X-axis and Y-axis force (Kx, Ky)	9.3×10^6 N/m
Z-axis force (Kz)	12×10^6 N/m
X-axis and Y-axis torque (Ktx, Kty)	250 Nm/rad
axis torque (Ktz)	390 Nm/rad
Resonant Frequency (Measured)	
Fx, Fy, Fz	7.2 kHz
Tx, Ty, Tz	7.2 kHz
Maximum Single-axis Load	
Fx, Fy	±350 N
Fz	±750 N
Tx, Ty	±2.4 Nm
Tz	±3.1 Nm
Weight	
Transducer with standard aluminum plates	9.4 g
Transducer with stainless steel plates	19 g
Material	
Transducer	Hardened Stainless Steel
Mounting and tool adapters	Aircraft Aluminum

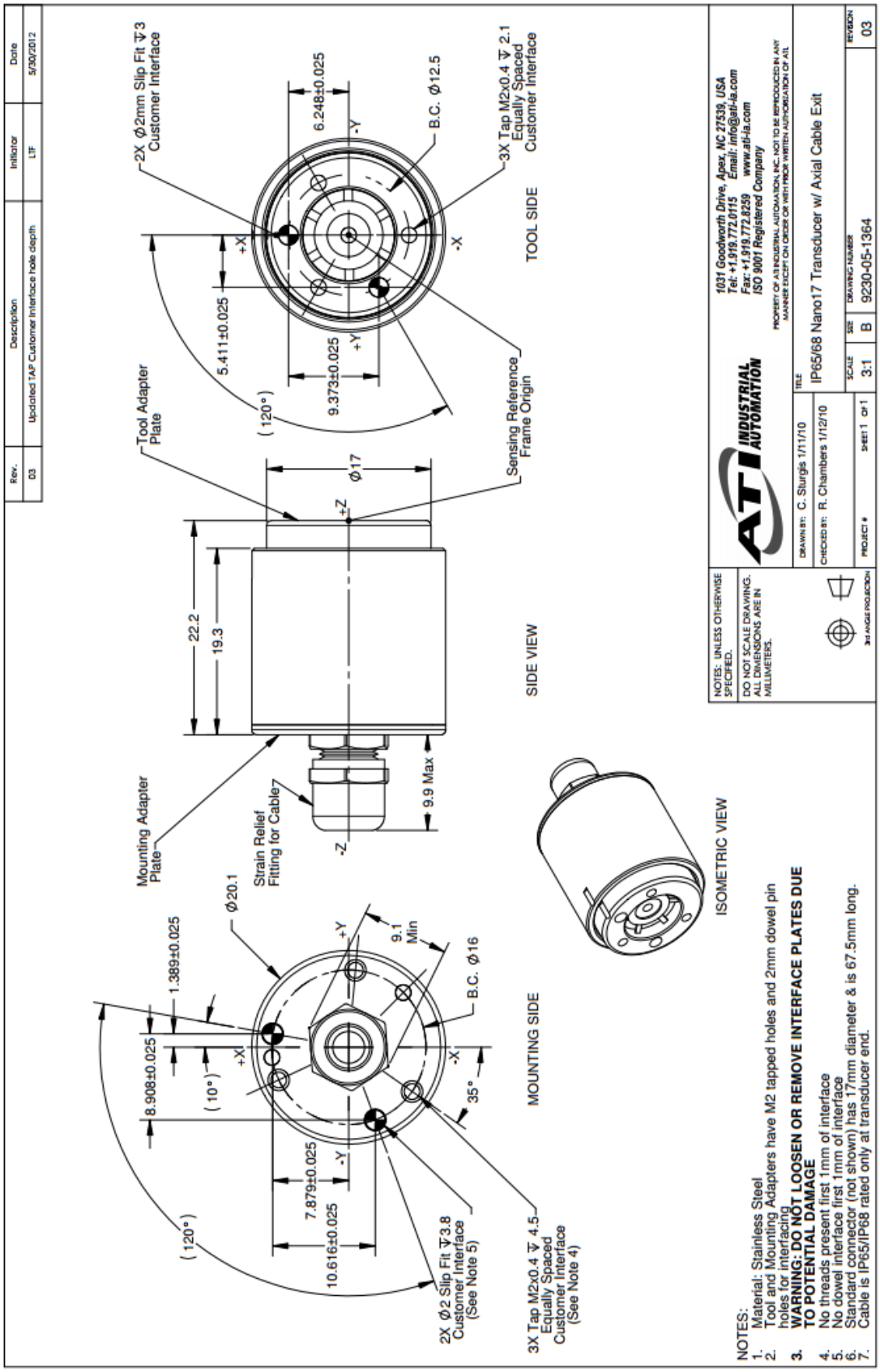

Figure B.6 ATI NANO17 IP65/IP68 Transducer with Axial Cable Exit [56]

APPENDIX C

GREAT FLIGHT DIAGRAM

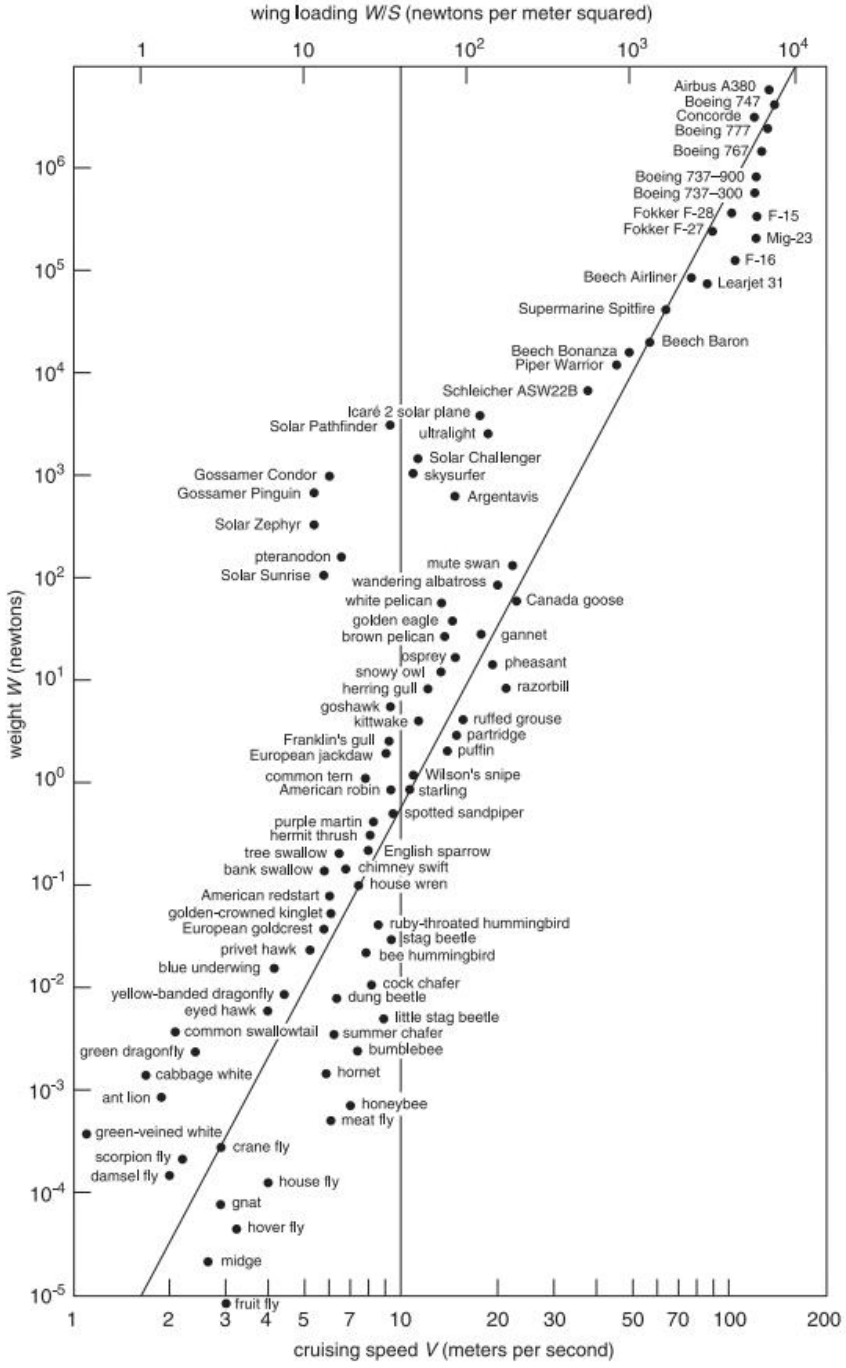

Figure C.1 The great diagram of flight [2]